

AN ABSTRACT OF THE THESIS OF

Darrick E. Boschmann for the degree of Master of Science in Geology presented on
November 29, 2012

Title: Structural and Volcanic Evolution of the Glass Buttes Area, High Lava Plains,
Oregon

Abstract approved:

John H. Dilles

Andrew J. Meigs

The Glass Buttes volcanic complex is a cluster of bimodal (basalt-rhyolite), Miocene to Pleistocene age lava flows and domes located in Oregon's High Lava Plains province, a broad region of Cenozoic bimodal volcanism in south-central Oregon. The High Lava Plains is deformed by northwest-striking faults of the Brothers Fault Zone, a diffuse, ~N40°W trending zone of en echelon faults cutting ~250 km obliquely across the High Lava Plains. Individual fault segments within the Brothers Fault Zone are typically <20 km long, strike ~N40°W, have apparent normal separation with 10-100 m throw. A

smaller population of ~5-10 km long faults striking ~N30°E exhibits mutually cross-cutting relationships with the dominant northwest striking faults.

Basaltic volcanic rocks in the Glass Buttes area erupted during the late Miocene and Pleistocene. The oldest and youngest lavas are 6.49 ± 0.03 Ma and 1.39 ± 0.18 Ma, respectively, based on $^{40}\text{Ar}/^{39}\text{Ar}$ ages of five basaltic units. Numerous small mafic vents both within and around the margins of the main silicic dome complex are commonly localized along northwest-striking faults of the Brothers Fault Zone. These vents erupted a diverse suite of basalt to basaltic andesite lava flows that are here differentiated into 15 stratigraphic units based on hand sample texture and mineralogy as well as major and trace element geochemistry.

The structural fabric of the Glass Buttes area is dominated by small displacement, discontinuous, en echelon, northwest-striking fault scarps that result from normal to slightly oblique displacements and are commonly linked by relay ramps. Northwest alignment of basaltic and rhyolitic vents, paleotopography, and cross-cutting relationships suggest these faults have been active since at least 6.49 ± 0.03 Ma, the age of the rhyolite lavas in the eastern Glass Buttes area. Faults displace Quaternary sedimentary deposits indicating these structures continue to be active into the Quaternary. Long-term extension rates across northwest-striking faults calculated from 2-5 km long cross section restorations range from 0.004 – 0.02 mm/yr with an average of 0.12 mm/yr.

A subordinate population of discontinuous northeast-striking faults form scarps and exhibit mutually cross-cutting relationships with the dominant northwest-striking population. Cross-cutting relationships indicate faulting on northeast-striking faults ceased sometime between 4.70 ± 0.27 Ma and 1.39 ± 0.18 Ma.

Gravity data at Glass Buttes reveals prominent northwest- and northeast-trending gravity gradients that closely parallel the strikes of surface faults. These are interpreted as large, deep-seated, normal faults that express themselves in the young basalts at the surface as the discontinuous, en echelon fault segments seen throughout the study area and BFZ in general. Elevated geothermal gradients are localized along these deep-seated structures at two locations: (1) where northwest- and northeast-striking faults intersect, (2) along a very prominent northwest-striking active normal fault bounding the southwest flank of Glass Butte.

High average heat flow and elevated average geothermal gradients across the High Lava Plains, and the presence of hydrothermal alteration motivated geothermal resource exploration at Glass Buttes. Temperature gradient drilling by Phillips Petroleum and others between 1977-1981 to depths of up to 600 m defined a local geothermal anomaly underlying the Glass Buttes volcanic complex with a maximum gradient of 224 °C/km.

Stratigraphic constraints indicate that near-surface hydrothermal alteration associated with mercury ores ceased before 4.70 ± 0.27 Ma, and is likely associated with the 6.49 ± 0.03 Ma rhyolite eruptions in the eastern part of Glass Buttes. The modern thermal anomaly is not directly related to the pre- 4.70 ± 0.27 Ma hydrothermal system; rather it is likely a result of deep fluid circulation along major extensional faults in the area.

©Copyright by Darrick E. Boschmann

November 29, 2012

All Rights Reserved

Structural and Volcanic Evolution of the Glass Buttes Area, High Lava Plains, Oregon

by
Darrick E. Boschmann

A THESIS

submitted to

Oregon State University

in partial fulfillment of
the requirements for the
degree of

Master of Science

Presented November 29, 2012
Commencement June 2013

Master of Science thesis of Darrick E. Boschmann presented on November 29, 2012

APPROVED:

Co-Major Professor, representing Geology

Co-Major Professor, representing Geology

Dean of the College of Earth, Ocean and Atmospheric Sciences

Dean of the Graduate School

I understand that my thesis will become part of the permanent collection of the Oregon State University libraries. My signature below authorizes release of my thesis to any reader upon request.

Darrick E. Boschmann, Author

ACKNOWLEDGMENTS

The author gratefully acknowledges the support for this project from the U.S. Department of Energy, Assistant Secretary for Energy Efficiency and Renewable Energy, Geothermal Technologies program under a cooperative agreement with Golden Field Offices, DE-EE0002836 for innovative exploration technologies under the '*Merging high resolution geophysical and geochemical surveys to reduce exploration risk at Glass Buttes, Oregon*' project.

On a more personal note, I want to thank my advisors Dr. John Dilles and Dr. Andrew Meigs for their dedication and encouragement through the research and writing of this thesis. I have benefited greatly from your continued support and guidance throughout this project, and your demonstrated faith in my abilities has more than once kept me on track during times of doubt and bewilderment.

I also want to give a special thanks to Brigette Martini, Patrick Walsh, and others at Ormat Nevada Inc. for making this research possible both financially and conceptually. Many Thanks to Brigette for taking the time to talk to a humble mudlogger one rainy day on a drill rig in Hawaii, and for pointing me in the direction of a fantastic opportunity when I needed it most. Many thanks to Patrick for spearheading the project, and for providing so many resources and opportunities that have helped make this project a success.

I would also like to acknowledge Rick Conrey of Washington State University for providing support in getting the Bruker instrument operating; Ian Madin with the Oregon Department of Geology and Mineral Industries for providing assistance with LiDAR visualization and interpretation; Dr. Michael Cummings of Portland State University for digging through the archives to pull up long lost data from the 1980's; my field assistant Jake Clarno for being handy with a sledge, and for his companionship around the fire on many high desert nights; and Officer Evan Olsen of the Albany Police department for recovering my stolen laptop at a time when it felt as if all hope was lost. Finally I wish to thank all of the students, faculty, and staff of the OSU department of Geosciences for their input, friendship, and support during my tenure at OSU.

TABLE OF CONTENTS

	<u>Page</u>
Introduction.....	1
Geologic setting	1
Study rational and key questions	5
Methods of study	6
LiDAR based mapping	6
Gravity survey.....	6
Airborne hyperspectral mineral mapping	7
Geochemical map unit correlation	7
Geochronology by $^{40}\text{Ar}/^{39}\text{Ar}$ incremental heating	13
Stratigraphy.....	14
Introduction.....	14
Late Miocene dacite to rhyolite lava flow and dome facies	18
Pliocene to Pleistocene basalt to basaltic andesite lava flows and tuffs	22
Structure.....	27
Faults.....	27
Timing of deformation.....	35
Magnitude and rate of extension.....	36
Discussion.....	41
Tectonomagmatic summary of the Glass Buttes area.....	41
Geothermal activity.....	45
Conclusions.....	52
References.....	55

LIST OF FIGURES

<u>Figure</u>	<u>Page</u>
1. Location of field area and regional tectonic setting.....	2
2. Sample location map.....	8
3. Bruker pXRF vs. conventional XRF dispersion plots	12
4. Simplified geologic map of the Glass Buttes area	15
5. Legend for simplified geologic map	17
6. Measured stratigraphic columns	19
7. Generalized stratigraphic column	20
8. $^{40}\text{Ar}/^{39}\text{Ar}$ age spectra.....	21
9. Geochemical correlation plots – all data.....	24
10. Geochemical correlation plots – northeast section	26
11. Fault map	28
12. Slickenline stereonets.....	30
13. Bouger gravity anomaly map showing inferred faults.....	32
14. Generalized regional cross sections	34
15. Measured cross sections 1-6 and extension calculations	37
16. Measurement of extension across LiDAR profiles	38
17. Regional Tectonic Model.....	45
18. Hyperspectral mineral map	47
19. Temperature gradient interpolation map.....	49

LIST OF TABLES

<u>Table</u>	<u>Page</u>
Table 1. Comparison of Bruker pXRF and USGS standards.....	11
Table 2. Repeat analysis for assessment of Bruker pXRF precision	11
Table 3. Summary of $^{40}\text{Ar}/^{39}\text{Ar}$ age determinations	16
Table 4. Characteristic compositional ranges for chemical stratigraphic units	23
Table 5. Extension magnitude and rate for cross sections 1-6.....	38

LIST OF APPENDICES

<u>Appendix</u>	<u>Page</u>
Appendix A: Whole rock geochemistry (conventional XRF)	58
Appendix B: Whole rock geochemistry (Bruker pXRF)	63
Appendix C: Calibration curves and parameters for Bruker pXRF	71
Appendix D: Detailed lithologic descriptions.....	88
Appendix E: Summary of $^{40}\text{Ar}/^{39}\text{Ar}$ incremental heating (this study).....	94
Appendix F: Sample location map – keyed to geochemical units	100

(Digital data supplement located in the pocket at the back of the book)

LIST OF PLATES

Plate 1: Geologic map and cross-sections of the Glass Buttes area

(Plates are located in the pocket at the back of the book)

INTRODUCTION

Geologic Setting

The Glass Buttes volcanic complex is a cluster of bimodal (basalt-rhyolite), Miocene to Pleistocene age lava flows and domes located in Oregon's High Lava Plains (HLP) province, a broad region of Cenozoic bimodal volcanism in south-central Oregon (Fig. 1). Silicic volcanic rocks within the HLP are progressively younger from east to west, ranging from ~12 Ma in the east to <0.01 Ma to the west at Newberry Caldera (Ford, 2011; Jordan et al., 2004; McKee et al., 1976; Walker, 1974). Basaltic volcanic rocks in the HLP show no such spatial-temporal trend, rather, basaltic rocks ranging from ~10 to 0.44 Ma are widely distributed across the region (Ford, 2011; Jordan et al., 2004).

The HLP is deformed by northwest-striking faults of the Brothers Fault Zone (BFZ), a diffuse, ~N40°W trending zone of en echelon faults cutting ~250 km obliquely across the HLP province (Fig. 1). Individual fault segments within the BFZ are typically <20 km long, strike ~N40°W and have apparent normal separation with 10-100 m throw (Lawrence, 1976; this study). A smaller population of ~5-10 km long faults striking ~N30°E exhibit mutually cross cutting relationships with the dominant northwest-striking faults (Johnson, 1995; Lawrence, 1976; Trench, 2008; Trench et al., 2012).

To the west the BFZ appears to bend northward merging with normal faults of the Central Cascade graben, and to the east the zone appears to terminate against the Steens Mountain normal fault escarpment, however, Walker (1981) suggests that the BFZ may curve southward into Nevada, or continue further east beyond Jordan Valley near the Idaho border. To the South of the BFZ the northwest Basin and Range province

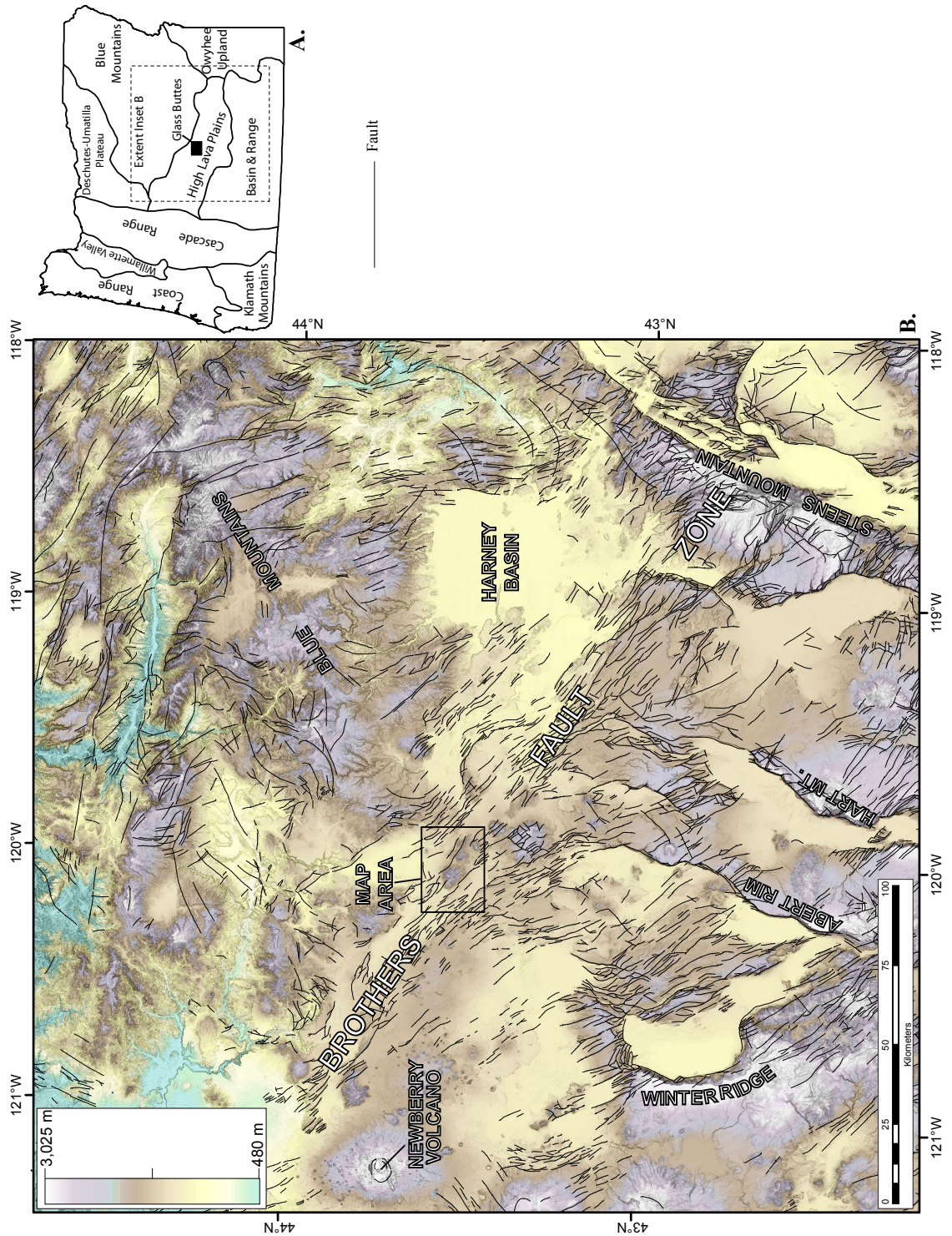


Figure 1: (A) Physiographic provinces of Oregon showing location of the Glass Buttes Mapping area. (B) Hillshade map of the High Lava Plains (HLP), Northwest Basin and Range (NWR), and southern Blue Mountains provinces highlighting the location of northwest striking Brothers Fault Zone (BFZ) faults and major northeast striking Basin and Range faults. Fault Layer from Walker, G.W. and Macleod, N.S., 1991.

consists of north-northeast striking normal faults with >150 m displacement and diminishing topographic and structural relief northwards approaching the BFZ (Trench et al., 2012). North of the BFZ there is a relatively abrupt transition into the Blue Mountains province that exposes early Cenozoic and pre-Cenozoic rocks brought to the surface during the Blue Mountain-Ochoco Mountains uplift (Fig. 1) (Walker, 1981; Scarberry, 2008; (Trench et al., 2012).

At present there are limited geologic ages to constrain the timing of deformation across the BFZ and NWBR. At Duck Creek Butte, near the northern tip of the Steens Mountain escarpment, geologic mapping showed that northwest-striking faults were active as early as 10.32-9.7 Ma, and that north-northeast-striking faults were active before 10.4 Ma (Johnson, 1995). Near the southern end of the Steens Mountain escarpment (Fig 1), an angular unconformity between the Steens Basalt and Oligocene and older volcanic rocks suggests between 5° and 20° of tilting before 16.6 Ma (Langer, 1991; Minor et al., 1987). Along the Abert Rim fault, mapping by Scarberry (2010) demonstrates that northwest-striking faults formed between ~8.9 and 7.5 Ma, and presents evidence of extension as early as ~22 Ma. East of the Harney Basin, (Millard, 2010) sedimentary deposits in syntectonic basins constrain the onset of northeast-striking faults to 15.5 Ma, and demonstrate that slip rates slowed after ~7 Ma (Millard, 2010).

The kinematic relationship between the Brothers Fault Zone, faults of the Northwest Basin and Range and other features in the region is complex and contested. Kinematic models for BFZ deformation in the context of NWBR faulting and regional tectonics have been limited by a lack of reliable kinematic indicators, and a paucity of detailed data constraining the timing of faulting across the region. (Donath, 1962)

attributed the fault geometry in the Winter Ridge area to a reorientation of principal stress axes. In his model an initial N-S horizontal maximum principal stress field produced a series of NW- and NNE-striking conjugate strike slip shears, which formed a set of polygonal fault blocks. With a relaxation of the horizontal principal stress field, these blocks were subsequently uplifted or down-dropped, resulting in the vertical dip-slip offset seen today. Lawrence (1976) hypothesized that large-scale extension in the Basin and Range province was separated from the relatively unextended Blue Mountains province to the north by a right-lateral strike-slip fault zone, and he interpreted the BFZ as an intracontinental Riedel shear transform comparable to the Garlock fault of southern California. Scarberry et al. (2008) challenged this model and noted the lack of observed strike-slip displacement and increased fault density within the Brothers Fault Zone near the northern tips of major normal faults of the Northwest Basin and Range. He proposed that faults within the Brothers Fault Zone represent dilatational fractures associated with the tips of propagating north-northeast-striking Basin and Range Faults. Trench et al. (2012) expanded on this hypothesis, suggesting deformation in the BFZ is due to a combination of “horsetail faulting” at the tips of propagating NWBR faults, extensional deformation associated with basaltic magma emplacement, and transtension associated with the clockwise rotation of the central Oregon block (e.g., (McCaffrey et al., 2007).

High average heat flow ($90.8 \pm 4.8 \text{ mW m}^{-2}$) and elevated average geothermal gradients ($82.2 \pm 5.6 \text{ }^{\circ}\text{C/km}$) across the High Lava Plains (Blackwell, 1982), and the presence of hydrothermal alteration have motivated past and present geothermal resource exploration at Glass Buttes. Temperature gradient drilling by Phillips Petroleum and others between 1977-1981 defined a local geothermal anomaly underlying the Glass

Glass Buttes volcanic complex, and reported a maximum gradient of 224 °C/km (Benoit, R.W., 1981). In 2008 Ormat Nevada Inc., with support from the U.S. Department of Energy began a renewed geothermal exploration program at Glass Buttes. The current study seeks to supplement a suite of high-resolution geophysical and geochemical techniques employed by Ormat to reduce exploration risk at Glass Buttes.

Study rationale and key questions

Previous geologic mapping at Glass Buttes (e.g. Ciancanelli, 1979; (Berri, 1982; Ciancanelli, 1979; Johnson, 1984; Roche, 1987) primarily focused on the lithostratigraphy, petrology, geochemistry and hydrothermal alteration of the silicic rocks that constitute the main Glass Buttes rhyolite complex. Much less work has focused on the surrounding basalt flow stratigraphy, and what the younger, onlapping basaltic units tell about the post-silicic structural evolution of the area.

LiDAR based geologic mapping of the Glass Buttes area, supported by geochemical rock unit correlation, airborne hyperspectral imaging, detailed gravity surveys, and $^{40}\text{Ar}/^{39}\text{Ar}$ ages were collected and provide constraints on the timing and association between faulting, silicic volcanism, basaltic volcanism, hydrothermal alteration, and modern geothermal activity in and around the Glass Buttes volcanic complex. These data are used to address the following key questions: (1) What is the structural style of the Glass Buttes area and the BFZ broadly? (2) What is the timing of faulting and volcanism, and their relationship to each other? (3) How has the rate and style of deformation varied through time? (4) How is the current geothermal system related to the magmatism, alteration and faulting at Glass Buttes?

METHODS OF STUDY

LiDAR based mapping

Field geologic mapping was undertaken to establish the stratigraphic and cross-cutting relationships between faults, basaltic rocks, silicic rocks, hydrothermal alteration events, and sedimentary deposits in and around the Glass Buttes complex. Light Detection and Ranging data (LiDAR) from the Glass Buttes area with a resolution of one meter (x-y), ~5cm (z) was collected by Watershed Sciences, Inc. (Corvallis, OR) over an area of ~350 km² in June 2010. Processing of LiDAR data into a ground classified points, bare-earth DEM was completed by Watershed Sciences, Inc. Surface fault expressions were identified from the LiDAR bare-earth model in ArcGIS by variable illumination hillshading, elevation contouring and slope analysis tools including slope mapping and slope-shade visualizations, and by field observation of offsets, fault scarps and lineaments. A 1:12000 scale, LiDAR bare-earth elevation model was used as a base map for field investigations, which facilitated identification of outcrops in poorly exposed areas and allows the detection of subtle, low-relief fault scarps.

Gravity survey

A ground-based gravity survey was conducted by Zonge International in 2009 and 2010. A detailed survey of 180 gravity stations were acquired along five profile lines in June, 2010, and compiled with an additional 355 gravity stations from a previous regional survey (Pearce, 2011).

Airborne hyperspectral mineral mapping

Airborne hyperspectral scanner imagery was flown with the HyMap Sensor (Integrated Spectronics, Ltd) and processed by HyVista Corporation in August 2009 (Hussey, 2010). The acquisition consisted of 14 flight lines over an area approximately 300 km². HyMap is an airborne hyperspectral scanner delivering 126 bands of imagery over the 450 nm to 2500 nm corresponding to the short wave infrared (SWIR) spectral interval. Spatial resolution is generally 3 m, however resolution changes depending on local topography. SWIR data is useful because numerous common minerals display absorption in the SWIR spectral interval, and therefore HyMap can be used to identify the presence and distribution of hydrothermal alteration minerals at the surface (Martini, 2010).

Geochemical map unit correlation

Correlation of basaltic rock outcrops to construct mappable lava flow and other units was done by field observation of mineralogical and textural characteristics is supported by whole-rock geochemistry. Analysis of major and trace element composition of 24 volcanic rock samples was conducted at the Washington State University GeoAnalytical Laboratory by X-ray Fluorescence (Johnson et al., 1999) (Fig. 2; Appendix A). Measurements of an additional 78 samples were made using a Bruker

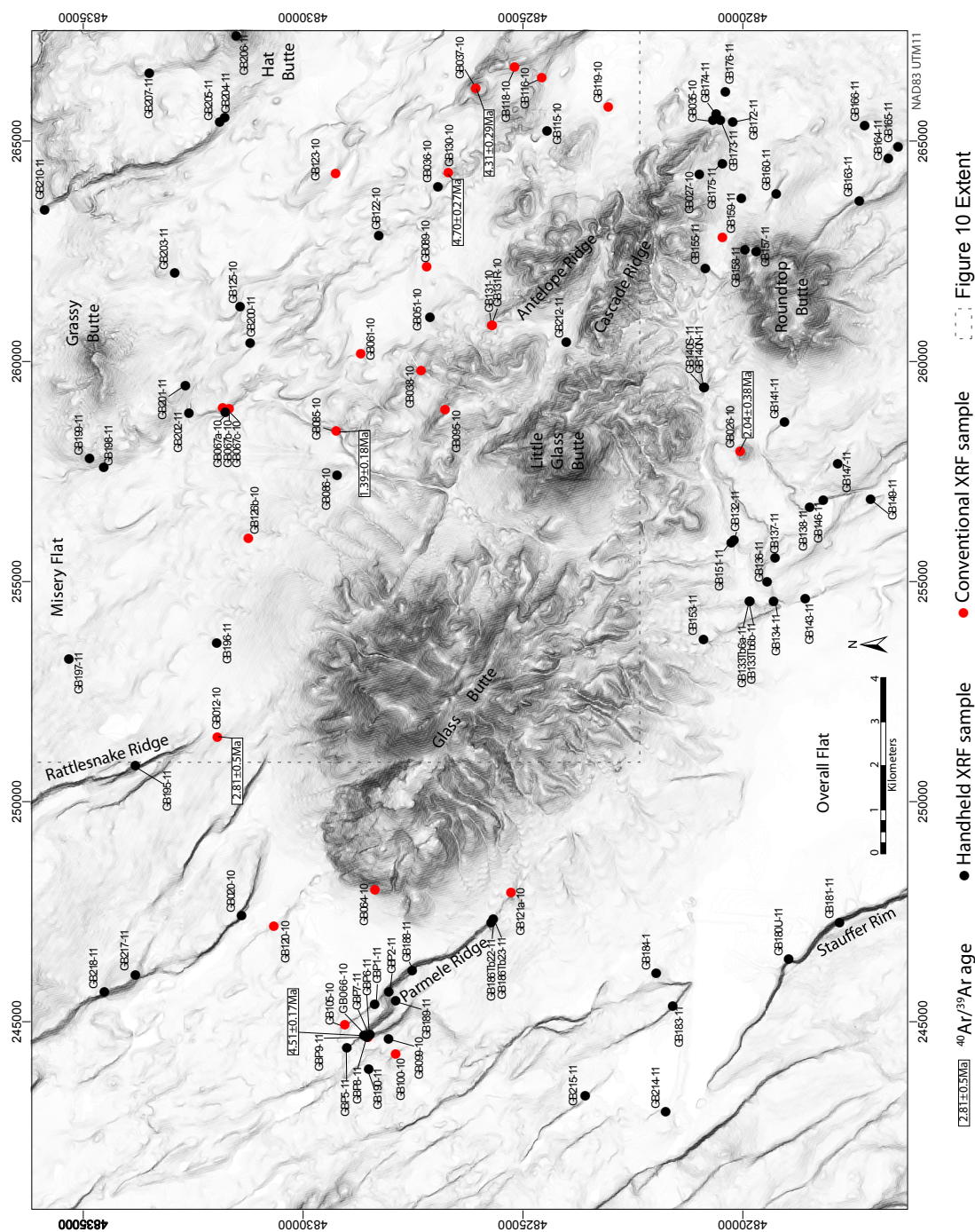


Figure 2: Sample location map for conventional XRF, handheld XRF, and $^{40}\text{Ar}/^{39}\text{Ar}$ age samples. Red symbols: conventional XRF; black symbols: Bruker portable XRF.

Tracer 5 field-portable XRF (pXRF) instrument (Fig. 2; Appendix B). This instrument consists of a portable analyzer incorporating a rhodium-based excitation source and a 30 mm² XFLASHTM Silicon Drift Detector (SSD) connected to a laptop for data acquisition and analysis. Hand-picked, fresh rock chips were ground to a fine powder for 1 minute in a steel ring mill for analysis. All measurements were made using the bench top stand instrument configuration in which powdered samples in XRF cups were placed over the sample window under a removable safety shield.

Spectra were obtained by exciting samples with the rhodium X-ray tube operated at 40 keV/25 mA for 240 seconds. Spectral intensities were corrected and quantified using a new empirical calibration developed in collaboration with Richard Conrey (Conrey et al., 2012) using the Bruker SpectraEDX software and conventional XRF data from 19 Glass Buttes basalt samples previously analyzed at WSU as standards (Appendix C).

The accuracy of the new basalt calibration for the Bruker pXRF is demonstrated for select examples in Table 1 and Figure 3, which show a comparison of results from the Bruker handheld unit and accepted values for USGS standards BCR-2, BHVO-2, BIR-1 and DNC-1. Figure 3 shows detailed dispersion plots comparing results of the Bruker pXRF to USGS standards. Data obtained from the Bruker pXRF are compared to the USGS sample standard values and plot close to the ideal 1:1 line ($R^2 = 0.97-0.99$; $m=0.92-1.1$; $b=0.02-14.5$), indicating that the Bruker instrument reproduces standard concentrations to within acceptable limits using the analytical protocols described above. Table 1 summarizes the percent difference between Bruker results and USGS standards. As expected, the greatest relative difference occurs at very low concentrations (e.g. BIR-

1: Nb, K₂O). In general, the percent difference of the Bruker data relative to the standard ranges from <1 to 33%, with most elements ~5-8%.

Repeat analysis of a single sample was done to assess the internal precision of the Bruker instrument. Table 2 illustrates that ten separate analyses of sample GB174-11 resulted in only minimal fluctuations ($1\sigma = 0.00$ to 4.98) in concentrations of elements of interest for this study (Ni, Sr, Zr, K₂O, TiO₂, MnO, FeO). Some of this variation may be a result of minor compositional variation within the sample itself, or slight changes in powder packing or geometry between analyses.

Table 1: Comparison of Bruker portable XRF an USGS standards in whole rock powders.

	BCR-2			BHVO-2			BIR-1			DNC-1		
	USGS	Bruker	% diff.*	USGS	Bruker	% diff.*	USGS	Bruker	% diff.*	USGS	Bruker	% diff.*
K ₂ O (wt.%)	1.79	1.69	5.6	0.52	0.44	15.4	0.03	0.02	33.3	0.23	0.2	13.0
CaO (wt.%)	7.12	6.97	2.1	11.4	10.62	6.8	13.3	12.71	4.4	11.5	10.83	5.8
TiO ₂ (wt.%)	2.26	2.34	3.5	2.73	2.73	0.0	0.96	0.98	2.1	0.48	0.53	10.4
MnO (wt.%)	0.196	0.2	2.0	0.167	0.17	1.8	0.175	0.17	2.9	0.15	0.148	1.3
FeO (wt.%)	12.43	12.22	1.7	11.08	11.33	2.2	10.18	10.02	1.6	8.97	9.13	1.7
Ni (ppm)	-	16	-	119	107	10.1	170	167	1.8	247	232	6.1
Sr (ppm)	346	334	3.5	389	384	1.3	110	102	7.3	144	127	11.8
Y (ppm)	37	41	10.8	26	29	11.5	16	17	6.3	18	18	0.0
Zr (ppm)	188	184	2.1	172	168	2.3	18	18	0.0	38	36	5.3
Nb (ppm)	-	11	-	18	16	11.1	0.6	2	200	3	3	0.0

$$*\%difference = \left| \frac{USGS - Bruker}{USGS} \right| \times 100\%$$

Table 2: Repeated analyses (n = 10) of basalt sample GB174-11 utilized as a standard to assess the precision of the Bruker portable XRF instrument.

RUN	Ni	Sr	Zr	K ₂ O	TiO ₂	MnO	FeO
1	65	275	193	0.57	2.41	0.207	11.94
2	71	278	197	0.57	2.44	0.21	12.09
3	71	271	198	0.58	2.43	0.21	12.08
4	67	274	196	0.58	2.43	0.211	12.1
5	73	274	195	0.57	2.39	0.209	11.98
6	72	275	197	0.56	2.37	0.208	11.97
7	74	279	199	0.58	2.45	0.213	12.24
8	82	281	199	0.58	2.45	0.213	12.23
9	77	276	199	0.59	2.44	0.213	12.2
10	77	286	203	0.59	2.48	0.215	12.35
MEAN	72.90	276.90	197.60	0.58	2.43	0.21	12.12
MIN	65.00	271.00	193.00	0.56	2.37	0.21	11.94
MAX	82.00	286.00	203.00	0.59	2.48	0.22	12.35
STDEV	4.98	4.28	2.72	0.01	0.03	0.00	0.13
StdError	0.07	0.02	0.01	0.02	0.01	0.01	0.01

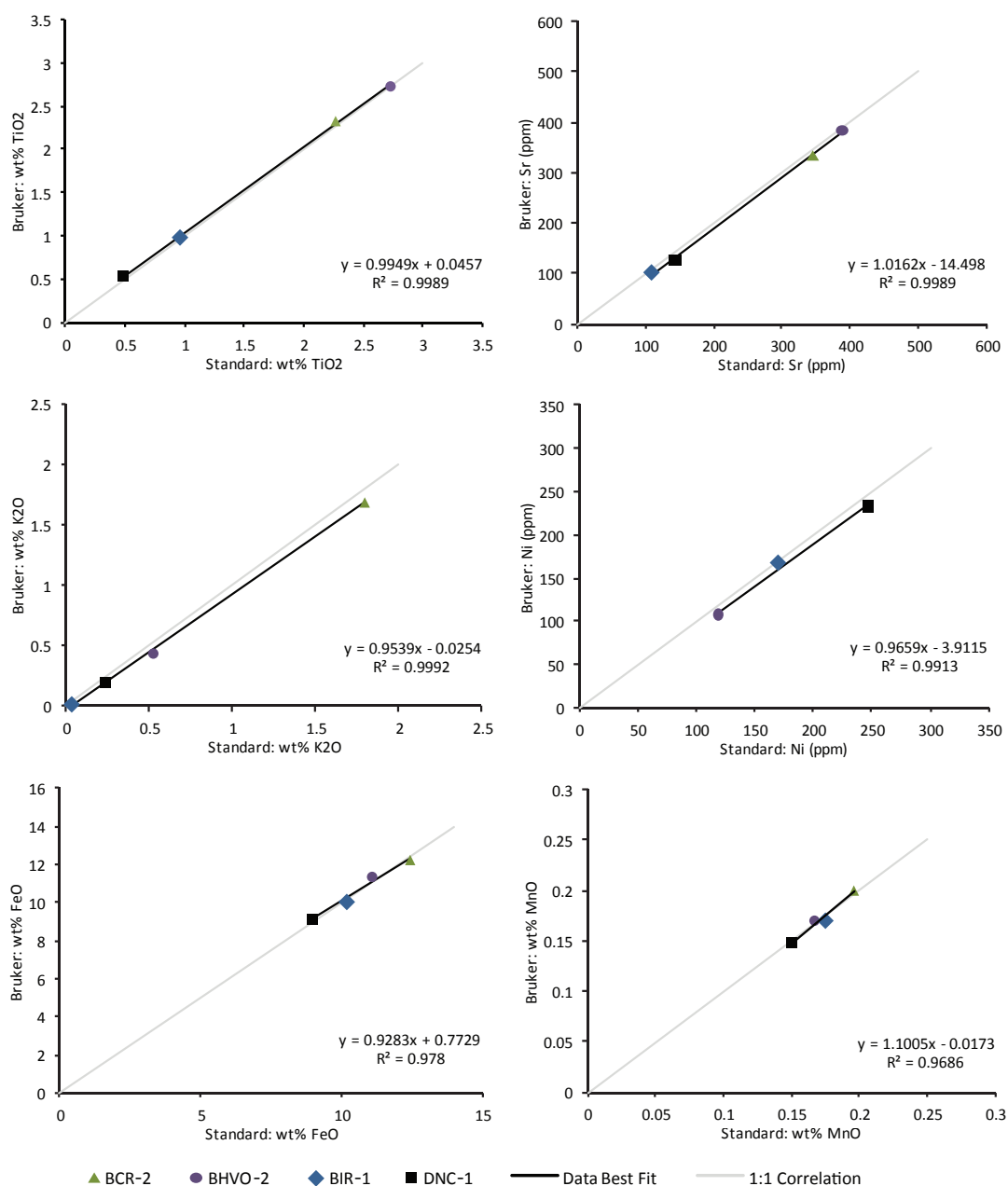


Figure 3: Bruker handheld XRF compared with known USGS standards (BCR-2, BHVO-2, BIR-1, DNC-1) for concentrations of select elements and oxides in whole rock powders.

Geochronology by $^{40}\text{Ar}/^{39}\text{Ar}$ incremental heating

$^{40}\text{Ar}/^{39}\text{Ar}$ ages for six basalt rock samples were determined in the noble gas mass spectrometry laboratory of the College of Earth, Ocean and Atmospheric Sciences Oregon State University (locations Fig. 2). Fresh basalt samples were crushed and sieved to a -30+60 mesh (0.6-0.25 mm), washed in a dilute HNO_3 ultrasonic bath, rinsed with DI water, and hand-picked to obtain ~100mg of clean groundmass. Samples were irradiated in evacuated silica vials for 6 hours in the Oregon State University TRIGA Reactor, and then heated incrementally using a 10W CO_2 laser. The isotopic Ar composition was measured at each heating step using a MAP-215/50 mass spectrometer. All six ages meet the criteria for a reliable estimate of the crystallization age: plateau ages are the weighted means of three or more heating step ages comprising over 50% of the total $^{39}\text{Ar}_\text{K}$ gas released and are concordant with isochrons with initial $^{40}\text{Ar}/^{39}\text{Ar}$ intercepts calculated from Ar compositions of the same steps (Longo et al., 2010). The $^{40}\text{Ar}/^{39}\text{Ar}$ ages were calculated using ArArCALC v2.2 software (Koppers, 2002), and are reported as plateau ages with a 2σ error at the 95% confidence interval.

STRATIGRAPHY

Introduction

Geologic mapping, geochemical rock unit correlation and radiometric ages from this study provide new constraints on the volcanic stratigraphy of the Glass Buttes volcanic complex. Rocks exposed in the study area can be divided into three broad stratigraphic groups: (1) Late Miocene dacite to rhyolite lava flow and dome facies of the Glass Buttes edifice, (2) Late Miocene and Pleistocene basalt to basaltic andesite lava flows and tuffs that lap onto the margins of the silicic complex, and (3) Pleistocene to Holocene sedimentary deposits (Figs. 4, 5, 6, 7; Plate 1). Lithologic descriptions of the silicic map units from (Roche, 1987), basaltic units (this study), and surficial deposits (this study) are given in Appendix D and summarized in Figure 7. Figure 6 illustrates measured stratigraphic columns that establish relative ages of the mafic and silicic units in the map area. Age data from this study are combined with existing $^{40}\text{Ar}/^{39}\text{Ar}$ ages (Ford, 2011; Iademarco, 2009; Jordan et al., 2004) to support mapped stratigraphic relationships and crosscutting relations of faults and volcanic units (Table 3; Figure 8; Appendix E).

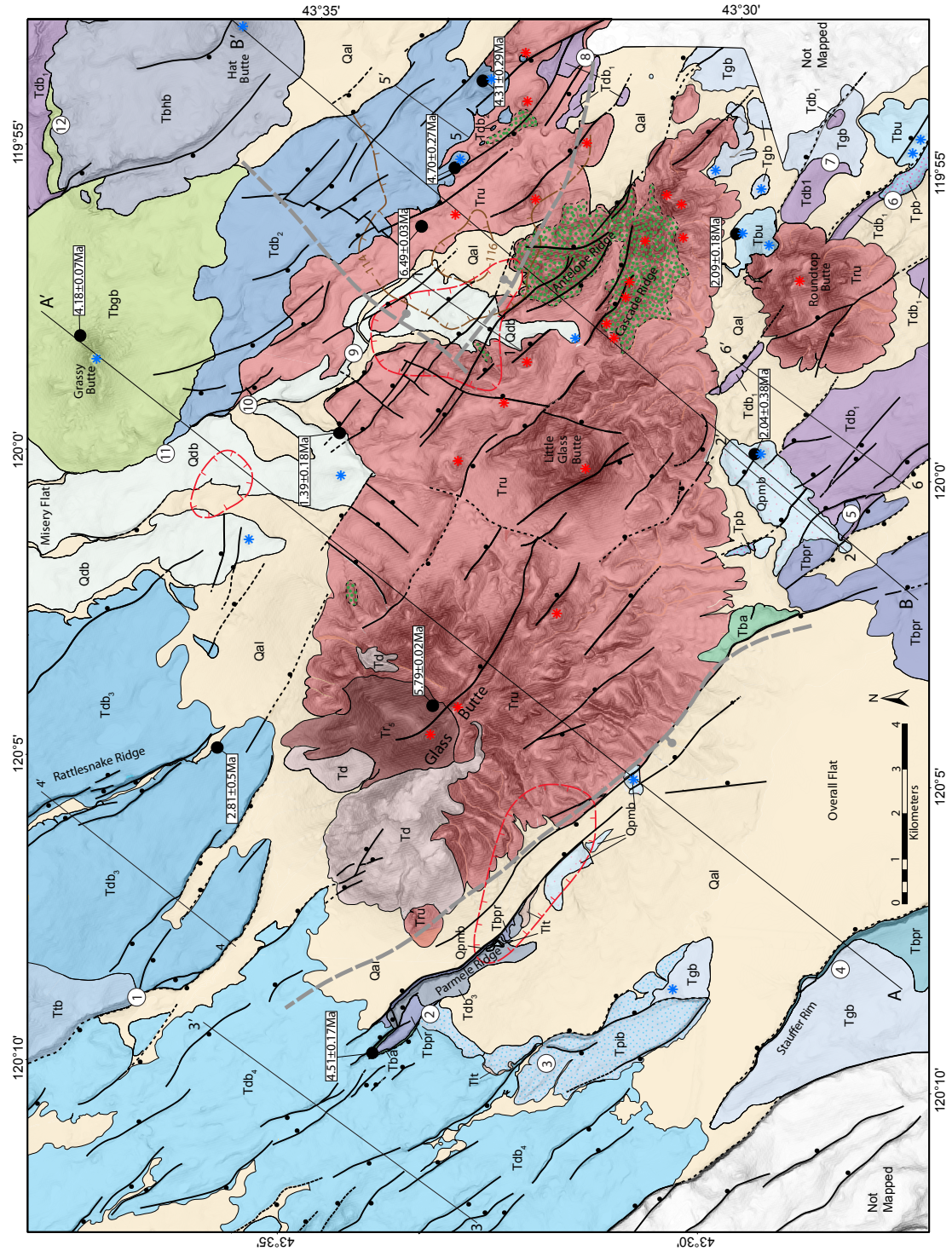


Figure 4: Simplified geologic map of the Glass Buttes volcanic complex. See figure 5 for explanation. Map unit descriptions are found in Fig. 7 and Appendix D; Ar/Ar ages are summarized in Fig. 8 and Table 3; cross sections 1-6, A and B appear in Figs. 14 and 15.

Table 3: Summary of $^{40}\text{Ar}/^{39}\text{Ar}$ age determinations.

Sample no.	Source	Unit	Northing	Easting	Material	Total fusion age (Ma) $\pm 2\sigma$	Plateau age (Ma)			Isochron age (Ma)				
							Plateau age $\pm 2\sigma$	No. of steps Plateau/tal	% ^{39}Ar in plateau	MSWD	Isochron age $\pm 2\sigma$	Initial $^{40}\text{Ar}/^{36}\text{Ar} \pm 2\sigma$	MSWD	Ma preferred age $\pm 2\sigma$
GB130-10	This study	Tdb2	4826660.3	264267.3	groundmass	4.74 \pm 1.29	4.70 \pm 0.27	10/10	100	0.04	4.70 \pm 0.28	295.5 \pm 1.08	0.04	4.70 \pm 0.27
GB037-10	This study	Tdb2	4826032.4	266190.7	groundmass	6.68 \pm 1.74	4.31 \pm 0.29	7/10	90.78	0.02	4.31 \pm 0.43	295.5 \pm 1.39	0.03	4.31 \pm 0.29
GB026-10	This study	Qpmb	4820023.7	257944.5	groundmass	2.96 \pm 0.47	2.04 \pm 0.38	6/10	69.92	0.05	2.04 \pm 0.87	295.5 \pm 3.21	0.06	2.04 \pm 0.38
GB085-10	This study	Qdb	4830218.5	258303.2	groundmass	1.62 \pm 0.29	1.39 \pm 0.18	9/10	96.79	0.02	1.42 \pm 0.38	293.7 \pm 18.12	0.02	1.39 \pm 0.18
GBP7-11	This study	Tbpr	4828479.6	244696.5	groundmass	4.45 \pm 0.25	4.51 \pm 0.17	9/12	92.61	0.04	4.47 \pm 0.46	296.39 \pm 12.1	0.04	4.51 \pm 0.17
GB012-10	This study	Tdb3	4831915.1	251447.4	groundmass	2.98 \pm 0.65	2.81 \pm 0.50	8/9	95.62	0.04	2.89 \pm 0.87	294.63 \pm 7.17	0.04	2.81 \pm 0.50
GB 0701	Iademarco, 2009	Tbgb	4834940	260558.4	whole rock	4.90 \pm 0.33	4.18 \pm 0.14	8/11	94.89	1.83	4.10 \pm 0.12	298.31 \pm 2.13	0.91	4.18 \pm 0.14
MTF 07-04	Ford, 2011	Tr5	4827149	252372.3	whole rock	-	5.79 \pm 0.04	-	-	-	5.74 \pm 0.11	-	-	5.79 \pm 0.04
MTF 07-05	Ford, 2011	Tr1Bx	4827399	262978.2	whole rock	-	6.49 \pm 0.05	-	-	-	6.49 \pm 0.06	-	-	6.49 \pm 0.05
HP-93-29	Jordan, 2004	Tbu	4820426	262809	whole rock	-	2.09 \pm 0.18	-	78	-	1.13 \pm 0.33	302.6	-	2.09 \pm 0.18

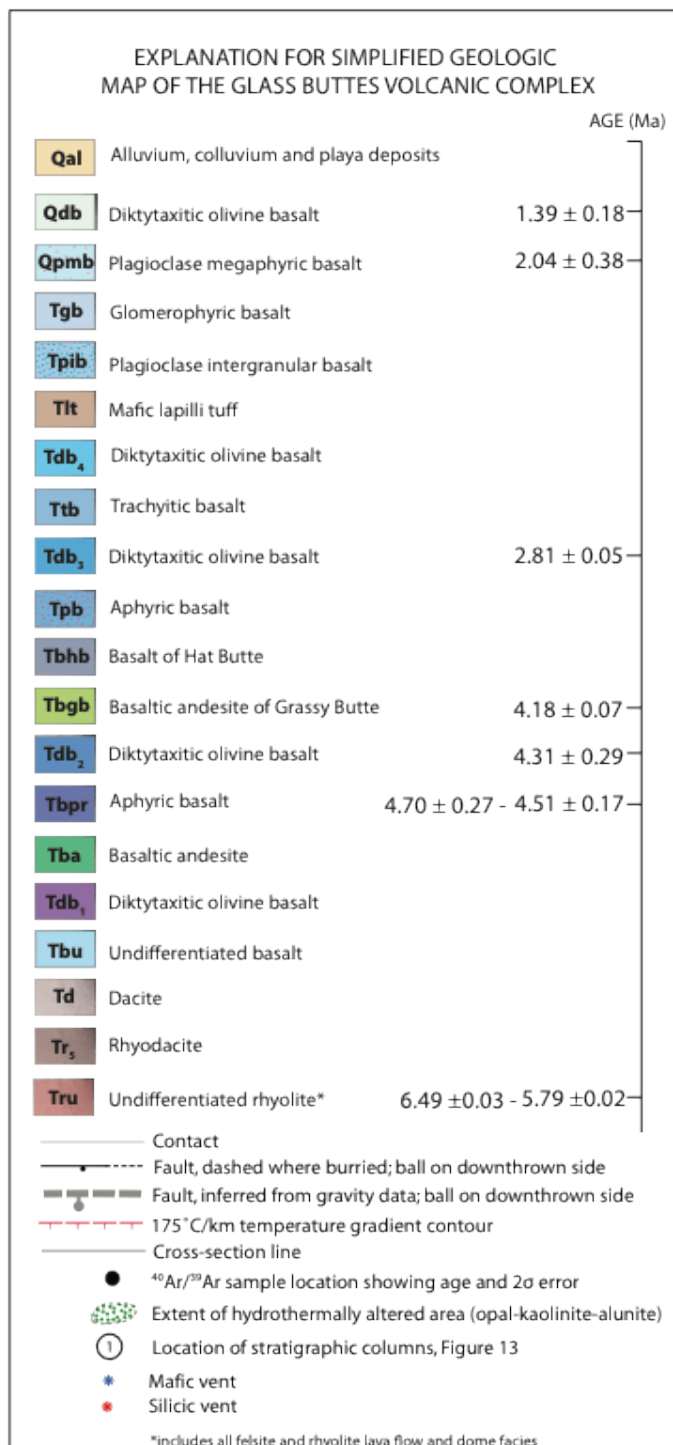
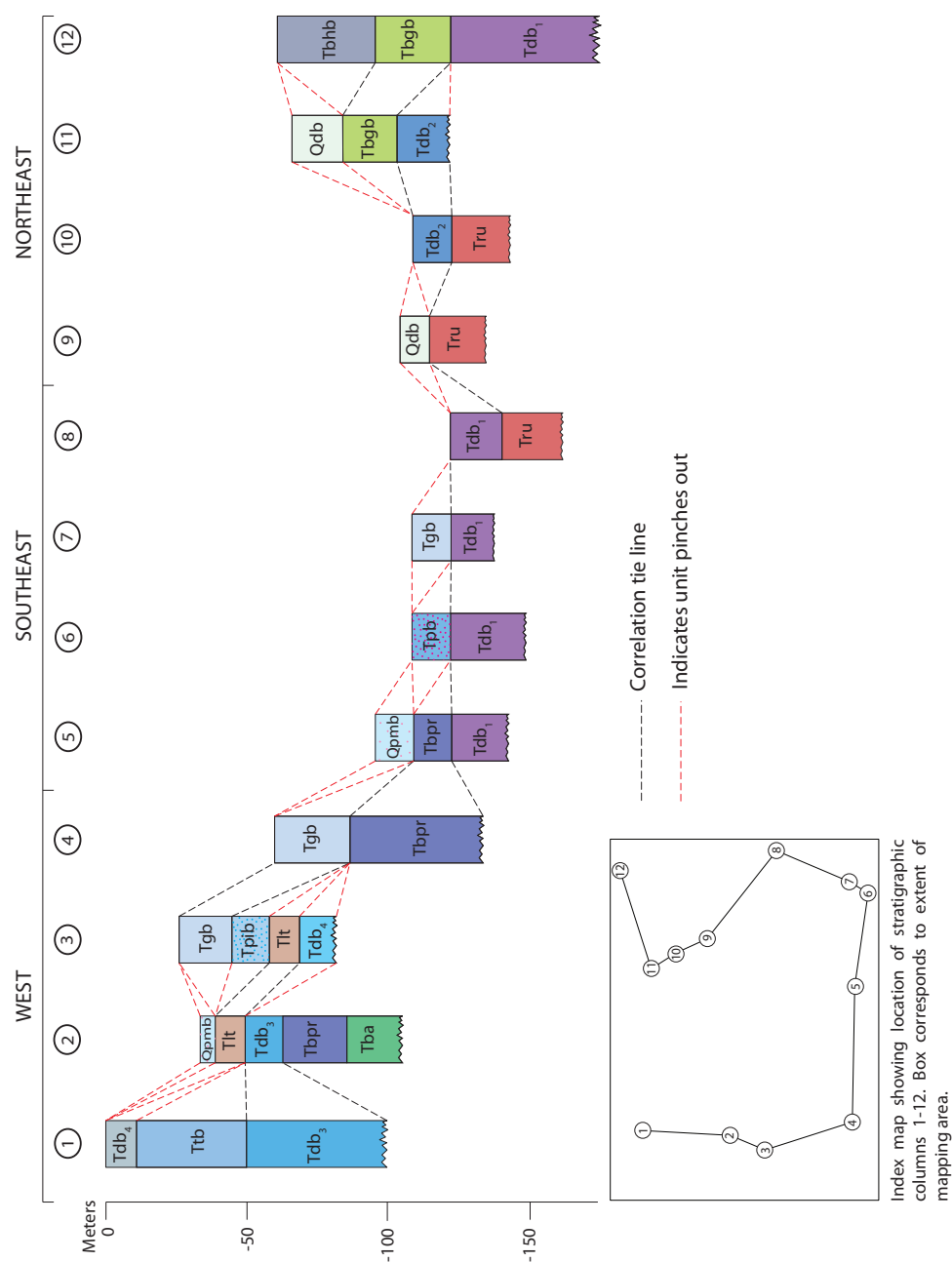


Figure 5: Legend for simplified geologic map of the Glass Buttes volcanic complex. Undifferentiated rhyolite (Tru) includes silicic flow and dome facies units Tr₄, Tr_{1f}, Tr_{1o}, Tr_{1p}, Tr_{bx}, Tr₂ and Tr₃. Detailed descriptions Fig. 7 and Appendix D.

Basaltic lavas and sedimentary deposits were found interbedded with rhyolitic rocks in Phillips well Strat-4, south of Cascade Ridge at a depth of 164 m and again at 250 m, however, these samples are unavailable so correlation with surface exposures was not possible. No exposures of pre-Glass Buttes basement rocks are present in the field area, however (Jordan et al., 2004) report an episode of increased province-wide basaltic volcanism from 7.5-7.8 Ma. These older basalts, and the widespread 7.05 Ma Rattlesnake Tuff (Streck and Grunder, 1995) likely underlie the Glass Buttes rhyolite complex.

Late Miocene dacite to rhyolite lava flow and dome facies

Silicic rocks of the Glass Buttes complex are the oldest rocks exposed in the field area (Figs. 4, 5, 6, 7). The complex is composed primarily of nearly aphyric rhyolite lavas and domes, including facies that range from dense and devitrified interiors to dense vitrophyre to margins or carapaces of pumice, brecciated vitrophyre, and pyroclastic ash as well as locally reworked volcanoclastic sedimentary deposits. The silicic rock unit descriptions presented below are taken largely from detailed mapping by Berri (1982), Johnson (1984), and Roche (1987). $^{40}\text{Ar}/^{39}\text{Ar}$ ages of $6.49 \pm 0.03\text{Ma}$ from a dome north of Antelope Ridge, and $5.79 \pm 0.02\text{Ma}$ at Glass Buttes proper, (Ford, 2011) (Fig.4, Table 3) suggest a local east to west age progression of silicic eruptive centers in the late Miocene, consistent with the regional westward younging trend of silicic rocks across the High Lava Plains.



AGE	COLUMN	THICKNESS	DESCRIPTION
Quaternary	Qal - Qp - Qoa	variable	Alluvium, colluvium and playa deposits.
1.39 ± 0.18 Ma (Qdb)	Qdb	0-7 m	Diktytaxitic olivine basalt lava flows. 0.4-0.5 wt.% K ₂ O, 2.3-2.7 wt.% TiO ₂ , 220-233ppm Sr. Abundant olivine phenocrysts in a groundmass of plagioclase, olivine, clinopyroxene and oxides. 2-5% vesicles.
2.04 ± 0.38 Ma (Qpmb)	Qpmb	0-5 m	Plagioclase megaphyric basalt lava flows. 1-3 cm long plagioclase phenocrysts in a fine-grained groundmass with abundant plagioclase microlites.
Pliocene and Quaternary (?)	Tgb	0-15 m	Plagioclase-olivine glomerophyric basalt lava flows. Round glomerocrysts of olivine and plagioclase up to 1 cm in diameter in a fine-grained groundmass.
	Tpib	0-10 m	Plagioclase intergranular basalt lava flows. ~30% plagioclase phenocrysts with intergranular olivine in a fine-grained groundmass.
	Tlt	0-5 m	Unwelded mafic lapilli tuff . Tan, brown, black pumice and lithics in a dark gray ashy matrix.
	Tdb ₁	0-30 m	Diktytaxitic olivine basalt lava flows. 74-119 ppm Zr, 0.17-0.19 wt.% MnO.
	Ttb	0-30 m	Plagioclase trachytic basalt lava flows. Dark gray-black, fine grained basalt with abundant flow-aligned plagioclase laths. Well defined platy jointing.
	Tdb ₂	0-5 m	Diktytaxitic olivine basalt lava flows. 0.1-0.2 wt.% K ₂ O, 0.6-1.0 wt.% TiO ₂ , 179-208ppm Sr, 0.97-1.2 Ni/Sr.
Pliocene and Quaternary (?)	Tpb	0-150m	Pyroxene basalt lava flows. 290-298 ppm Sr, 3.2-3.5 Ni/Zr. ~20% pyroxene, ~20% plagioclase, rare <1mm size olivine phenocrysts in groundmass composed of fine plagioclase microlites.
	Tbhb	0-150m	Basalt of Hat Butte . 0.8-0.9 wt.% K ₂ O, 2.6-2.7 wt.% TiO ₂ . Medium-dark gray, 5% plagioclase (1-3mm), rare olivine phenocrysts.
	Tbgb	0-150 m	Basaltic-andesite of Grassy Butte . 1.1-1.3 wt.% K ₂ O, 2.3-2.7 wt.% TiO ₂ . Unconsolidated oxidized, fine-coarse, scoriaceous cinders, bombs and agglutinate. Lava flows are very dark gray-black, fine-grained with ~2% plagioclase phenocrysts generally <1mm.
	Tdb ₃	0-20 m	Diktytaxitic olivine basalt lava flows. 0.4-0.7 wt.% K ₂ O, 1.5-1.8 wt.% TiO ₂ .
	Tbpr	0-20 m	Basalt of Parmele Ridge . Light-medium gray aphyric basalt lava flows. 437-482 ppm Sr.
	Tba	0-15 m	Light-medium gray, aphyric basaltic-andesite lava flows with rare 1-5 cm rhyolite inclusions. 634-666 ppm Sr.
Miocene and Pliocene (?)	Tdb ₄	0-50 m	Diktytaxitic olivine basalt lava flows. 0.2-0.4 wt.% K ₂ O, 1.7-2.0 wt.% TiO ₂ , 0.21-0.23 wt.% MnO, 83-109ppm Zr.
	Td	0-100 m	Dacite lava flows . ~5% plagioclase phenocrysts, 5-10% elongate vesicles.
	Tr ₁	0-300m	Black to gray; pink, often oxidized red rhyodacite lava flows . >10% plagioclase and 2-6% hornblende phenocrysts.
	Tr ₂	0-300m	Rhyolite lava flows (Tr₁) : black to gray; pink, often oxidized red. Common contorted flow banding. <10% plagioclase phenocrysts
	Tr ₃	0-300m	Pyroclastic rhyolite (Tr₂) : Well indurated ash-flow tuff. Clasts of obsidian, pumice, and felsite in a white- to pink-colored rhyolite ash matrix. Broad cross-bedding of cobble-size clasts occurs locally.
	Tr ₄	0-300m	Biotite-phyric lava flows and domes (Tr₃) : 1-2% biotite ± quartz, ± plagioclase, ± sanidine phenocrysts in pumiceous, gray to brown, locally perlitically fractured groundmass. Elongate vesicles comprise 25-40% of the volume. Biotite phenocrysts are <2mm and aligned parallel to flow banding.
Miocene and Pliocene (?)	Undifferentiated basalt	0-600 m	Carapace breccia (Trbx) : Poorly sorted, black, gray, brown pumice clasts in an unaltered gray-brown pumice matrix. Clasts are angular, ranging from pebble to boulder size.
	Tru	0-600 m	Pumice (Tr₁) : Light to dark gray, coarsely vesicular pumice with common perlitic fractures and >50% ovoid-highly elongate vesicles up to a few cm in diameter.
	Tru	0-600 m	Obsidian (Tr₁) : Black, red, brown, mahogany, nonvesicular obsidian flows ranging from massive uniform to strongly flow banded.
	Tru	0-600 m	Felsite (Tr₁) : Lava flows and domes of devitrified gray glass. Weak-moderate vesiculation aligned parallel to moderately-strongly developed, often contorted flow banding. Lithophysae, spherulitic zones, and perlitic fracturing occur locally.
	Tru	0-600 m	
	Tru	0-600 m	

Figure 7: Generalized stratigraphic column for the Glass Buttes area showing lithologic units of Miocene to Quaternary volcanics and surficial sedimentary deposits, their age range based on ⁴⁰Ar/³⁹Ar determinations, and range of thickness.

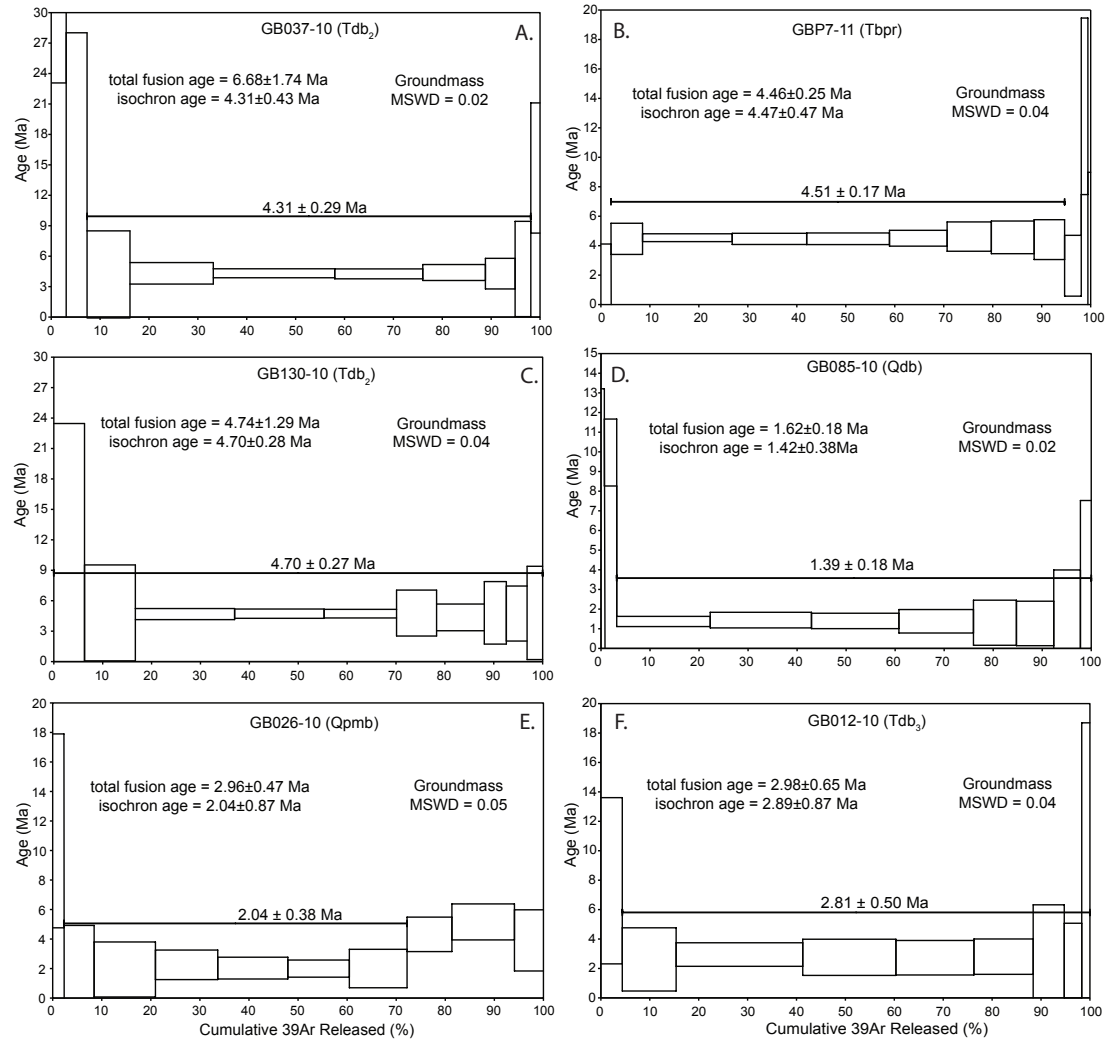


Figure 8: $^{40}\text{Ar}/^{39}\text{Ar}$ age spectra for samples from rock units Tdb₂, Tbpr, Qdb, Qpmb, and Tdb₃. A summary of all available ages is found in Table 3.

Pliocene to Pleistocene basalt to basaltic andesite lava flows and tuffs

Diverse basalt to basaltic andesite lava flows flank the Glass Buttes complex in all directions (Figs. 4, 5, 6, 7). Source vents located within and around the complex are commonly aligned along northwest striking faults. Flows are exposed along intermittent stream channels and degraded fault scarps, often exhibiting well-developed columnar jointing and locally rare platy jointing. Individual flow units are typically 2-10 meters in thickness, and rarely up to 30 meters where flows ponded into the half graben basin to the north of Glass Buttes (see Fig. 1).

Fine-grained, dark-gray to black diktytaxitic olivine basalts form most of the surrounding plateau to the north and west of the Glass Buttes complex. These basalts have distinct diktytaxitic texture, with abundant olivine and plagioclase phenocrysts in a groundmass of plagioclase, olivine, clinopyroxene and oxides and 2-5% vesicles. The diktytaxitic olivine basalts (Tdb₁, Tdb₂, Qdb, Tdb₃, Tdb₄) have been subdivided into distinct chemical stratigraphic sub-units based on whole rock chemical composition. Correlation of basaltic units is based on characteristic mineralogy, texture and whole rock geochemical composition.

Examination of the 102 analyses from conventional XRF and pXRF show that there is significant compositional variability in basaltic lavas at Glass Buttes. Most of the basaltic lava flows fall into one of ten chemical stratigraphic groups (Figs. 9, 10; Table 4; Appendix F), which are distinguished by variations in chemical composition. Figure 9 shows bivariate scatter plots of all XRF data, and geochemical correlations based on variations in K₂O, TiO₂, FeO, MnO, Zr, Sr, and Ni.

Table 4: Characteristic compositional ranges for chemical stratigraphic units.

Unit	Characteristic Compositional Range
Qdb	0.4-0.5 wt.% K ₂ O; 2.3-2.7 wt.% TiO ₂ , 220-233 ppm Sr
Tdb4	74-119 ppm Zr; 0.17-0.19 wt.% MnO
Tdb3	0.1-0.2 wt.% K ₂ O; 0.6-1.0 wt.% TiO ₂ ; 179-208 ppm Sr; 0.97-1.2 Ni/Sr
Tpb	290-298 ppm Sr; 3.2-3.5 Ni/Zr
Tbhb	0.8-0.9 wt.% K ₂ O; 2.6-2.7 wt.% TiO ₂ ; 379-394 ppm Sr
Tbgb	1.1-1.3 wt.% K ₂ O; 2.3-2.7 wt.% TiO ₂
Tdb2	0.4-0.7 wt.% K ₂ O; 1.5-1.8 wt.%TiO ₂
Tpbr	437-482 ppm Sr
Tba	634-666 ppm Sr
Tdb1	0.2-0.4 wt.% K ₂ O; 1.7-2.0 wt.% TiO ₂ ; 0.21-0.23 wt% MnO; 83-109 ppm Zr

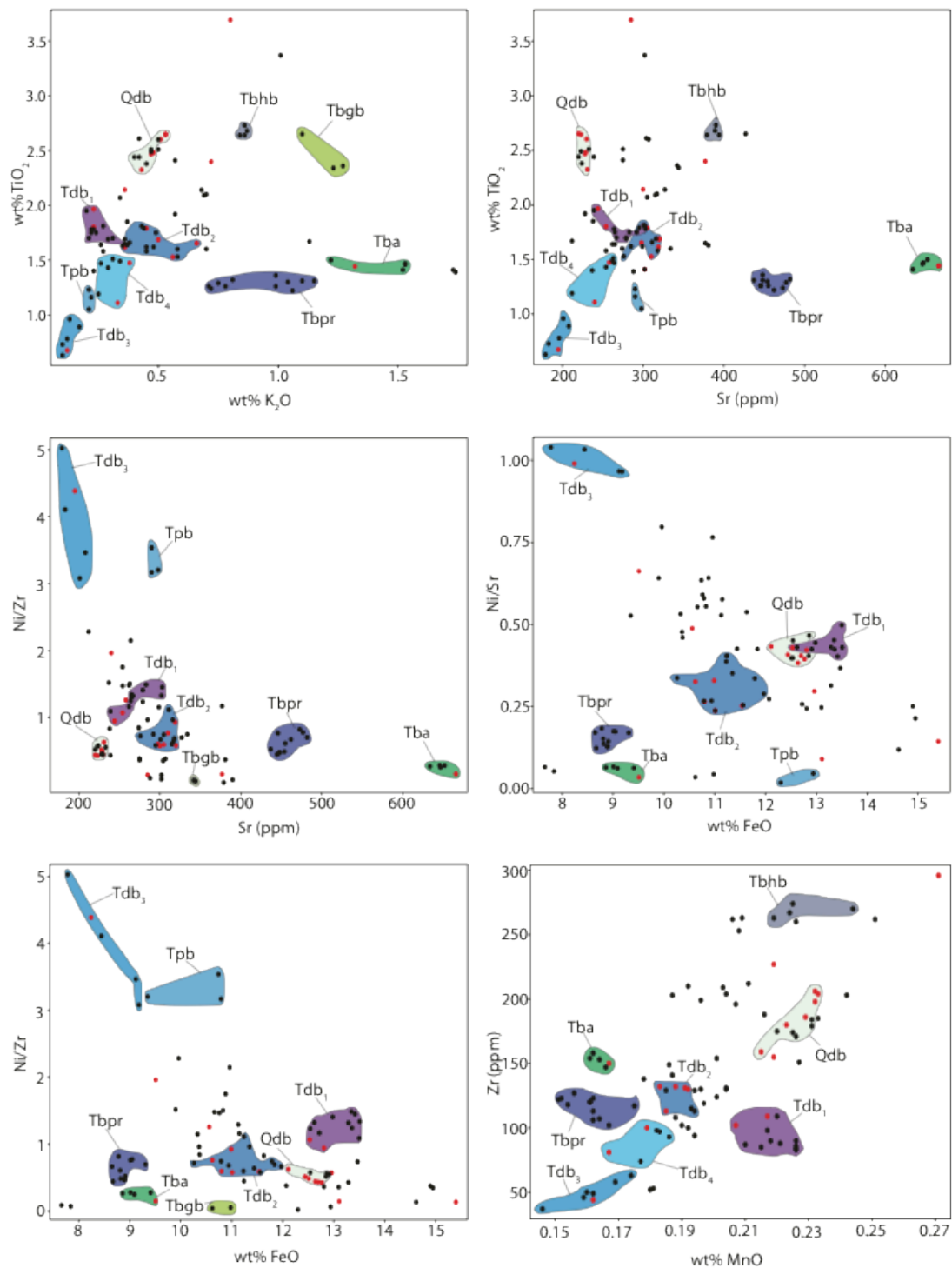


Figure 9: Geochemical variation diagrams for Glass Buttes basalts from conventional (red points) and Bruker handheld (black points) XRF. Colored fields are keyed to stratigraphic units (Figs. 4, 5).

As a result of the low erupted volume and localized nature of basaltic lava flows in the field area, when all data from across the entire mapping area are plotted, as in Figure 9, overlap and scatter within and between geochemical stratigraphic units obscures the distinguishing geochemical fingerprints. In particular, the basalt of Parmele Ridge (Tbpr) and a basaltic-andesite unit (Tba), are easily distinguished by significant enrichments in Sr compared to all other samples across the entire map area.

To resolve this, geochemical correlations are first established over short distances between outcrops by comparison of composition and mapped stratigraphic relations within sampling sub-regions (eg. Fig. 10). Figure 10A depicts sample location, the areal extent of chemical stratigraphic units, and their relation to faults and silicic rocks in the northeast region of the Glass Buttes complex. Field mapping and initial attempts at unit correlation by hand sample texture and mineralogy identified only four distinct volcanic units in the northeast region: silicic rocks of the Glass Buttes complex (Tru – undifferentiated rhyolite used here for simplicity), basaltic-andesite of Grassy Butte (Tbgb), basalt of Hat Butte (Tbhb), and a series of widespread, undifferentiated diktytaxitic, olivine basalt flows and vents. Geochemical subgroups within the diktytaxitic olivine basalts are readily distinguished by small but significant variations in concentrations of K_2O and TiO_2 , and fall into one of four chemical stratigraphic units: Tdb₁, Tdb₂, Tdb₃, and Qdb (Fig. 10B).

Once correlation is established within the limited sub-regions, it is then expanded to include relations between sub-regions where possible. Appendix F shows the location of XRF samples, with location symbols keyed to the 10 chemical stratigraphic units,

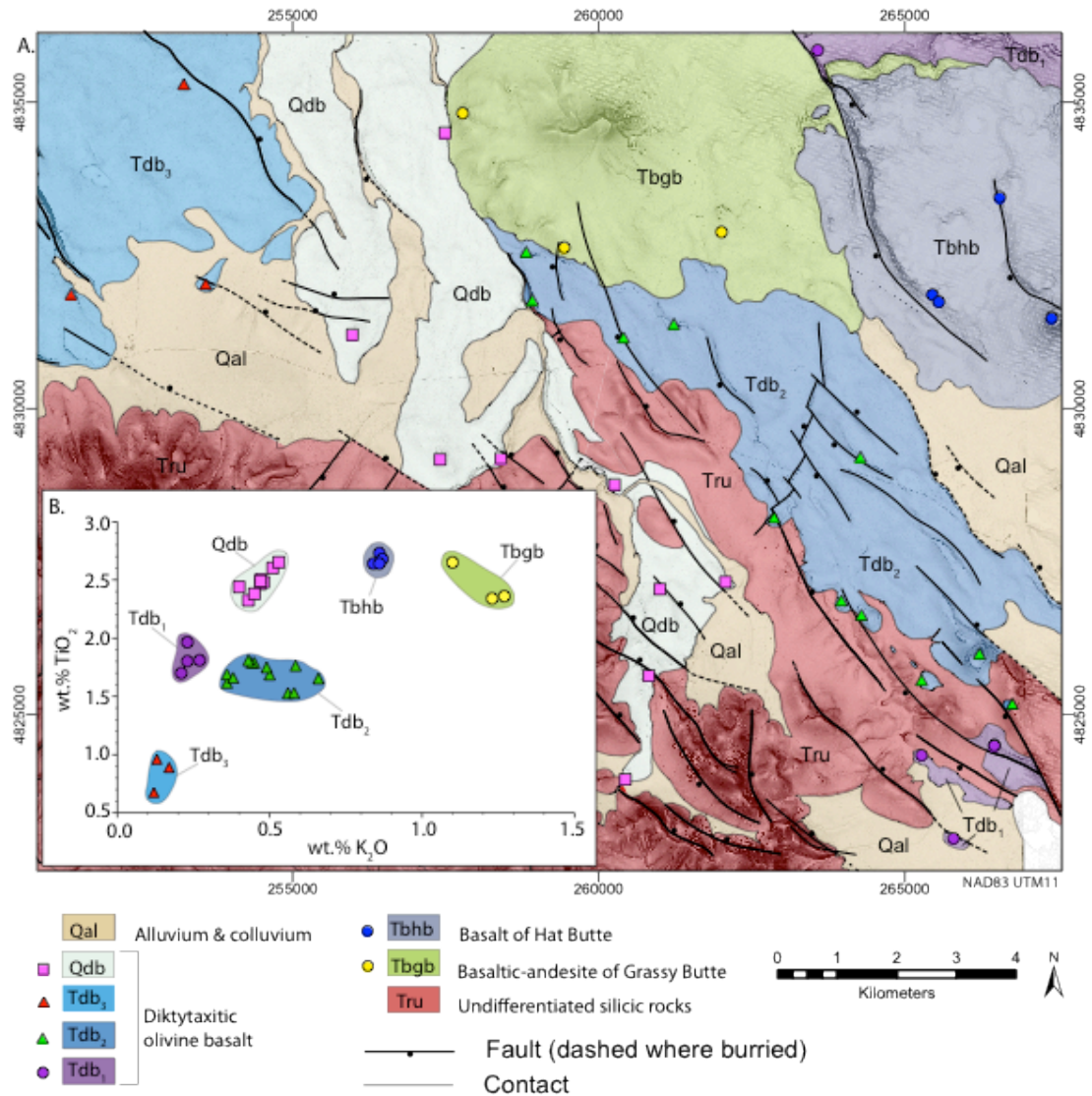


Figure 10: (A) Simplified geologic map of the northeast part of the field area showing sample locations, lithology, and faults. Sample locations are keyed to the inset K_2O v. TiO_2 variation plot (B), illustrating the use of geochemical composition for outcrop correlation.

illustrating the distribution of samples from each unit. Table 4 summarizes the characteristic compositional ranges used to identify samples from each unit.

STRUCTURE

Faults

All faults mapped within the study area exhibit primarily normal displacement with a minor oblique component, and can be broadly grouped into northwest- and northeast-striking populations based on orientation (Fig. 11). The strike of the dominant fault population ranges from N20°W to N60°W, which is similar to strikes of other faults that make up the BFZ to the southeast and northwest (Donath, 1962; Pezzopane and Weldon, 1993). Individual fault segments in this population are generally 2-10 km in length with normal separation of <60 meters (minimum separation value as measured from topographic expression), and are generally spaced 1-2 km apart (Fig. 11). These fault segments often overlap in an en echelon pattern and are locally connected by relay ramps that transfer displacement between fault segments that overstep in map view (eg. Fig. 4 at Parmele Ridge) (Peacock, D. C. P. and Sanderson, D. J., 1994).

Well-preserved fault surfaces are rare and were found in only two locations. Slickenlines are preserved in hydrothermally altered and silicified footwalls at Antelope Ridge and Cascade Ridge where exposed fault surfaces strike 270°-288° and dip 66°-71°northeast, and slickenlines pitch 65°NW-90° (Fig. 12). These faults suggest slip has been primarily normal, with up to 28% strike-slip motion at some locations. This conclusion is in general agreement with the observations of (Trench et al., 2012), who used basalt flow margins as a piercing point and concluded negligible strike-slip separation dominates motion of BFZ faults.

A second, smaller population of faults striking N10°E to N40°E are found only in the eastern half of the mapping area and exhibit mutually cross-cutting relationships with

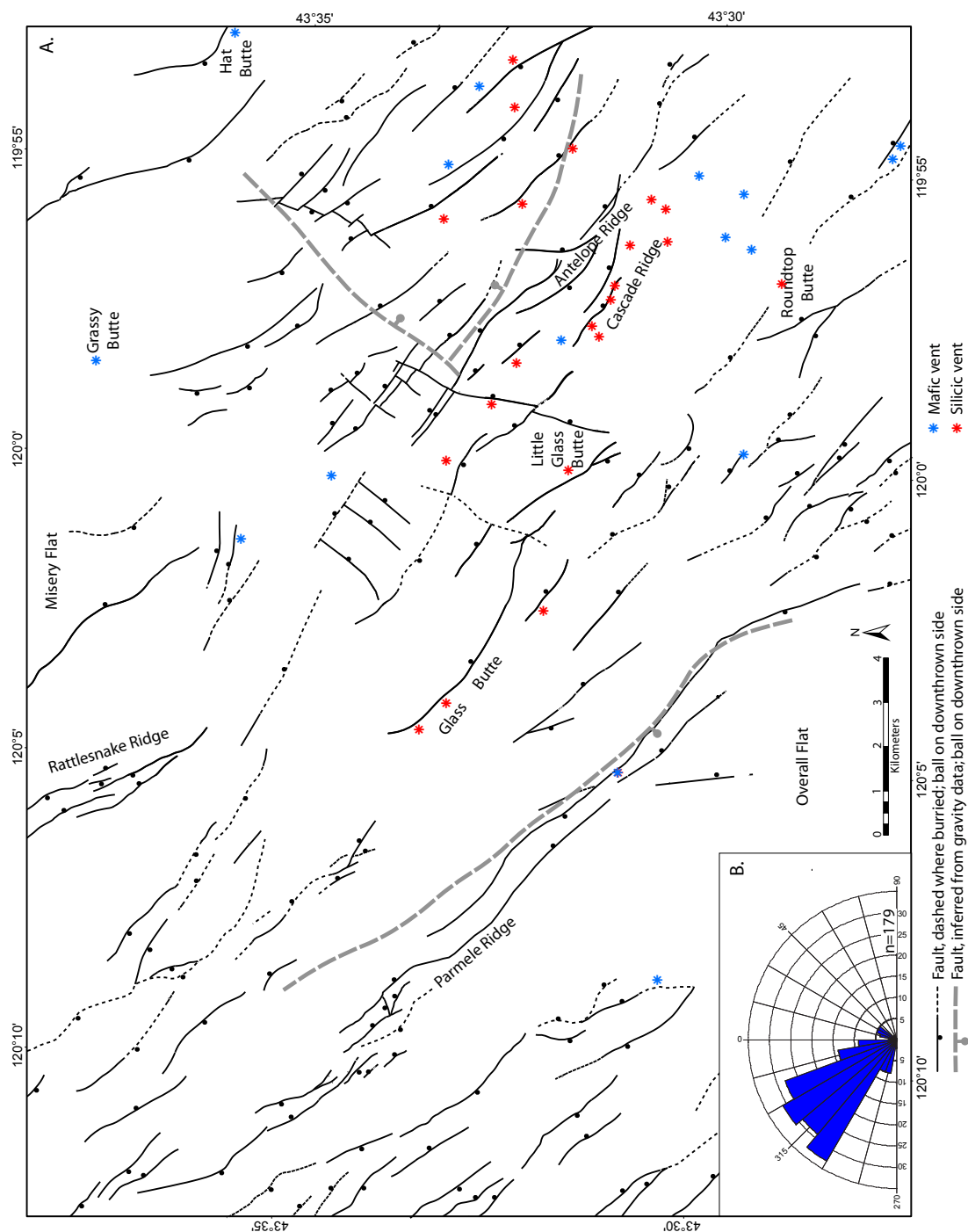


Figure 11: A: Fault map showing the distribution of volcanic vents and faults in the Glass Buttes area. B: Rose diagram illustrating the dominant northeast-striking structural fabric.

the dominant northwest striking fault set (Fig. 11). Individual fault segments in this population are generally 1-5 km in length with normal separation of <40 meters. No preserved slickenlines or piercing points were found along faults of the northeast striking population.

Gravity data (Fig. 13) are consistent with the presence of both northwest- and northeast-striking faults at depth that closely parallel the surface manifestations mapped through LiDAR and field mapping. Figure 13 shows the complete Bouguer gravity anomaly of the survey area using a reduction density of 2.25 g/cc. A prominent, northwest-trending and steep gravity gradient bounds the southwest flank of Glass Butte, for example, and closely parallels the regional BFZ structural fabric, and is located on the area of a mapped down-to-the-southwest normal fault.

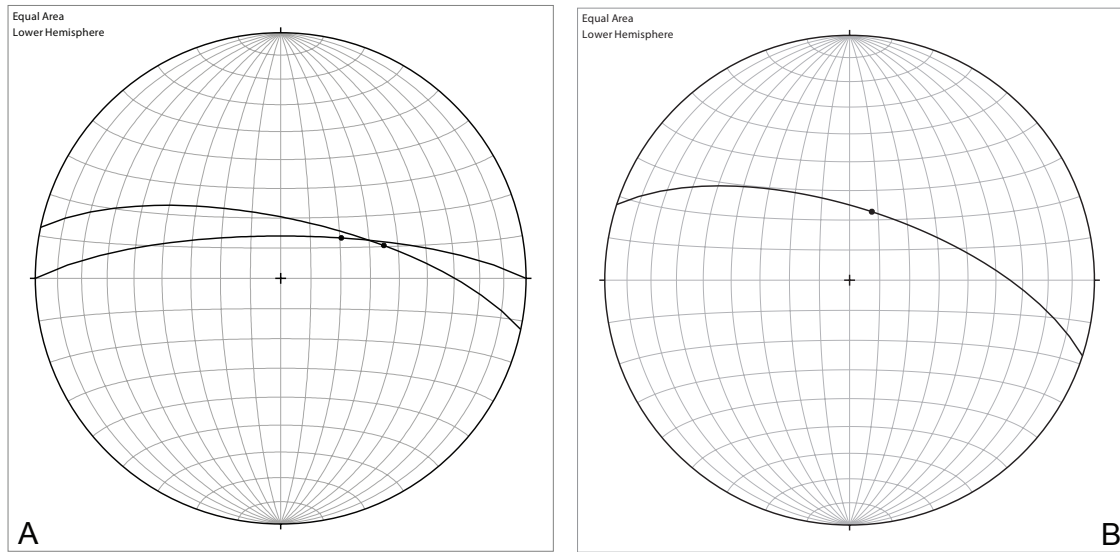


Figure 12: Stereonet projections of slickenlines measured in silicified fault scarps at Cascade Ridge (A) and Antelope Ridge (B). Great circles are fault planes and slickenlines are points on great circles.

A simple 1-D gravity model is used to estimate the offset of the Glass Buttes felsite across this northwest-striking gravity anomaly using the Bouguer formula for an infinite slab and solving for Δh :

$$\Delta h = \frac{\Delta g}{2\pi G \Delta \rho}$$

A gravity change (Δg) of ~ 4 mGal is estimated over the anomaly which is interpreted as a fault juxtaposing the Glass Buttes felsite against unconsolidated sedimentary material deposited on the hanging wall side. The density of unconsolidated alluvium ranges from 1700-2100 kg/m³ and the density of rhyolite (felsite) ranges from 2400-2600 kg/m³ (Daly et al., 1966). Choosing densities of 1700 kg/m³ and 2500 kg/m³ for the unconsolidated alluvium and felsite, respectively, yields a $\Delta \rho$ of 800 kg/m³. Plugging these values of Δg and $\Delta \rho$ into equation 1 yields a vertical offset of 119 m across this fault.

Northeast-trending and northwest-trending gravity anomalies with steep gradients also bound a pronounced gravity low north of Antelope Ridge. These steep gravity gradients are interpreted to mark buried northeast-striking, down to the southeast, and northwest-striking, down to the northeast normal faults (Fig. 11, 13), the combined displacement of which has formed sedimentary basin characterized by low density rocks and a negative Bouguer gravity anomaly. At the northeast edge of this negative anomaly, the top section of Phillips Petroleum Stratigraphic Test Well #2 encountered 46 meters of hydrothermally altered (before transport) rhyolitic gravel and cobbles (Benoit, 1981), which likely represents the shallow margin of the basin. The pronounced gravity high lying north of Glass Butte is interpreted to be the result of a thick sequence of basaltic rocks lying between Grassy Butte and Rattlesnake Ridge and may have been produced

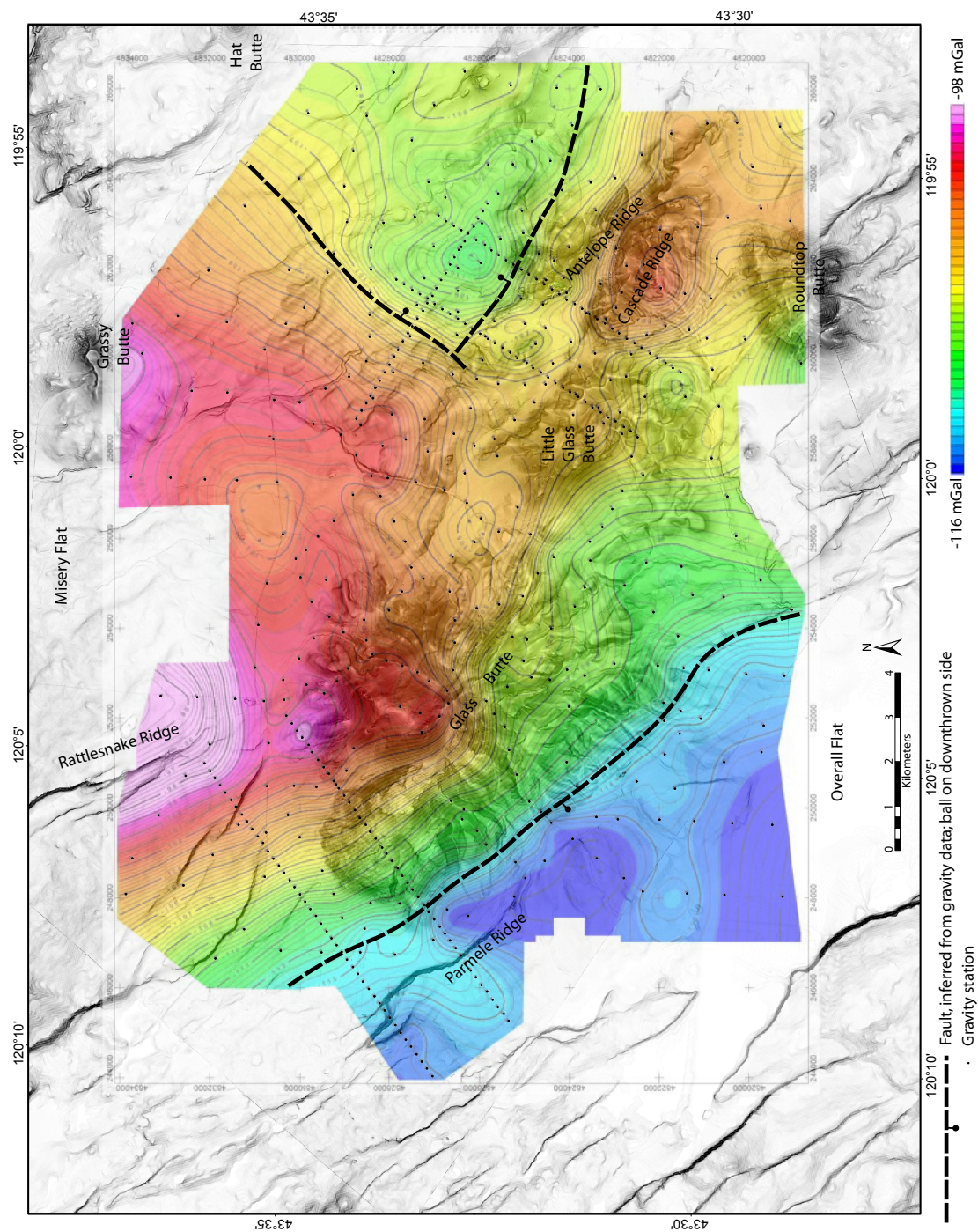


Figure 13: Complete Bouguer gravity anomaly of the eastern complex calculated with a reduction density of 2.25 g/cc. Northeast and northwest trending faults inferred from gravity data are also shown.

where flows have ponded into the half-graben basin north of the map area (Fig. 1). The discontinuous, low displacement, en echelon fault scarps often linked by relay ramps at the surface are interpreted as the surface expression of these much larger and continuous faults inferred from gravity data. Continued slip on these deeper faults has been continuously buried by younger mafic volcanism, thus the small displacement scarps seen at the surface only represent the latest displacement events on these larger structures.

Regional cross sections A-A' and B-B' (Figs. 4, 14) illustrate the general structural style of the Glass Buttes area. Notably, these cross sections highlight the dominant and mapped northwest-striking surface faults as well as basement faults identified in the gravity data.

The thickness of Glass Buttes rhyolites is constrained by drilling records from stratigraphic test wells that intersected up to 610 m of rhyolite (Benoit, 1981; Johnson and Ciancanelli, 1984). The nature of pre-Glass Buttes rocks below this level are inferred to be Middle-Late Miocene basaltic lava flows, sedimentary deposits, and tuffaceous rocks based on studies elsewhere in the High Lava Plains (Jordan et al., 2004; Streck and Grunder, 1995). Similarly, the nature of lithologies underlying the exposed stratigraphic section along the flanks of Glass Buttes is unknown, but is similarly inferred to be intercalated basalt lava flows, sedimentary deposits, and tuffaceous rocks based on regional geology and mapped stratigraphy.

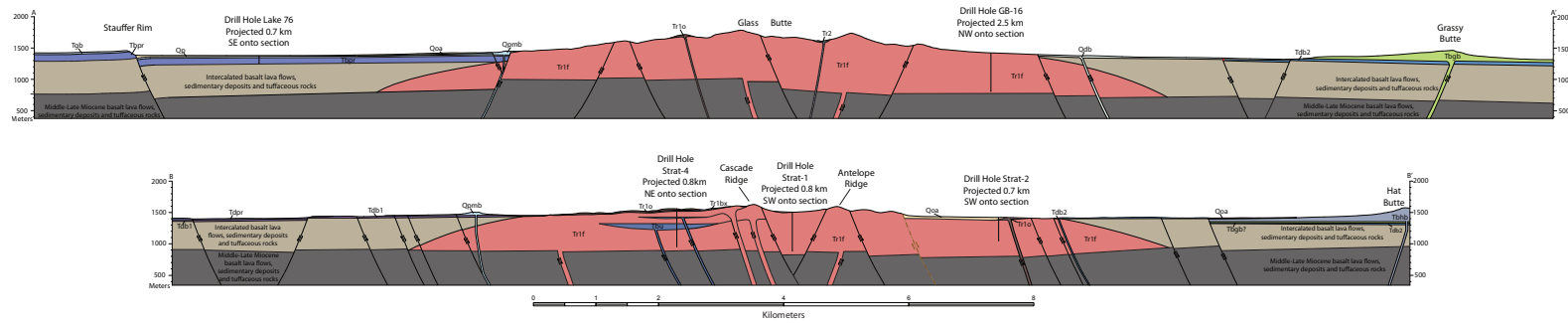


Figure 14: Regional cross-sections A-A' and B-B' (see Figure 4 for cross-section locations). Subsurface lithologies below mapped stratigraphy generalized and inferred from studies elsewhere in the High Lava Plains (Jordan et al., 2004; Streck and Grunder, 1995). No vertical exaggeration.

Timing of deformation

The overall northwest elongation of the oldest silicic rocks dated at Glass Buttes suggests vent emplacement controlled by preexisting, or contemporaneous northwest striking faults of the BFZ at 6.49 ± 0.03 Ma to 5.79 ± 0.02 Ma (Fig. 4). Lava flows of diktytaxitic olivine basalt unit Tdb₂ were erupted from at least two small, structurally aligned vents located ~ 3 km northeast of Antelope Ridge and were channeled northwest along preexisting fault-controlled drainages in the silicic rocks of the Glass Buttes complex (Fig. 4). These fault confined basalt flows indicate that BFZ faults in the Glass Buttes area were unquestionably established by 4.70 ± 0.27 Ma, the oldest age of unit Tdb₂. Continued slip on northwest striking faults into the Quaternary is evidenced by faults that offset and produce scarps with at least 10-15 m of throw in the 1.39 ± 0.18 Ma diktytaxitic olivine basalt unit Qdb. Other scarps are evident in the older alluvial unit (Qoa) unit along the southwest flank of Glass Butte and indicate Pleistocene to Holocene movement (Fig. 4).

Northeast-striking faults are found cutting the Glass Buttes rhyolite complex and the 4.70 ± 0.27 to 4.31 ± 0.29 Ma diktytaxitic olivine basalt unit Tdb₂, but do not cut any of the younger basalt units. Scarps within basalt unit Tdb₂ have topographic separation of 5-15 meters. At one location a northeast-striking fault is buried by flows of the Qdb basalt with an age of 1.39 ± 0.18 Ma, indicating that this northeast trending fault segment has not been recently active.

The northwest-striking, down-to-the-northeast fault bounding the northern flank of Antelope Ridge shows clear evidence of movement post-dating hydrothermal alteration. Abundant silicified fault breccias within rhyolite units on Antelope Ridge and

Cascade Ridge indicate syn- or post-tectonic hydrothermal activity. Northwest along strike the fault segment is overlain by the unaltered 1.39 ± 0.18 Ma Qdb basalt flow, which is in turn cut by the fault, indicating continued post-alteration slip on this fault segment (Fig. 4).

Magnitude and rate of extension

Cross sections 1- 6 (Fig. 15) were constructed to estimate the magnitude of northeast-southwest directed extension and the rate of extension. These relatively short section lines were chosen along continuous exposures of units with well-constrained ages to compare changes in extension magnitude and rate over time across the field area.

Topographic relief, a proxy for the vertical component of slip across fault scarps, geologic mapping, and geometric constraints are used to measure the extension (ΔL) across each fault (Fig. 16). The sum of ΔL divided by the original unextended length (L) is multiplied by 100% to determine percent extension ($\%e_n$) (Twiss and Moores, 2006). Dividing the percent extension value by the age of the faulted surface provides a long-term extension rate for each section over the age of the surface.

$$\%e_n = \frac{\Sigma \Delta L}{L} \times 100\%$$

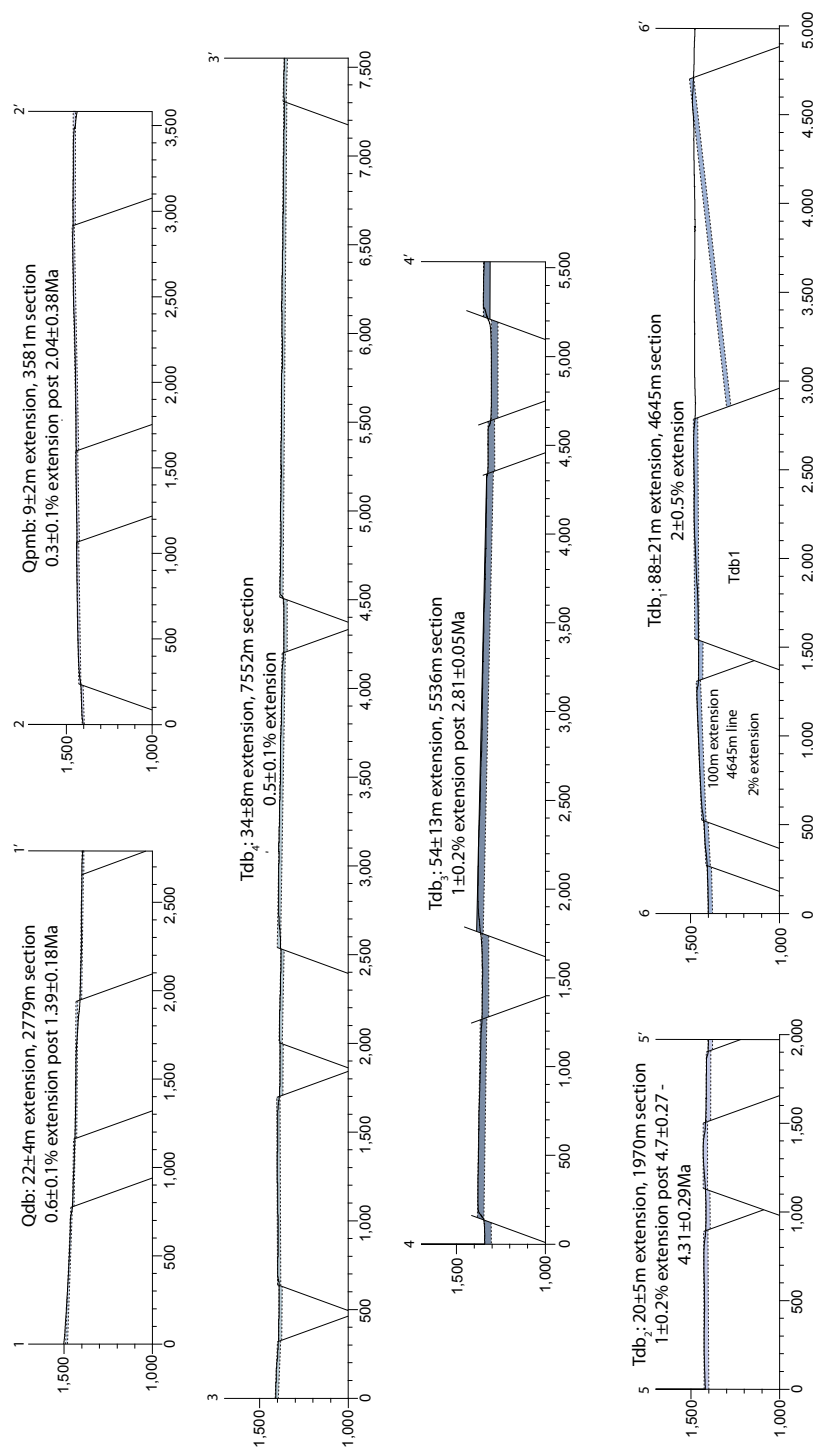


Figure 15: Cross sections from southwest to northeast across surfaces of known or bracketed ages in the study area. See text for discussion.

Based on dip of fault surfaces in the mapping area a 70° dip is assumed for all faults in the cross-sections (Fig. 15). (Jackson and White, 1989) use fault plane solutions of earthquakes to suggest that normal faults on the continents are restricted to a dip range of 30-60°, so although the 70° assumption may underestimate the magnitude of extension, it is used here based on observed fault dips at the surface. Table 5 shows the range of extension magnitude and rate for sections 1 – 6 for fault dips of 65°, 70°, and 75°. These ranges form the basis of an estimate of error for the 70° dip assumption.

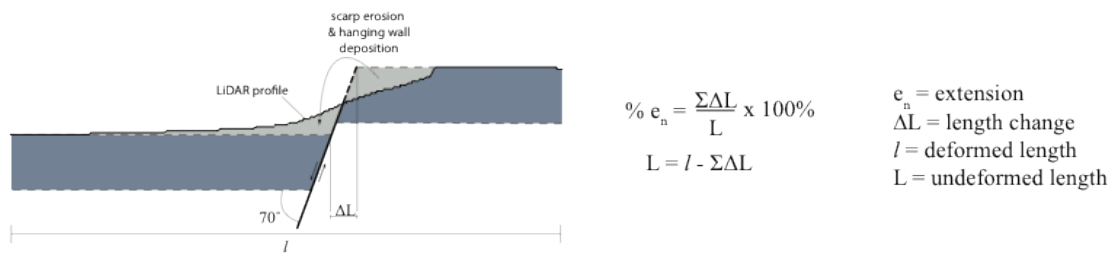


Figure 16: Method for measuring extension across fault scarps utilizing LiDAR topographic profiles. Equation and variable definitions for measuring percent extension also shown.

Table 5: Calculated extension across cross-sections 1-6.

	Unit	Age (Ma)	l	65°				70°				75°			
				$\Sigma \Delta L$ (m)	L (m)	% e_n	mm/yr	$\Sigma \Delta L$ (m)	L (m)	% e_n	mm/yr	$\Sigma \Delta L$ (m)	L (m)	% e_n	mm/yr
A-A'	Qdb	1.39±0.18	2779	21	2758	0.8	0.015	17	2762	0.6	0.012	13	2766	0.5	0.009
B-B'	Qpmb	2.04±0.38	3581	11	3570	0.3	0.005	9	3572	0.3	0.004	6	3575	0.2	0.003
C-C'	Tdb ₄	2.81±0.05-2.04±0.38	7552	42	7510	0.6	0.015-0.02	34	7518	0.5	0.01-0.02	26	7526	0.3	0.013-0.009
D-D'	Tdb ₃	2.81±0.05	5536	68	5468	1.2	0.024	55	5481	1.0	0.020	41	5495	0.7	0.015
E-E'	Tdb ₂	4.70±0.27-4.31±0.29	1970	25	1945	1.3	0.005-0.006	20	1950	1.0	0.004-0.005	15	1955	0.8	0.003
F-F'	Tdb ₁	4.70±0.27-6.49±0.03	4645	109	4536	2.4	0.017-0.023	88	4557	1.9	0.01-0.02	66	4579	1.4	0.01-0.014

The 1-1' cross section traverses the 1.39 ± 0.18 Ma Qdb basalt unit northwest of Antelope Ridge and crosses 2-25 meter high northwest-striking fault scarps (Figs. 4, 15). Horizontal extension on individual faults ranges from 0.7 to 8.6 m for a total of 17 ± 4 m extension across the 2779 m long 1-1' cross section. A total of 0.6% extension over cross section 1-1' yields a long-term extension rate of 0.012 mm/yr (Table 5).

The 2-2' cross section traverses the Qpmb basalt unit and crosses 2-11 meter high northwest-striking fault scarps (Figs. 4, 15). Horizontal extension on individual faults ranges from 0.6 to 3.8 m for a total of 9 ± 2 m extension across the 3581 m long 2-2' cross section. A total of 0.3% extension over cross section 2-2' yields a long-term extension rate of 0.004 mm/yr (Table 5).

The 3-3' cross section traverses the 2.04 ± 0.38 Ma Tdb4 basalt unit and crosses 3-26 meter high northwest-striking fault scarps (Figs. 4, 15). Horizontal extension on individual faults ranges from 1 to 8.9 m for a total of 34 ± 8 m extension across the 7552 m long 3-3' cross section. A total of 0.5% extension over cross section 3-3' yields a long-term extension rate of 0.01 – 0.02 mm/yr (Table 5).

The 4-4' cross section traverses the 2.81 ± 0.05 Ma Tdb3 basalt unit and crosses 7-48 meter high northwest-striking fault scarps (Figs. 4, 15). Horizontal extension on individual faults ranges from 2.4 to 16.4 m for a total of 55 ± 14 m extension across the 5536 m long 4-4' cross section. A total of 1.0% extension over cross section 4-4' yields a long-term extension rate of 0.02 mm/yr (Table 5).

The 5-5' cross section traverses the 4.70 ± 0.27 Ma Tdb2 basalt unit and crosses 11-19 meter high northwest-striking fault scarps (Figs. 4, 15). Horizontal extension on individual faults ranges from 3.8 to 6.5 m for a total of 20 ± 5 m extension across the 1970

m long 5-5' cross section. A total of 1.0% extension over cross section 5-5' yields a long-term extension rate of 0.004 – 0.005 mm/yr (Table 5).

The 6-6' cross section traverses the Tdb1 basalt unit and crosses 8-200 meter high (inferred from measured fault block dip) northwest-striking fault scarps (Figs. 4, 15). Horizontal extension on individual faults ranges from 2.7 to 68.4 m for a total of 88 ± 22 m extension across the 4645 m long 6-6' cross section. A total of 1.9% extension measured over cross section 6-6' yields a long term extension rate of 0.01 – 0.02 mm/yr (Table 5).

Horizontal extension across individual faults ranges from 0.6 m to 68.4 m with total extension ranging from 17 – 88 m across sections 1970 – 7552 m long. Percent extension ranges from 0.3% across the 2.04 ± 0.38 Ma Qpmb unit (B-B') to 1.9% across the 4.7 ± 0.27 - 6.49 ± 0.03 Ma Tdb1 unit (6-6'), the oldest mafic unit in the field area. Long-term extension rates across northwest-striking faults calculated from cross section restorations range from 0.004 – 0.02 mm/yr with an average of 0.012 mm/yr (Table 5). Variations in calculated extension rates across the field area are likely explained by strain heterogeneities due to the relative location of active basement faults to cross section lines, although variations in extension rate through time are likely (see discussion below).

DISCUSSION

Stratigraphic and cross-cutting relationships between faults, basaltic rocks, silicic rocks, and regions of hydrothermal alteration, combined with $^{40}\text{Ar}/^{39}\text{Ar}$ ages provide constraints on the timing and association between faulting, silicic volcanism, basaltic volcanism and hydrothermal alteration in and around the Glass Buttes complex.

Tectonomagmatic summary of the Glass Buttes area

The northwest alignment of silicic eruptive centers of the Glass Buttes complex suggests vent emplacement controlled by preexisting, or contemporaneous northwest striking faults of the Brothers Fault Zone (BFZ) by 6.49 ± 0.03 Ma, the age of the oldest rhyolitic rocks at Glass Buttes. A more definitive constraint on the earliest presence of BFZ faults in the Glass Buttes area is the flow paths of basalt unit Tdb₂, which are localized along, and bank against fault-controlled paleo-valleys in the underlying silicic rocks. This relationship unambiguously establishes the presence of a northwest-striking BFZ structural fabric by 4.70 ± 0.27 Ma, the oldest age of unit Tdb₂.

The average long term extension rate from cross-section restorations (0.012 mm/yr) is consistent with previous calculations by (Trench et al., 2012) who calculated a post-5.68 Ma extension rate of 0.01 mm/yr regionally across the BFZ. Two time periods, $2.04 \pm 0.38 - 1.39 \pm 0.18$ Ma (cross section 2-2'), and $4.70 \pm 0.27 - 2.81 \pm 0.05$ Ma (cross section 5-5') record extension rates an order of magnitude lower than the rates calculated across all other cross sections (Fig. 15; Table 5). The variation in extension rate can be satisfied by two possible explanations: (1) the distribution of strain at the surface is not homogenous within the map area; (2) the rate of extension has not been constant

between 6.49 ± 0.03 – 1.30 ± 0.18 Ma. It is clear from Figure 11 that there is heterogeneity in the distribution of faults at the surface, and that the location of a given cross-section line will have an effect on the total calculated extension. However, a comparison of cross-sections 2-2' and 6-6' supports the explanation that extension has been variable through time. Both cross sections are located in the same region of the map area, are roughly aligned along strike of the northwest structural fabric, and are located at about the same distance from the deep-seated basement fault bounding the southwest flank of Glass Butte. Given these considerations, the data support the interpretation that the rate of extension at this location slowed from 0.01-0.02 mm/y to 0.004 mm/yr sometime after 2.04 ± 0.38 Ma. Other variations in extension rate between cross sections 1-6 are not easily compared due to the possibility of strain heterogeneity across the map area.

Basaltic volcanism persisted in the Glass Buttes area from early eruption synchronous with the rhyolite domes until the Quaternary. Interlayered basaltic and rhyolitic flows in Phillips stratigraphic test well #4 demonstrate that basaltic volcanism accompanied the initial rhyolitic eruptive episode. The youngest dated basalt flow is the 1.39 ± 0.18 Ma diktytaxitic olivine basalt unit Qdb, and no stratigraphically younger basalt was mapped in the field area (Fig. 7).

Vents of basalt units Tdb₂ and Qdb are aligned along northwest striking BFZ faults both within and along the northern flanks of the Glass Buttes complex. It is presumed that vents are connected at depth by dikes, the emplacement of which was controlled by normal faults of the BFZ. Elsewhere, vents of units Tgb, Qpmb, Tbh_b, and Tbu are localized along northwest-striking faults.

Flows of unit Qdb erupted from a small vent located between Cascade Ridge and Antelope Ridge flowed over and buried hydrothermally altered and mineralized zones along the Antelope Ridge fault system. Subsequent reactivation of this structure has since faulted these flows since Tdb₂ time. Four kilometers to the northeast, a vent of unit Tdb₂ erupted along this same system of faults, burying these faults with no subsequent reactivation. Although the duration between eruptions of these two Tdb₂ vents is not constrained, these relations suggest fault motion and vent eruption may have occurred in close succession, and so suggest a close association between active faulting and volcanism.

The termination of northeast-striking faulting between 4.70 ± 0.27 Ma and 1.39 ± 0.18 Ma is a conspicuous element of the structural history at Glass Buttes. Prior to this time, northwest- and northeast-striking faults exhibit mutually cross-cutting relationships. The structural fabric then changed to one exclusively characterized by northwest-striking BFZ faults some time after 4.70 ± 0.27 Ma. This observation is in contrast to the findings of (Scarberry et al., 2010), who report mutually cross cutting northwest- and northeast-striking faults giving way to a dominantly northeast-striking structural fabric at the northern end of the Abert Rim fault in the Northwest Basin and Range 80 km to the south.

The BFZ clearly marks the topographic boundary between the Blue Mountains – Ochoco Mountains uplift to the north and the relatively flat-lying topography of the High Lava Plains and Northwest Basin and Range. The Riedel shear model of Lawrence (1976) for the northwest- and northeast- striking faulting seen throughout the BFZ been difficult to defend due to a lack of observable strike-slip offset, or kinematic indicators

suggesting strike-slip motion on BFZ faults. Further, (Trench et al., 2012) concluded using regional cross section restorations that the BFZ and NWBR are kinematically unrelated and display an additive effect of extension where the two zones overlap. However, as illustrated in the detailed mapping of basaltic stratigraphy at Glass Buttes, estimation of extension from cross sections is complicated by continual burial of older surfaces by progressively younger basaltic flows, essentially masking the magnitude of extension for previous periods.

I propose a model going back to the Riedel shear model of Lawrence (1976) in which the contemporaneous northeast and northwest-striking faults in the BFZ are the surface expression of deep seated shearing in response to NWBR extension against the relatively less extended Blue Mountains province to the north. Importantly however, the observations at Glass Buttes illustrate that the simultaneous northwest- and northeast-striking faulting gives way to exclusively northwest-striking faulting some time after 4.7 ± 0.27 Ma. My interpretation of this relationship, in the context of the model of Lawrence (1976) is that after 4.7 ± 0.27 Ma Riedel shearing ceases in response to some kinematic mechanism that relaxes the horizontal maximum principal stress, resulting in the active northwest-striking faults we see today. One possible mechanism for the relaxing of the horizontal maximum principal stress is the northwestward propagation of the northern Walker Lane dextral shear zone toward the Cascade arc by about ~ 3.5 Ma (Faulds and Henry, 2008) (Fig. 19). If displacement along faults in the BFZ has been purely normal to slightly oblique since ~ 3.5 Ma, and given the continual burial of older surfaces by younger basaltic flows, as well as the general tendency for these basaltic fault scarps to degrade and not preserve slickenlines, it would be entirely possible that all

kinematic indications of strike-slip shear have been obscured except for the relict polygonal faults resulting from prior Riedel shearing type deformation.

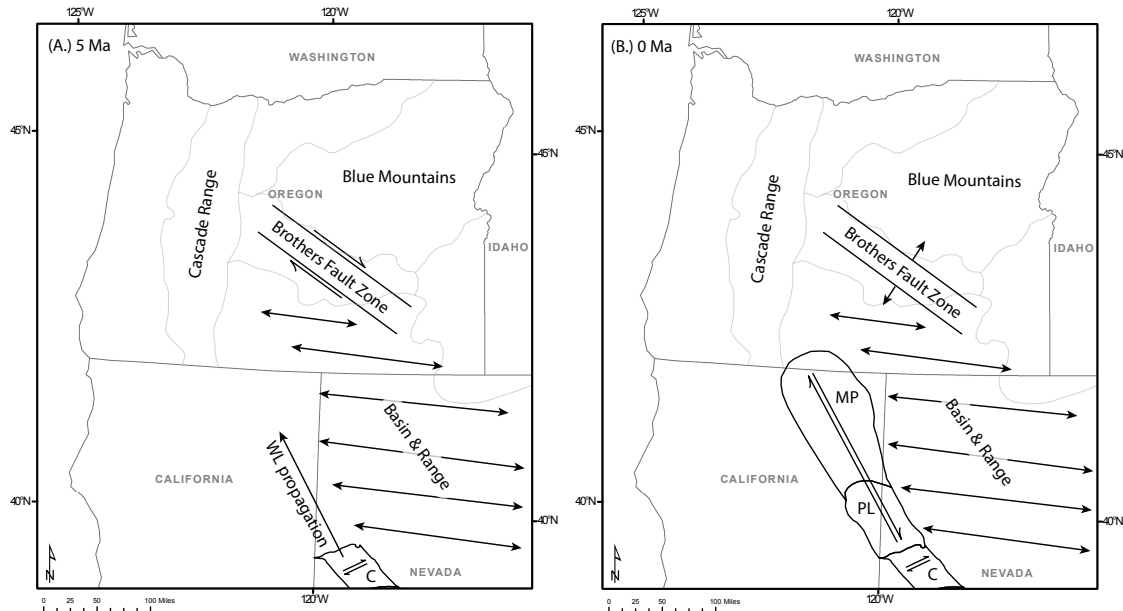


Figure 17: Regional tectonic model for the Brothers Fault Zone in the context of Basin and Range Extension and northward propagation of the Walker Lane dextral shear zone. **A.** At ~5 Ma the BFZ is deforming as a Riedel shear zone in response to differential extension between the Basin and Range and Blue Mountains provinces. Deformation at the propagating front of the Walker Lane belt is active in the Carson domain (C) as east-to northeast-striking dextral shear beginning ~9 to 5 Ma. **B.** At present the BFZ is extending in a NE-SW direction in response to the northward propagation of dextral shear in the Pyramid Lake (PL) and Modoc Plateau (MP) domains of the Walker Lane Belt, both of which became active at ~3.5 Ma (Faulds and Henry, 2008).

Geothermal activity

Airborne spectral mineral mapping by HyVista identified the presence of goethite, opal, dickite, alunite, kaolinite, tourmaline and sericite (Fig. 17). Two endmembers of dickite were identified, which may be due to temperature of formation and/or mixing

with kaolinite. Four endmembers of opal were identified, and it is likely that much of the detected opaline signature in the western complex is in fact mapping the abundant obsidian flows in the area (Martini, 2010).

Hydrothermal opal (silicification) is the dominant alteration type, within irregular zones of rhyolite altered to mixtures of fine-grained kaolinite, alunite and opal and localized cinnabar mineralization (Berri, 1982; Hussey, 2010; Johnson, 1984; Martini, 2010). The opal-kaolinite-alunite alteration and cinnabar mineralization is here interpreted to result from near-surface steam-heated advanced argillic alteration characteristic of the uppermost and $<100^{\circ}\text{C}$ parts of epithermal/geothermal fluids (Simeone et al., 2005; Simmons et al., 2005). Mercury associated with steam is well documented for the Steamboat Springs Nevada and Clear Lake California - Sulphur Bank deposits (White et al., 1970).

Field mapping confirms that pervasive hydrothermal alteration of silicic rocks is localized along faults bounding Cascade Ridge and Antelope Ridge, with zones of

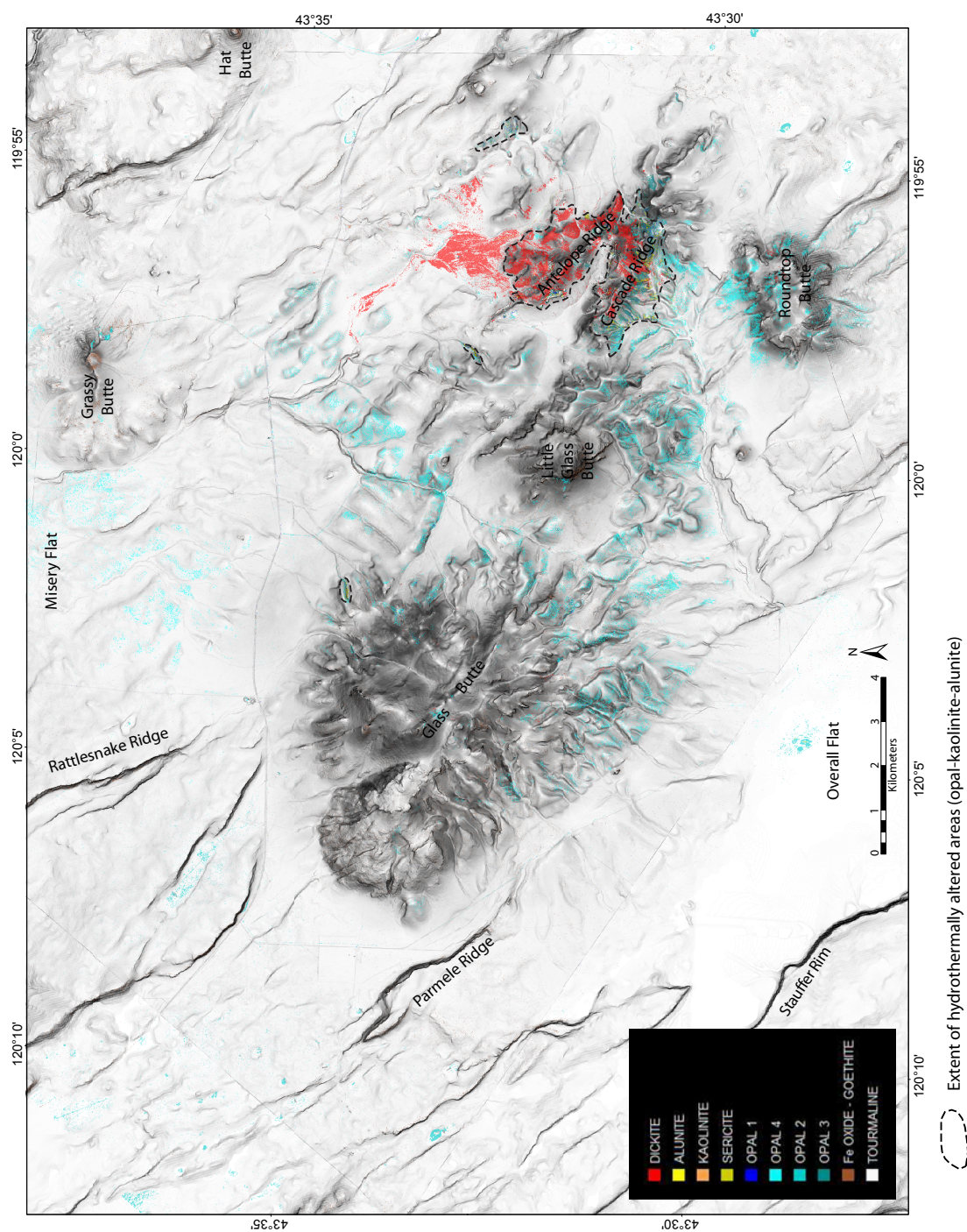


Figure 18: Hyperspectral mineral map color composite showing extent of opal-kaolinite-alunite alteration.

of opal-kaolinite-alunite alteration as determined via PIMA SWIR spectral data collected on a dozen samples at Cascade Ridge and Antelope Ridge. Results of the PIMA analysis did not identify the presence of sericite or tourmaline, and dickite was only identified in one sample, in contrast to the widely distributed dickite identified by the airborne survey. The termination of hydrothermal alteration and associated cinnabar mineralization along Antelope Ridge, Cascade Ridge and silicic rocks to the east is also constrained to predate the 4.70 ± 0.27 to 4.31 ± 0.29 Ma basalt unit Tdb₂. Field mapping supported by airborne hyperspectral mineral mapping demonstrates that unaltered unit Tdb₂ overlies hydrothermally altered silicic rocks ~3 kilometers northeast of Antelope Ridge. Accordingly, the working hypothesis is that hydrothermal alteration is likely related to the emplacement and eruption of the silicic volcanic centers at the eastern end of the complex, dated at 6.49 ± 0.03 Ma.

Figure 18 shows an inverse distance weighted interpolation plot of temperature gradient from 20 geothermal exploration wells in the Glass Buttes area (Johnson and Ciancanelli, 1984; Sass et al., 2000). One well to the east is not shown. Only wells deeper than 90 meters were used in the interpolation. The distribution of high temperature zones in Figure 18 suggests that the shallow thermal anomaly is localized along several zones, one to the north of Antelope Ridge, and another lying southwest of Glass Butte near Parmele Ridge (Fig. 4).

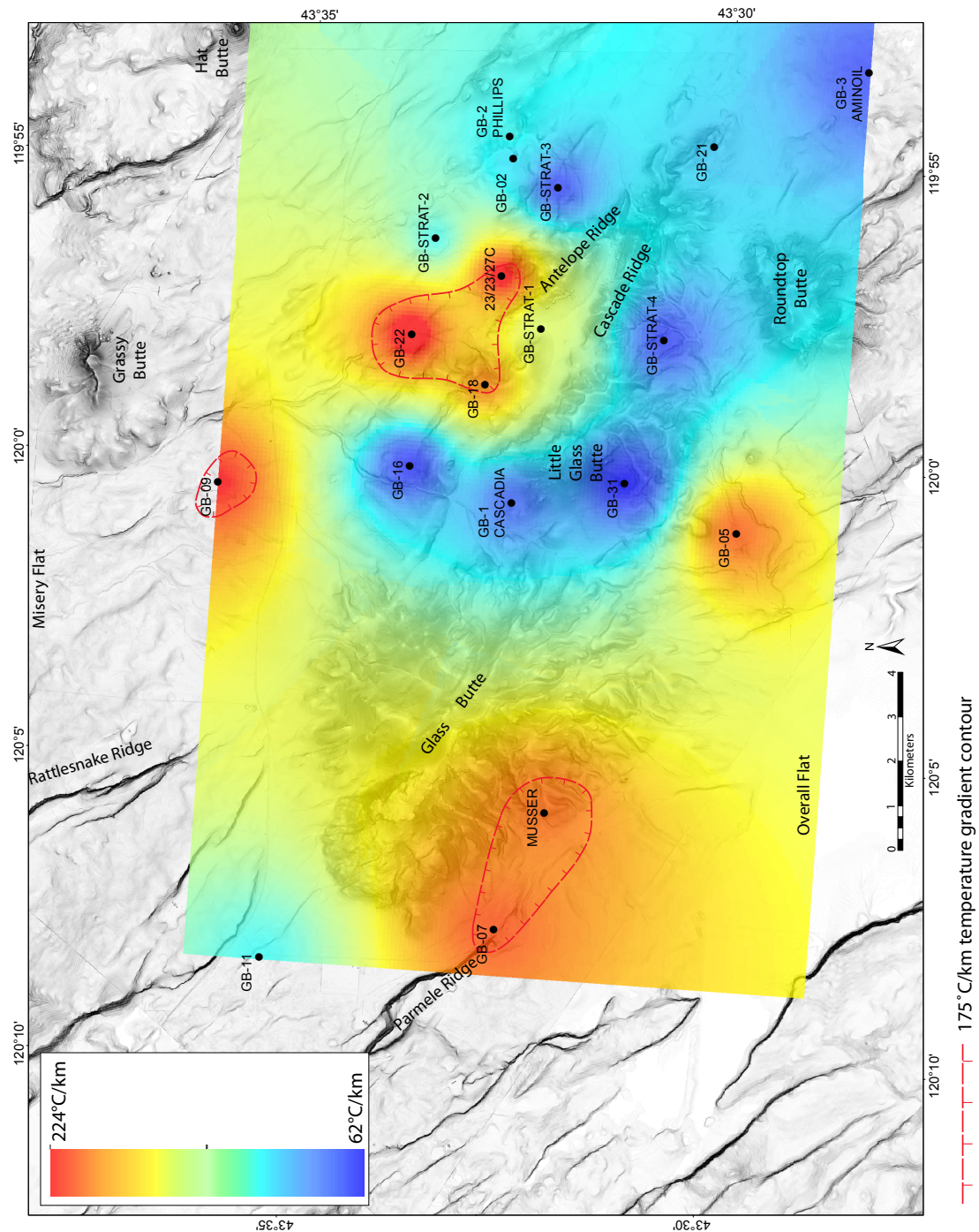


Figure 19: Inverse distance weighted interpolation plot of temperature gradient from 20 geothermal exploration wells in the Glass Buttes area (one well to the east not shown). Only wells deeper than 90 meters were used in the interpolation. Regions of temperature gradient $>175^{\circ}\text{C}/\text{km}$ are encircled in red.

Figure 4 illustrates the association of the modern geothermal anomaly, intersecting northwest- and north-northeast-striking fault scarps, and deeper faults inferred from gravity data and strongly suggests that geothermal upflow at Glass Buttes is controlled by faults in the area, particularly areas where northwest- and northeast-striking faults intersect, and along the large active normal fault bounding the southwest margin of Glass Butte (Fig. 13).

Temperatures in the range of 85 to 170°C are sufficient to operate a modern binary geothermal power plant with the selection of an appropriate working fluid (Maghiar and Antal, 2001). Given the average High Lava Plains geothermal gradient of 82.2°C/km (Blackwell et al., 1982) the lowest end of this feasible temperature range could be reached at about 1 kilometer depth. Furthermore, the maximum extrapolated geothermal gradient from Glass Buttes of 224°C/km (Benoit, 1981) would suggest that economic temperatures could be reached at much shallower depths.

In the western United States two general types of geothermal systems have been described. *Magma heated systems* are those geothermal systems closely associated with young (≤ 1.5 Ma) silicic volcanic rocks (Koenig and McNitt, 1983), whereas *extensional-type* systems rely on deep circulation of water along faults to achieve elevated temperatures, and are not associated with a young nearby magma body (Wisian et al., 1999).

Furthermore, numerical calculations of the longevity of geothermal systems (e.g. (Cathles et al., 1997) suggest that convective magmatic systems which produce near surface geothermal systems, such as the one that produced the hydrothermal alteration at Glass Buttes, will typically cool and cease surface activity in at most ~800,000 years.

Geologic evidence suggests that even with multiple episodes of magmatism, the longest-lived geothermal systems are active only ~1 m.y. (Cathles et al., 1997).

This modeling result suggests that the modern geothermal anomaly measured in temperature gradient wells is not directly related to the geothermal system that created surface alteration before 4.70 ± 0.27 Ma or the emplacement of rhyolite lavas that were likely the source of this earlier system. Rather, the interpretation is that the modern geothermal anomaly most likely can be categorized as an extensional type system analogous to those found in the Great Basin. Alternatively, the presense of basalt lavas as young as 1.4 Ma at Glass Buttes is compatible with the possibility that younger basaltic intrusions at depth may be providing some magmatic heat. The two geothermal systems are related in the sense that the emplacement of rhyolites that created the surface alteration was controlled by northwest-striking faults, much as the upflow of the current geothermal system is controlled by faults today. Given the association of the modern thermal anomaly with the largest of the gravity anomalies inferred to represent large normal faults, the interpretation is that hydrothermal circulation is localized along deep basement faults cutting through the Glass Buttes area.

CONCLUSIONS

Basaltic eruptions in the Glass Buttes area from numerous small mafic vents continued from $>6.49\pm0.03$ Ma to 1.39 ± 0.18 Ma. Previous mapping (e.g. (Roche, 1987) identified only two distinct basaltic units in the area, but new whole-rock geochemistry verifies these lava flows are far more diverse in composition and timing than previously thought. Whole rock geochemistry by both conventional and portable XRF analysis readily distinguished the diversity in basalt composition, identifying 10 new basalt-basaltic andesite units within the map area. The ability to distinguish these basalts, and to establish the mafic stratigraphy plays a fundamental role in understanding both the structural and volcanic history of the Glass Buttes area, and the application of detailed mapping and a dense sampling strategy would likely shed light on remaining questions across the HLP and elsewhere.

Small displacement, discontinuous, en echelon, northwest-striking fault scarps locally linked by relay ramps dominate the structural fabric of the Glass Buttes area. Northwest vent alignment, paleotopography, and cross cutting relationships suggest these structures have been active since at least 6.49 ± 0.03 Ma, the age of the rhyolites in the eastern part of the Glass Buttes complex. Identification of subtle, low relief fault scarps in surficial deposits and Quaternary age basalts by means of LiDAR analysis confirm that northwest-striking faults continue to be active into the Quaternary. A subordinate population of discontinuous northeast-striking fault scarps exhibits mutually cross cutting relationships with the dominant northwest-striking population. Cross-cutting relationships indicate northeast faulting ceased sometime between 4.70 ± 0.27 Ma and

1.39±0.18 Ma. After this time the structural fabric changes to one dominated exclusively by northwest-striking faults.

Gravity data at Glass Buttes reveals prominent northwest- and northeast-trending gravity gradients that closely parallel the strikes of mapped faults at the surface. These are interpreted as large, deep-seated normal faults that express themselves in the young basalts at the surface as the discontinuous, en echelon fault segments. These inferred and apparently long-lived basement faults are the dominant structures, and seemingly control the structural fabric of the area. The large, northwest-striking gravity gradient along the southwest flank of Glass Butte in particular represents the most significant structure in the map area. The total magnitude of displacement and slip history along this structure cannot be resolved here due to continual resurfacing and burial of older deformational episodes by progressively younger mafic lava flows. Further gravity modeling informed by the updated stratigraphy presented here may be able to resolve more details about these deeper structures.

Long-term extension rates across northwest-striking faults calculated from cross section restorations range from 0.004 – 0.02 mm/yr with an average of 0.12 mm/yr, consistent with the findings of (Trench et al., 2012). These values are calculated using a constant fault dip of 70°, and may underestimate the magnitude of extension if fault dips become shallower at depth. Variations in extension rate through time are evident from comparisons of cross-sections over surfaces of different ages, however these comparisons are complicated by likely heterogeneities in strain over the surface of the map area. Targeted mapping of basaltic stratigraphy elsewhere in the BFZ could likely explore this variation in more detail.

Near-surface steam-heated hydrothermal alteration predates basalt unit Tdb2 (4.70 ± 0.27 - 4.31 ± 0.29 Ma), and is likely associated with rhyolite eruption in the eastern complex. Elevated geothermal gradients are localized along deep-seated, gravity defined structures in two locations: (1) where northwest- and northeast-striking faults intersect, (2) along the very prominent northwest-striking active normal fault bounding the southwest flank of Glass Butte. The modern thermal anomaly is not directly related to the hydrothermal system that created surface alteration before 4.70 ± 0.27 Ma, rather, our interpretation is that the modern thermal anomaly is related to deep circulation along faults similar to convective systems of the Great Basin.

REFERENCES

- Benoit, W.R., 1981, The Results of Intermediate Depth Drilling at the Glass Buttes Prospect, Lake County, Oregon, Phillips Petroleum Company, Geothermal Division.
- Berri, D.A., 1982, Geology and Hydrothermal Alteration, Glass Buttes, Southeast Oregon: Portland, Portland State University.
- Blackwell, D., Bowen, R.G., Hull, D.A., Riccio, J., and Steele, J.L., 1982, Heat Flow, Arc Volcanism, and Subduction in Northern Oregon: *Journal of Geophysical Research*, v. 87, p. 19.
- Cathles, L.M., Erendi, A., and Barrie, T., 1997, How long can a hydrothermal system be sustained by a single intrusive event?: *Economic Geology*, v. 92, p. 766-771.
- Ciancanelli, E.V., Emmet, P.A., 1979, Geology of the Glas Butte geothermal prospect, Lake County, Oregon: A report prepared for the Vulcan Group., p. 56.
- Conrey, R., Wolff, J.A., Seyfarth, A., VanHoose, A., Goodman-Elgar, M., Bettencourt, N., Boschmann, D., and Werling, K., 2012, Portable XRF calibration using influence coefficients, 8th International Conference on the Analysis of Geological and Environmental Materials: Buzios, Rio de Janeiro, Brazil.
- Daly, R., Manger, G., and Clark, S., 1966, Density of rocks: *Handbook of physical constants: Geological Society of America Memoir*, v. 97, p. 19-26.
- Donath, F.A., 1962, Analysis of Basin-Range structure, south-central Oregon: *Geological Society of America Bulletin*, v. 73, p. 1-16.
- Faulds, J.E., and Henry, C.D., 2008, Tectonic influences on the spatial and temporal evolution of the Walker Lane: An incipient transform fault along the evolving Pacific-North American plate boundary: Ores and orogenesis: Circum-Pacific tectonics, geologic evolution, and ore deposits: *Arizona Geological Society Digest*, v. 22, p. 437-470.
- Ford, M.T., 2011, Rhyolitic magmatism of the High Lava Plains and adjacent Northwest Basin and Range, Oregon : implications for the evolution of continental crust [PhD thesis]: Corvallis, Oregon State University.
- Hussey, M.C., 2010, HyMap Survey Processing Report - Glass Buttes Oregon: Reno, NV, Unpublished industry report - Hyvista Corporation, p. 24.
- Iademarco, M., 2009, Volcanism and Faulting along the Northern Margin of Oregon's High Lava Plains: Hampton Butte to Dry Mountain [MS thesis]: Corvallis, Oregon State University.
- Jackson, J., and White, N., 1989, Normal faulting in the upper continental crust: observations from regions of active extension: *Journal of Structural Geology*, v. 11, p. 15-36.
- Johnson, D., Hooper, P., and Conrey, R., 1999, XRF analysis of rocks and minerals for major and trace elements on a single low dilution Li-tetraborate fused bead: *Advances in X-ray Analysis*, v. 41, p. 843-867.
- Johnson, J.A., 1995, Geologic evolution of the Duck Creek Butte eruptive center, High Lava Plains, southeastern Oregon: Corvallis, Oregon State University.
- Johnson, K.E., and Ciancanelli, E.V., 1984, Geothermal Exploration at Glass Buttes, Oregon: *Oregon Geology*, v. 46, p. 15-19.

- Johnson, M.J., 1984, Geology, Alteration, and Mineralization of a Silicic Volcanic Center, Glass Buttes, Oregon: Portland, Portland State University.
- Jordan, B.T., Grunder, A.L., Duncan, R.A., and Deino, A.L., 2004, Geochronology of age-progressive volcanism of the Oregon High Lava Plains: Implications for the plume interpretation of Yellowstone.
- Koenig, J., and McNitt, J., 1983, Controls on the location and intensity of magmatic and non-magmatic geothermal systems in the Basin and Range province: Geothermal Resources Council, Special Report.
- Koppers, A.A.P., 2002, ArArCALC--software for $^{40}\text{Ar}/^{39}\text{Ar}$ age calculations: Computers & Geosciences, v. 28, p. 605-619.
- Langer, V., 1991, Geology and petrologic evolution of silicic and intermediate volcanic rocks underneath Steens Mountain basalt: SE Oregon: Queen's University (CAN) MS thesis.
- Lawrence, R.D., 1976, Strike-Slip Faulting Terminates Basin and Range Province in Oregon: Geological Society of America Bulletin, v. 87, p. 846-850.
- Longo, A.A., Dilles, J.H., Grunder, A.L., and Duncan, R., 2010, Evolution of calc-alkaline volcanism and associated hydrothermal gold deposits at Yanacocha, Peru: Economic Geology, v. 105, p. 1191-1241.
- Maghiar, T., and Antal, C., 2001, Power generation from low-enthalpy geothermal resources: Geo-Heat Center Quarterly Bulletin, v. 22, p. 35-38.
- Martini, B., 2010, Hyperspectral Data Analysis and Synthesis - Glass Buttes Oregon, Unpublished industry report - Ormat Technologies Inc., p. 4.
- McCaffrey, R., Qamar, A.I., King, R.W., Wells, R., Khazaradze, G., Williams, C.A., Stevens, C.W., Vollick, J.J., and Zwick, P.C., 2007, Fault locking, block rotation and crustal deformation in the Pacific Northwest: Geophysical Journal International, v. 169, p. 1315-1340.
- McKee, E.H., MacLeod, N.S., and Walker, G.W., 1976, Potassium-argon ages of late Cenozoic silicic volcanic rocks, southeast Oregon: Isochron, West.
- Millard, J.B., 2010, Two-stage opening of the northwestern basin and range in eastern Oregon: Evidence from the Miocene Crane Basin [Master's thesis]: Corvallis, Oregon State University.
- Minor, S.A., Plouff, D., Esparanza, L.E., and Peters, T.J., 1987, Mineral Resources of the High Steens and Little Blitzen Gorge Wilderness Study Areas, Harney County, Oregon, *in* Bulletin, U.S.G.S., ed., Volume 8755-531X, US Government Printing Office, p. A1-A21.
- Pezzopane, S.K., and Weldon, R.J., 1993, Tectonic Role of Active Faulting in Central Oregon: Tectonics, v. 12, p. 1140-1169.
- Roche, R.L., 1987, Stratigraphic and Geochemical Evolution of the Glass Buttes Complex, Oregon: Portland Portland State University.
- Sass, J.H., Priest, S.S., Blanton, A.J., Sacket, P., Welch, S.L., and MA, W., 2000, Geothermal industry temperature profiles from the Great Basin: US Geological Survey Open-file Report, p. 99-425.
- Scarberry, K.C., Meigs, A.J., and Grunder, A.L., 2010, Faulting in a propagating continental rift: Insight from the late Miocene structural development of the Abert Rim fault, southern Oregon, USA: Tectonophysics, v. 488, p. 71-86.

- Simeone, R., Dilles, J., Padalino, G., and Palomba, M., 2005, Mineralogical and stable isotope studies of kaolin deposits: Shallow epithermal systems of western Sardinia, Italy: *Economic Geology*, v. 100, p. 115-130.
- Simmons, S.F., White, N.C., and John, D.A., 2005, Geological characteristics of epithermal precious and base metal deposits.
- Streck, M.J., and Grunder, A.L., 1995, Crystallization and welding variations in a widespread ignimbrite sheet; the Rattlesnake Tuff, eastern Oregon, USA: *Bulletin of Volcanology*, v. 57, p. 151-169.
- Trench, D., 2008, The Termination of the Basin and Range Province into a Clockwise Rotating Region of Transtension and Volcanism, Central Oregon [Master's thesis]: Corvallis, OR, Oregon State University.
- Trench, D., Meigs, A., and Grunder, A., 2012, Termination of the northwestern Basin and Range province into a clockwise rotating region of transtension and volcanism, southeast Oregon: *Structural Geology*, v. 39, p. 52-65.
- Twiss, R.J., and Moores, E.M., 2006, *Structural Geology*: New York, NY, W.H. Freeman and Company, 736 p.
- Walker, G.W., 1974, Implications of late cenozoic volcanism to geothermal potential in the high lava plains of south-central Oregon: *Ore Bin*, v. 36.
- White, D., Hinkle, M., and Barnes, I., 1970, Mercury contents of natural thermal and mineral fluids: *US Geol. Surv. Prof. Pap.*, v. 713, p. 25-28.
- Wisian, K.W., Blackwell, D.D., and Richards, M., 1999, Heat flow in the Western United States and extensional geothermal systems, *Proceedings of the 24th Workshop on Geothermal Reservoir Engineering*, Stanford University, Stanford, California, Jan, p. 25-27.

APPENDICES

APPENDIX A

Normalized Whole Rock XRF Data (Conventional XRF)
NAD83 UTM11

Sample ID	GB037-10	GB131-10	GB130-10	GB120-10	GB067b-10
NORTHING	4826032.4	4825667.5	4826660.3	4830627.2	4831660.3
EASTING	266190.7	260808.7	264267.3	247167.9	258877.7
SiO ₂ (wt.%)	49.92	46.66	48.98	48.85	49.46
TiO ₂ (wt.%)	1.53	2.64	1.79	1.11	1.69
Al ₂ O ₃ (wt.%)	17.07	15.71	16.61	17.21	16.66
FeO* (wt.%)	10.62	12.77	11.54	9.51	11.01
MnO (wt.%)	0.18	0.23	0.19	0.17	0.19
MgO (wt.%)	6.88	7.16	6.76	8.91	6.81
CaO (wt.%)	9.58	10.56	10.01	10.89	10.00
Na ₂ O (wt.%)	3.32	3.12	3.28	2.82	3.28
K ₂ O (wt.%)	0.56	0.53	0.45	0.33	0.50
P ₂ O ₅ (wt.%)	0.34	0.61	0.39	0.19	0.39
Total	100	100	100	100	100
Ni (ppm)	101	88	77	159	76
Cr (ppm)	127	143	145	248	142
Sc (ppm)	31	41	35	34	33
V (ppm)	235	330	265	216	245
Ba (ppm)	346	217	315	144	471
Rb (ppm)	8	8	6	4	5
Sr (ppm)	310	223	305	240	320
Zr (ppm)	132	206	130	81	131
Y (ppm)	32	48	38	23	34
Nb (ppm)	7.3	18.9	7.1	6.7	7
Ga (ppm)	19	19	19	16	19
Cu (ppm)	62	62	79	110	63
Zn (ppm)	95	111	99	64	95
Pb (ppm)	3	2	2	1	2
La (ppm)	16	16	10	5	12
Ce (ppm)	27	37	29	21	25
Nd (ppm)	18	25	20	13	20
U (ppm)	1	3	2	0	1

APPENDIX A (continued)

Normalized Whole Rock XRF Data (Conventional XRF)

Sample ID	GB085-10	GB116-10	GB121a-10	GB064-10	GB118-10
NORTHING	4830218.5	4824532.2	4825286.6	4828327.0	4825153.9
EASTING	258303.2	266431.6	247989.1	247982.5	266665.9
SiO ₂ (wt.%)	46.72	47.18	50.42	67.05	50.35
TiO ₂ (wt.%)	2.47	1.97	2.40	1.12	1.65
Al ₂ O ₃ (wt.%)	16.01	16.21	15.64	13.63	16.56
FeO* (wt.%)	12.44	12.81	13.11	6.07	10.80
MnO (wt.%)	0.22	0.22	0.22	0.14	0.19
MgO (wt.%)	7.46	7.65	4.57	1.71	6.51
CaO (wt.%)	10.65	10.35	8.66	4.15	9.56
Na ₂ O (wt.%)	3.01	3.09	3.55	4.37	3.37
K ₂ O (wt.%)	0.47	0.23	0.72	1.36	0.66
P ₂ O ₅ (wt.%)	0.54	0.29	0.70	0.40	0.36
Total	100	100	100	100	100
Ni (ppm)	93	103	34	5	79
Cr (ppm)	154	137	11	6	138
Sc (ppm)	42	38	32	21	34
V (ppm)	327	292	326	101	247
Ba (ppm)	221	317	516	487	358
Rb (ppm)	7	2	8	18	11
Sr (ppm)	228	244	377	162	298
Zr (ppm)	180	109	227	182	132
Y (ppm)	43	34	48	54	33
Nb (ppm)	16.9	4.8	11.5	7.1	7
Ga (ppm)	19	18	22	17	17
Cu (ppm)	68	55	39	11	62
Zn (ppm)	108	98	129	85	95
Pb (ppm)	1	2	3	5	3
La (ppm)	13	4	19	16	10
Ce (ppm)	38	21	48	35	24
Nd (ppm)	24	17	30	23	17
U (ppm)	1	3	1	1	1

APPENDIX A (continued)

Normalized Whole Rock XRF Data (Conventional XRF)

Sample ID	GB100-10	GB123-10	GB026-10	GB061-10	GB012-10
NORTHING	4827859.1	4829226.9	4820023.7	4828656.4	4831915.1
EASTING	244271.3	264255.6	257944.5	260170.0	251447.4
SiO ₂ (wt.%)	47.29	48.48	45.83	46.71	48.88
TiO ₂ (wt.%)	2.14	1.62	3.69	2.48	0.68
Al ₂ O ₃ (wt.%)	16.28	17.22	14.82	16.23	17.83
FeO* (wt.%)	12.96	10.99	15.40	12.51	8.24
MnO (wt.%)	0.22	0.19	0.27	0.23	0.16
MgO (wt.%)	7.26	7.46	5.20	7.14	9.68
CaO (wt.%)	9.87	10.15	9.36	10.64	12.03
Na ₂ O (wt.%)	3.23	3.20	3.64	3.02	2.29
K ₂ O (wt.%)	0.36	0.36	0.80	0.48	0.12
P ₂ O ₅ (wt.%)	0.38	0.35	0.99	0.56	0.10
Total	100	100	100	100	100
Ni (ppm)	89	105	41	91	193
Cr (ppm)	98	139	33	157	270
Sc (ppm)	35	33	41	41	38
V (ppm)	323	244	287	329	194
Ba (ppm)	205	264	336	229	128
Rb (ppm)	3	3	7	6	1
Sr (ppm)	300	319	285	229	195
Zr (ppm)	155	113	296	186	44
Y (ppm)	40	31	63	45	20
Nb (ppm)	9.5	6	29.2	17.8	1.9
Ga (ppm)	21	17	23	20	13
Cu (ppm)	52	60	47	38	90
Zn (ppm)	110	94	140	107	54
Pb (ppm)	1	2	1	1	1
La (ppm)	12	10	23	15	5
Ce (ppm)	28	26	63	38	8
Nd (ppm)	20	20	38	24	4
U (ppm)	1	0	0	0	1

APPENDIX A (continued)

Normalized Whole Rock XRF Data (Conventional XRF)

Sample ID	GB066-10	GB126b-10	GB119-10	GB105-10	GB089-10
NORTHING	4828485.8	4831210.6	4823022.7	4829012.6	4827152.9
EASTING	244657.9	255985.8	265766.4	244924.4	262140.2
SiO ₂ (wt.%)	54.24	46.83	47.30	48.79	47.09
TiO ₂ (wt.%)	1.44	2.32	1.80	1.47	2.60
Al ₂ O ₃ (wt.%)	16.14	16.44	16.66	17.27	15.78
FeO* (wt.%)	9.51	12.11	12.53	10.56	12.64
MnO (wt.%)	0.17	0.22	0.21	0.18	0.23
MgO (wt.%)	4.43	7.47	7.63	7.81	6.75
CaO (wt.%)	8.51	10.74	10.37	10.18	10.67
Na ₂ O (wt.%)	3.80	2.95	2.98	3.13	3.10
K ₂ O (wt.%)	1.32	0.43	0.23	0.38	0.51
P ₂ O ₅ (wt.%)	0.45	0.49	0.28	0.23	0.63
Total	100	100	100	100	100
Ni (ppm)	23	100	109	126	88
Cr (ppm)	43	167	142	172	146
Sc (ppm)	32	41	36	33	42
V (ppm)	255	321	274	234	324
Ba (ppm)	701	182	343	155	319
Rb (ppm)	20	5	1	4	7
Sr (ppm)	666	231	254	258	230
Zr (ppm)	150	159	102	100	198
Y (ppm)	33	39	34	28	50
Nb (ppm)	7.9	14.1	4.4	5.1	18.7
Ga (ppm)	20	18	20	18	19
Cu (ppm)	109	62	71	96	74
Zn (ppm)	95	103	100	81	110
Pb (ppm)	6	2	1	2	2
La (ppm)	23	13	6	6	20
Ce (ppm)	49	29	18	17	38
Nd (ppm)	30	20	13	12	26
U (ppm)	1	1	0	1	1

APPENDIX A (continued)

Normalized Whole Rock XRF Data (Conventional XRF)

Sample ID	GB095-10	GB067c-10	GB038-10	GB131R-10
NORTHING	4826730.2	4831660.3	4827274.4	4825667.5
EASTING	258896.0	258877.7	259781.2	260808.7
SiO ₂ (wt.%)	75.05	76.48	76.73	46.66
TiO ₂ (wt.%)	0.22	0.11	0.11	2.65
Al ₂ O ₃ (wt.%)	14.43	12.91	12.90	15.74
FeO* (wt.%)	1.61	0.85	0.87	12.70
MnO (wt.%)	0.04	0.04	0.04	0.23
MgO (wt.%)	0.14	0.28	0.08	7.14
CaO (wt.%)	1.07	1.21	1.01	10.59
Na ₂ O (wt.%)	3.28	3.55	3.80	3.13
K ₂ O (wt.%)	4.10	4.55	4.33	0.53
P ₂ O ₅ (wt.%)	0.06	0.03	0.13	0.61
Total	100	100	100	100
Ni (ppm)	6	1	2	89
Cr (ppm)	3	2	4	144
Sc (ppm)	4	3	3	42
V (ppm)	8	5	1	326
Ba (ppm)	1186	1200	1475	219
Rb (ppm)	82	90	93	7
Sr (ppm)	89	71	80	220
Zr (ppm)	140	91	94	204
Y (ppm)	26	25	26	48
Nb (ppm)	7.4	7.4	7.3	19.7
Ga (ppm)	16	13	15	20
Cu (ppm)	7	5	4	63
Zn (ppm)	30	23	27	111
Pb (ppm)	17	17	17	1
La (ppm)	22	24	26	16
Ce (ppm)	39	39	50	43
Nd (ppm)	19	14	19	28
U (ppm)	3	3	4	0

APPENDIX B
Bruker pXRF Data
 NAD83 UTM11

Sample	GB020-11	GB027-10	GB035-10	GB036-10	GB051-10
NORTHING	4831356.8	4820948.1	4820635.7	4826894.2	4827075.4
EASTING	247400.7	264230.3	265466.8	263943.9	260991.4
SiO ₂	43.6	41.6	43.1	43.4	42.3
TiO ₂	0.73	1.64	2.51	1.69	2.44
Al ₂ O ₃	15.7	15.4	14.9	15.1	14.6
FeO*	8.44	11.13	13.1	11.35	12.85
MnO	0.159	0.188	0.216	0.193	0.226
MgO	19.4054	18.9483	15.299	17.7642	16.5388
CaO	11.62	10.68	10.06	10.08	10.34
K ₂ O	0.1	0.26	0.5	0.36	0.4
Total	99.83	99.83	99.83	99.83	99.83
Ni	189	140	68	111	89
Cr	374	313	213	254	233
V	200	253	275	271	285
Sr	183	265	275	316	220
Zr	46	108	188	115	171
Y	21	30	39	30	41
Nb	6	7	16	6	16
Cu	108	52	44	69	75
Zn	78	99	124	118	128

Sample	GB067A-10	GB086-10	GB099-10	GB115-10	GB122-10
NORTHING	4831660.3	4829186.6	4828019.8	4824414.1	4828240.4
EASTING	258877.7	257414.3	244613.5	265209.9	262847.7
SiO ₂	44.5	42.5	45	40.8	43.3
TiO ₂	1.75	2.51	1.6	1.95	1.66
Al ₂ O ₃	15	14.6	14.4	14.8	15.2
FeO*	11.79	12.91	10.79	13.5	11.24
MnO	0.204	0.231	0.197	0.22	0.194
MgO	16.4281	16.3005	17.9781	18.6249	17.9942
CaO	9.65	10.19	9.13	9.9	9.89
K ₂ O	0.49	0.47	0.7	0.2	0.38
Total	99.83	99.83	99.83	99.83	99.83
Ni	98	99	89	119	126
Cr	341	320	273	267	290
V	274	335	271	303	275
Sr	292	233	334	239	311
Zr	131	179	119	109	113
Y	32	44	33	34	31
Nb	6	16	6	5	5
Cu	73	93	94	74	79
Zn	122	136	116	119	117

APPENDIX B (continued)
Bruker pXRF Data

Sample	GB125-10	GB132-11	GB133TB6A-11	GB133TB6B-11	GB134-11
NORTHING	4831391.1	4820166.0	4819808.0	4819808.0	4819259.8
EASTING	261218.5	255941.5	254535.0	254535.0	254544.1
SiO ₂	45.8	39.9	50.8	50.4	48.2
TiO ₂	1.53	1.05	1.47	1.46	1.26
Al ₂ O ₃	14	15.6	15.1	15	14.9
FeO*	10.26	9.35	9.09	9.01	8.67
MnO	0.185	0.162	0.162	0.164	0.152
MgO	18.3441	23.3997	13.3001	13.9255	17.0232
CaO	9.11	10.45	8.18	8.19	8.55
K ₂ O	0.58	0.21	1.53	1.53	0.99
Total	99.83	99.83	99.86	99.83	99.81
Ni	93	157	40	43	55
Cr	307	204	193	180	240
V	262	224	231	238	227
Sr	276	298	647	646	445
Zr	129	49	158	153	123
Y	33	23	34	38	27
Nb	6	2	7	6	6
Cu	77	99	111	112	98
Zn	118	85	120	121	110

Sample	GB136-11	GB137-11	GB138-11	GB140N-11	GB140S-11
NORTHING	4819409.2	4819227.6	4818446.8	4820842.9	4820842.9
EASTING	254982.5	255526.3	256673.2	259398.1	259398.1
SiO ₂	49.1	47.3	42.8	42.7	42.6
TiO ₂	1.3	1.31	1.75	1.7	1.69
Al ₂ O ₃	15.2	14.6	15.2	14.9	15.2
FeO*	8.82	8.9	13.35	12.98	12.54
MnO	0.156	0.162	0.226	0.221	0.218
MgO	15.3338	17.7776	15.9174	16.5043	17.4619
CaO	8.76	8.61	10.34	10.53	9.94
K ₂ O	1.04	1.15	0.24	0.31	0.29
Total	99.85	99.83	99.83	99.83	99.83
Ni	62	58	128	124	111
Cr	217	249	265	256	217
V	242	238	312	305	300
Sr	454	448	283	279	279
Zr	127	123	86	88	90
Y	27	28	34	32	35
Nb	6	7	5	6	4
Cu	120	114	108	123	96
Zn	111	118	120	125	114

APPENDIX B (continued)
Bruker pXRF Data

Sample	GB141-11	GB143-11	GB144-11	GB146-11	GB147-11
NORTHING	4819012.7	4818539.0	4817918.9	4818133.6	4817801.0
EASTING	258602.6	254597.7	256220.7	256831.4	257656.7
SiO ₂	42.7	48.2	43.3	42.3	42.7
TiO ₂	1.78	1.36	1.63	1.78	1.65
Al ₂ O ₃	15.2	15.1	15.2	14.7	14.8
FeO*	13.42	8.89	12.81	13.36	12.72
MnO	0.226	0.161	0.208	0.226	0.226
MgO	16.2183	16.4251	16.5134	17.2208	17.8092
CaO	10.12	8.66	9.9	10.07	9.63
K ₂ O	0.23	0.99	0.35	0.22	0.36
Total	99.83	99.88	99.83	99.83	99.83
Ni	122	57	93	112	97
Cr	275	239	217	272	243
V	333	237	292	321	298
Sr	303	448	381	264	377
Zr	84	120	253	90	83
Y	39	26	41	36	30
Nb	5	6	5	2	3
Cu	106	96	127	80	107
Zn	121	108	119	119	131

Sample	GB149-11	GB151-11	GB153-11	GB155-11	GB157-11
NORTHING	4817059.6	4820227.2	4820859.9	4820815.4	4819656.0
EASTING	256851.9	255877.2	253678.4	262096.0	262472.9
SiO ₂	48	44	49.7	43.6	41.8
TiO ₂	1.31	1.16	1.41	2.14	2.09
Al ₂ O ₃	14.6	16	14.6	14.6	14.5
FeO*	8.91	10.74	8.86	11.84	11.23
MnO	0.161	0.18	0.161	0.196	0.187
MgO	17.1824	16.34	15.0845	17.8568	21.1503
CaO	8.54	11.18	8.39	8.91	8.4
K ₂ O	1.1	0.22	1.52	0.68	0.69
Total	99.83	99.89	99.87	99.83	99.89
Ni	63	184	41	139	122
Cr	288	294	184	395	445
V	251	265	217	247	224
Sr	437	290	634	327	315
Zr	120	52	154	199	203
Y	27	24	34	32	34
Nb	4	2	6	20	20
Cu	100	132	111	51	67
Zn	115	92	113	114	108

APPENDIX B (continued)
Bruker pXRF Data

Sample	GB158-11	GB159-11	GB160-11	GB160-11	GB163-11
NORTHING	4819918.2	4819993.3	4824532.2	4819203.5	4817335.8
EASTING	262521.3	263684.5	266431.6	263782.1	263634.6
SiO ₂	44.4	47.7	41.9	42.1	41.1
TiO ₂	1.6	1.62	1.7	1.75	1.23
Al ₂ O ₃	14.7	15.6	15.1	14.7	14.9
FeO*	10.37	10.33	13.29	13.51	10.79
MnO	0.186	0.178	0.21	0.215	0.181
MgO	17.9393	13.8238	17.54	17.3566	20.911
CaO	10.01	9.96	10.03	10.02	10.71
K ₂ O	0.58	0.48	0.21	0.22	0.21
Total	99.86	99.84	99.92	99.83	99.86
Ni	126	159	115	114	168
Cr	359	356	218	277	438
V	246	245	300	310	274
Sr	274	299	267	265	290
Zr	149	138	87	85	53
Y	30	32	34	33	24
Nb	14	10	5	3	3
Cu	67	79	122	124	137
Zn	106	111	122	120	103

Sample	GB164-11	GB166-11	GB172-11	GB173-11	GB174-11
NORTHING	4816656.7	4817187.5	4820192.0	4820472.1	4820571.8
EASTING	264588.3	265340.1	265415.4	265468.7	265606.6
SiO ₂	43.7	43.8	42.6	43.5	43.7
TiO ₂	1.4	1.85	2.1	2.44	2.41
Al ₂ O ₃	15.3	14.9	14.7	14.7	15.4
FeO*	9.9	11.63	11.44	13.29	12.07
MnO	0.192	0.201	0.192	0.225	0.207
MgO	18.1252	16.3282	19.4617	15.0434	15.2795
CaO	10.98	10.61	8.66	10.1	9.95
K ₂ O	0.23	0.37	0.7	0.42	0.57
Total	99.83	99.83	99.83	99.83	99.86
Ni	152	128	135	75	75
Cr	409	308	325	273	154
V	243	276	236	287	286
Sr	237	238	317	239	275
Zr	100	154	210	174	196
Y	26	35	36	39	40
Nb	6	13	20	17	21
Cu	74	101	59	78	60
Zn	98	126	134	123	117

APPENDIX B (continued)
Bruker pXRF Data

Sample	GB175-11	GB176-11	GB180L-11	GB181-11	GB184-11
NORTHING	4820422.8	4820353.1	4818915.5	4817761.8	4821932.2
EASTING	264469.8	266115.7	246415.8	247251.5	246096.9
SiO ₂	41.5	44.9	45.1	47.8	43.3
TiO ₂	1.58	1.62	1.58	1.22	2.61
Al ₂ O ₃	15	15.5	15.3	15.1	14.6
FeO*	10.76	10.36	10.94	8.65	14.95
MnO	0.19	0.187	0.201	0.154	0.233
MgO	19.7288	16.6857	16.973	16.8771	14.3815
CaO	10.89	10.03	9.26	8.96	9.29
K ₂ O	0.27	0.45	0.45	1.06	0.42
Total	99.83	99.83	99.87	99.83	99.83
Ni	150	136	85	79	65
Cr	312	380	406	226	207
V	265	245	260	220	329
Sr	254	285	318	462	304
Zr	102	141	124	118	185
Y	31	28	36	25	43
Nb	8	13	6	6	11
Cu	90	89	57	94	88
Zn	98	103	115	111	147

Sample	GB186TB22-11	GB188-11	GB189-11	GB190-11	GB195-11
NORTHING	4825640.1	4827476.8	4827859.6	4828468.0	4833779.7
EASTING	247330.7	246162.1	245474.5	243918.2	250817.5
SiO ₂	45.4	41.1	46.1	43.1	42.4
TiO ₂	1.29	0.63	1.32	1.51	1.64
Al ₂ O ₃	15	15.5	14.5	15.1	15.4
FeO*	9.05	7.78	9.31	10.83	11.15
MnO	0.164	0.146	0.175	0.183	0.196
MgO	19.0749	23.0477	18.3287	18.6584	18.5476
CaO	9.21	11.7	9.29	10.25	10.19
K ₂ O	0.75	0.1	0.81	0.31	0.37
Total	99.93	99.83	99.83	99.83	99.83
Ni	83	186	82	146	151
Cr	284	420	298	316	336
V	247	189	250	260	263
Sr	477	179	482	263	262
Zr	107	37	117	97	130
Y	25	17	28	26	31
Nb	7	1	7	4	7
Cu	88	60	116	73	69
Zn	108	70	111	102	112

APPENDIX B (continued)
Bruker pXRF Data

Sample	GB196-11	GB197-11	GB198-11	GB199-11	GB200-11
NORTHING	4831920.4	4835291.0	4834497.6	4834818.0	4831167.5
EASTING	253602.1	253241.0	257576.6	257777.7	260400.7
SiO ₂	44	42.5	41.2	49	44
TiO ₂	0.89	0.96	2.38	2.34	1.79
Al ₂ O ₃	15.5	15.3	14.6	14.2	15.2
FeO*	9.12	9.18	12.54	10.62	11.56
MnO	0.169	0.174	0.22	0.206	0.194
MgO	18.4977	20.4709	17.7782	14.8795	17.0485
CaO	11.43	11.11	10.55	7.26	9.59
K ₂ O	0.17	0.13	0.45	1.23	0.44
Total	99.83	99.81	99.87	99.87	99.88
Ni	201	194	101	12	75
Cr	546	435	262	88	213
V	222	231	325	240	270
Sr	208	201	224	344	295
Zr	58	63	175	262	129
Y	22	23	43	54	33
Nb	4	3	17	13	9
Cu	51	282	120	38	74
Zn	81	175	136	152	123

Sample	GB201-11	GB202-11	GB203-11	GB204-11	GB205-11
NORTHING	4832635.3	4832562.4	4832884.9	4831749.1	4831864.2
EASTING	259432.1	258814.8	261990.4	265525.8	265422.7
SiO ₂	50.7	43.8	46.3	46.8	46.7
TiO ₂	2.36	1.81	2.65	2.64	2.64
Al ₂ O ₃	14.7	14.8	14.5	14.5	14.7
FeO*	10.98	11.97	12.19	12.34	12.3
MnO	0.209	0.204	0.226	0.225	0.224
MgO	12.4713	16.8615	15.3335	14.5085	14.1938
CaO	6.92	9.91	7.43	7.64	7.97
K ₂ O	1.27	0.43	1.1	0.86	0.84
Total	99.83	99.83	99.83	99.84	99.84
Ni	15	87	-6	0	7
Cr	153	325	61	52	43
V	247	280	255	245	242
Sr	342	301	427	394	379
Zr	263	130	260	274	267
Y	54	32	56	62	56
Nb	15	7	13	15	16
Cu	22	82	29	31	24
Zn	162	123	162	156	151

APPENDIX B (continued)
Bruker pXRF Data

Sample	GB206-11	GB207-11	GB210-11	GB212-11	GB214-11
NORTHING	4831487.7	4833454.6	4835840.2	4823981.4	4821717.3
EASTING	267367.2	266521.7	263436.9	260425.2	242958.4
SiO ₂	46	47	43	42.3	43.6
TiO ₂	2.73	2.68	1.81	2.49	1.19
Al ₂ O ₃	14.7	14.9	14.9	14.6	15.6
FeO*	12.94	12.39	12.62	12.86	9.96
MnO	0.244	0.219	0.217	0.231	0.177
MgO	14.3264	13.7228	16.9856	16.3924	18.5698
CaO	7.95	7.67	10.05	10.33	10.62
K ₂ O	0.86	0.87	0.27	0.47	0.25
Total	99.92	99.86	99.83	99.83	99.92
Ni	18	0	130	104	169
Cr	151	48	293	270	321
V	288	242	303	311	244
Sr	390	389	302	223	212
Zr	270	263	98	184	74
Y	57	55	33	43	23
Nb	17	14	5	18	4
Cu	35	28	100	66	92
Zn	153	161	120	129	100

Sample	GB215-11	GB217-11	GB218-11	GBP2-11	P1-11
NORTHING	4823547.8	4833776.2	4834479.0	4828011.4	4828334.8
EASTING	243323.8	246066.6	245677.7	245679.1	245402.9
SiO ₂	43	56.4	57	42.2	43.3
TiO ₂	1.43	1.41	1.39	0.78	1.26
Al ₂ O ₃	15.3	14.3	14.3	15.3	14.7
FeO*	10.88	7.84	7.66	8.62	9.01
MnO	0.186	0.211	0.203	0.16	0.167
MgO	18.902	12.6352	12.1341	21.2569	21.902
CaO	9.91	5.15	5.11	11.44	8.99
K ₂ O	0.29	1.73	1.74	0.12	0.71
Total	99.84	99.83	99.82	99.83	99.91
Ni	163	16	19	233	78
Cr	285	198	94	419	349
V	259	124	122	206	232
Sr	254	302	288	196	446
Zr	93	212	209	50	102
Y	27	56	56	22	26
Nb	7	13	14	0	6
Cu	77	8	14	60	82
Zn	104	141	143	80	103

APPENDIX B (continued)
Bruker pXRF Data

Sample	P5-11	P6-11	P7-11	P8-11	P9-11
NORTHING	4828968.3	4828438.5	4828479.6	4828511.4	4828569.7
EASTING	244405.9	244716.0	244696.5	244653.4	244698.9
SiO ₂	43.4	45.9	46.4	48.3	45.4
TiO ₂	1.49	1.26	1.24	1.5	1.67
Al ₂ O ₃	15.2	15.3	15.5	14.7	13.3
FeO*	10.66	8.81	8.78	9.41	6.93
MnO	0.182	0.162	0.162	0.166	0.151
MgO	18.4833	18.5065	17.5971	16.2281	26.0614
CaO	10.17	9.08	9.39	8.17	5.41
K ₂ O	0.34	0.78	0.72	1.22	1.13
Total	99.86	99.88	99.86	99.81	99.93
Ni	145	69	87	41	-43
Cr	287	320	195	157	34
V	254	238	222	257	158
Sr	262	455	473	652	212
Zr	98	113	106	147	122
Y	27	29	25	32	38
Nb	6	6	6	7	7
Cu	85	89	94	137	-18
Zn	96	110	105	124	98

APPENDIX C

Calibration curves for Bruker portable XRF

Al KA1/OSU BASALT 45

OSU BASALT 45

Abridged calibration data for line Al KA1/OSU BASALT 45

S/N 1593, Mask: 30 mm, Mode: Air, 45 kV, 0.025 mA, Filter: None

Detector parameter 1: 600 parameter 2: 400

Peak Channels[trapeze]: 1.412 - 1.555 keV

Calibration data for compound Al₂O₃ in original sample

Absorption correction: Variable alphas

Intensity model: net intensity

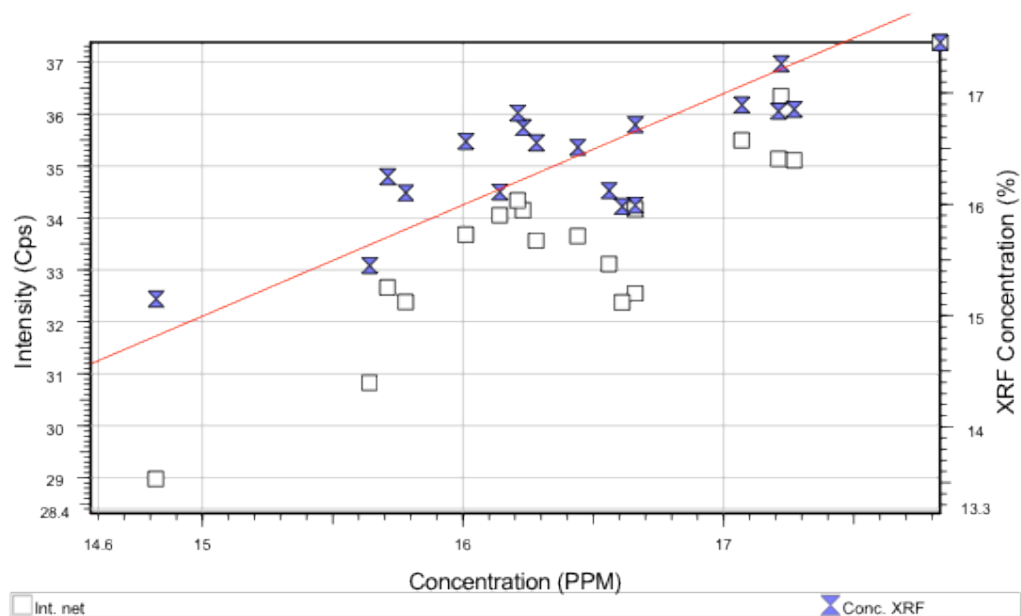
Minimization target: absolute error, 19 standards from 14.82 % to 17.83 %

Standard deviation: 0.41 %

Squared correlation coefficient: 0.662893

Slope: 0.1909 %/Cps / Sensitivity: 5.239 Cps/% (Adjustable by regression)

Corrected intensity offset: +29.29 Cps (Adjustable by regression) or -5.5907 %



Ca KA1/OSU BASALT 45

OSU BASALT 45

Abridged calibration data for line Ca KA1/OSU BASALT 45

S/N 1593, Mask: 30 mm, Mode: Air, 45 kV, 0.025 mA, Filter: None

Detector parameter 1: 600 parameter 2: 400

Peak Channels[trapeze]: 3.567 - 3.817 keV

Calibration data for compound CaO in original sample

Absorption correction: Variable alphas

Intensity model: net intensity

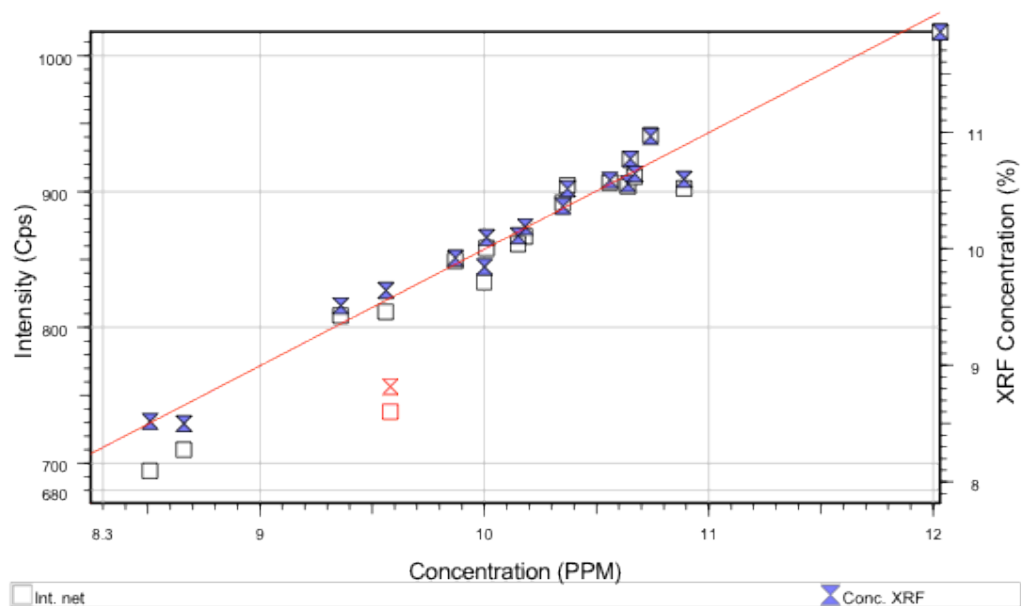
Minimization target: absolute error, 18 standards from 8.51 % to 12.03 %

Standard deviation: 0.133 %

Squared correlation coefficient: 0.973713

Slope: 0.01379 %/Cps / Sensitivity: 72.5 Cps/% (Adjustable by regression)

Corrected intensity offset: +53.79 Cps (Adjustable by regression) or -0.7420 %



Cr KA1/OSU BASALT 45

OSU BASALT 45

Abridged calibration data for line Cr KA1/OSU BASALT 45

S/N 1593, Mask: 30 mm, Mode: Air, 45 kV, 0.025 mA, Filter: None

Detector parameter 1: 600 parameter 2: 400

Peak Channels[trapeze]: 5.31 - 5.52 keV

Calibration data for compound Cr in original sample

Absorption correction: Variable alphas

Intensity model: net intensity

Minimization target: absolute error, 19 standards from 11 PPM to 270 PPM

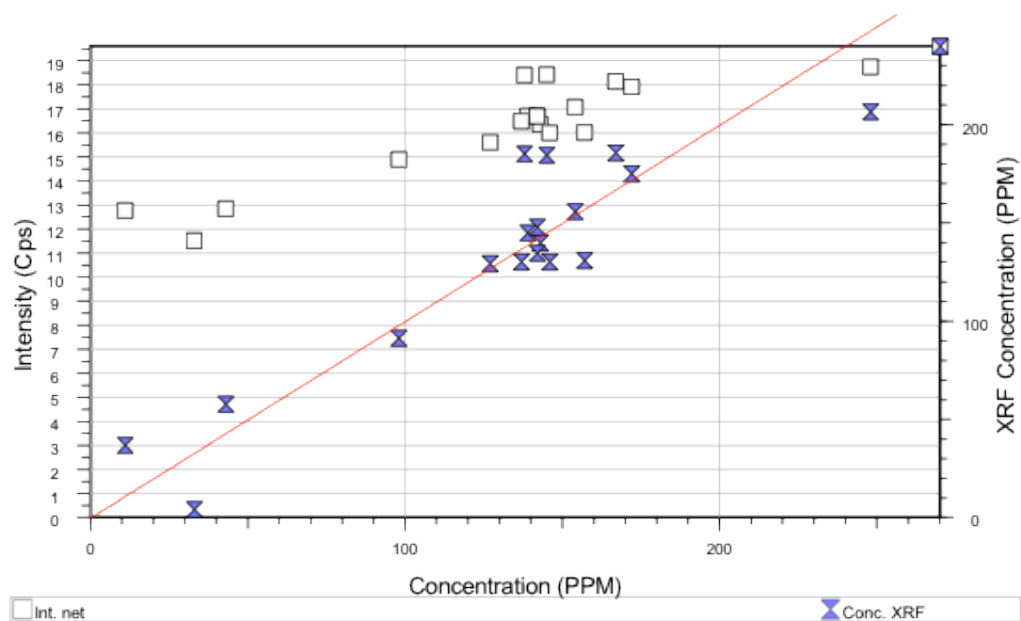
Standard deviation: 23 PPM

Squared correlation coefficient: 0.862755

Slope: 0.003978 %/Cps / Sensitivity: 251.4 Cps/% (Adjustable by regression)

Corrected intensity offset: -4.672 Cps (Adjustable by regression) or 185.9 PPM

Line overlap correction by Intensity (Fe KA1/OSU BASALT 45) * (-0.001037) (Adjustable by regression)



Cu KA1/OSU BASALT 45

OSU BASALT 45

Abridged calibration data for line Cu KA1/OSU BASALT 45

S/N 1593, Mask: 30 mm, Mode: Air, 45 kV, 0.025 mA, Filter: None

Detector parameter 1: 600 parameter 2: 400

Peak Channels[trapeze]: 7.943 - 8.152 keV

Calibration data for compound Cu in original sample

Absorption correction: Variable alphas

Intensity model: net intensity

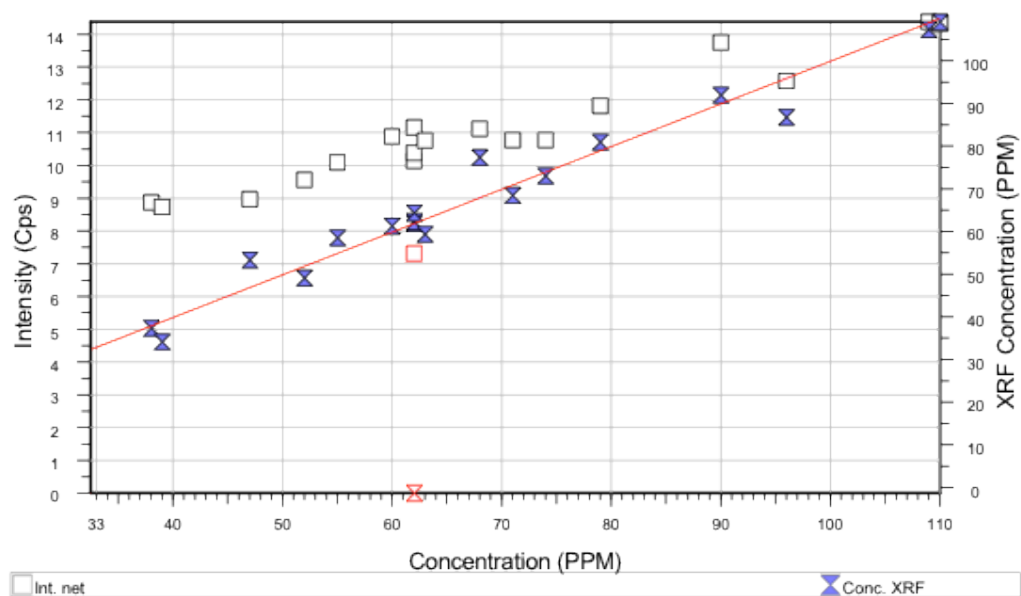
Minimization target: absolute error, 18 standards from 38 PPM to 110 PPM

Standard deviation: 4 PPM

Squared correlation coefficient: 0.961447

Slope: 0.00298 %/Cps / Sensitivity: 335.6 Cps/% (Adjustable by regression)

Corrected intensity offset: -4.126 Cps (Adjustable by regression) or 122.9 PPM



Fe KA1/OSU BASALT 45

OSU BASALT 45

Abridged calibration data for line Fe KA1/OSU BASALT 45

S/N 1593, Mask: 30 mm, Mode: Air, 45 kV, 0.025 mA, Filter: None

Detector parameter 1: 600 parameter 2: 400

Peak Channels[trapeze]: 6.245 - 6.559 keV

Calibration data for compound FeO in original sample

Absorption correction: Variable alphas

Intensity model: net intensity

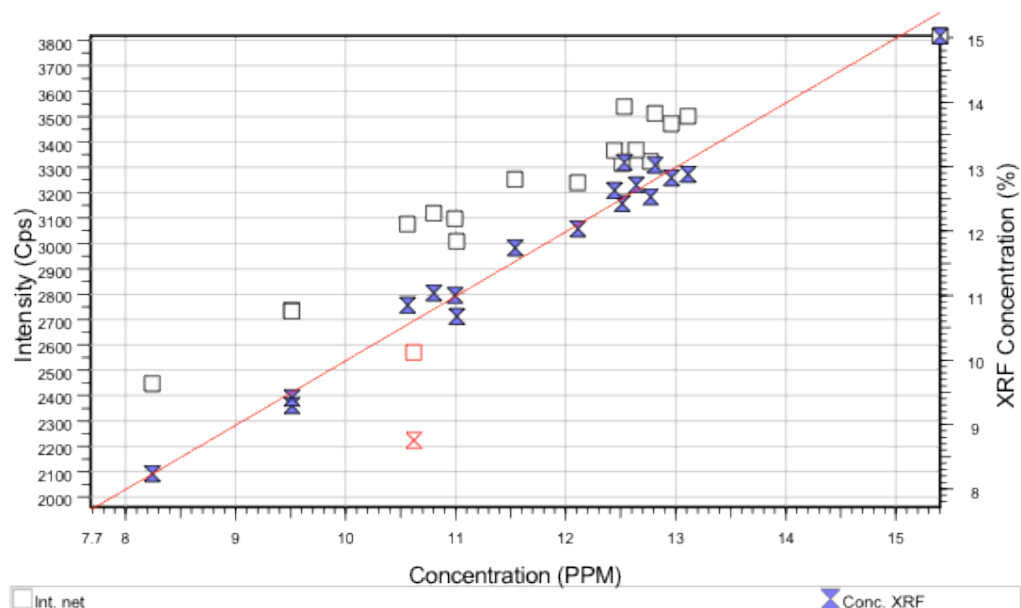
Minimization target: absolute error, 18 standards from 8.24 % to 15.40 %

Standard deviation: 0.243 %

Squared correlation coefficient: 0.978762

Slope: 0.007139 %/Cps / Sensitivity: 140.1 Cps/% (Adjustable by regression)

Corrected intensity offset: -218.7 Cps (Adjustable by regression) or 1.5612 %



K KA1/OSU BASALT 45

OSU BASALT 45

Abridged calibration data for line K KA1/OSU BASALT 45

S/N 1593, Mask: 30 mm, Mode: Air, 45 kV, 0.025 mA, Filter: None

Detector parameter 1: 600 parameter 2: 400

Peak Channels[trapeze]: 3.224 - 3.404 keV

Calibration data for compound K2O in original sample

Absorption correction: Variable alphas

Intensity model: net intensity

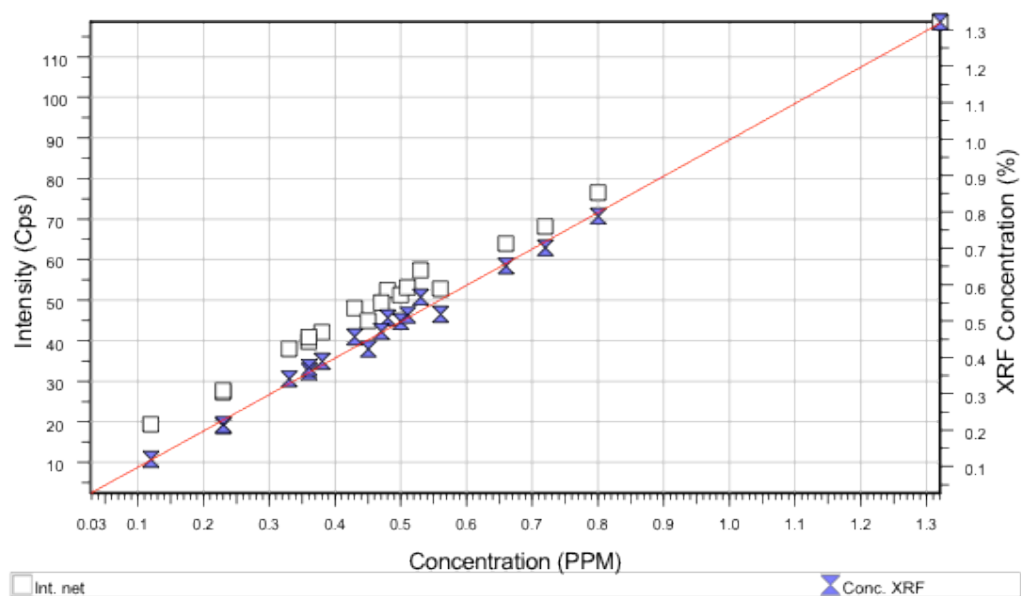
Minimization target: absolute error, 19 standards from 0.12 % to 1.32 %

Standard deviation: 0.0193 %

Squared correlation coefficient: 0.994499

Slope: 0.0132 %/Cps / Sensitivity: 75.74 Cps/% (Adjustable by regression)

Corrected intensity offset: -8.392 Cps (Adjustable by regression) or 0.1108 %



Mg KA1/OSU BASALT 45

OSU BASALT 45

Abridged calibration data for line Mg KA1/OSU BASALT 45

S/N 1593, Mask: 30 mm, Mode: Air, 45 kV, 0.025 mA, Filter: None

Detector parameter 1: 600 parameter 2: 400

Peak Channels[trapeze]: 1.183 - 1.284 keV

Calibration data for compound MgO in original sample

Absorption correction: Variable alphas

Intensity model: net intensity

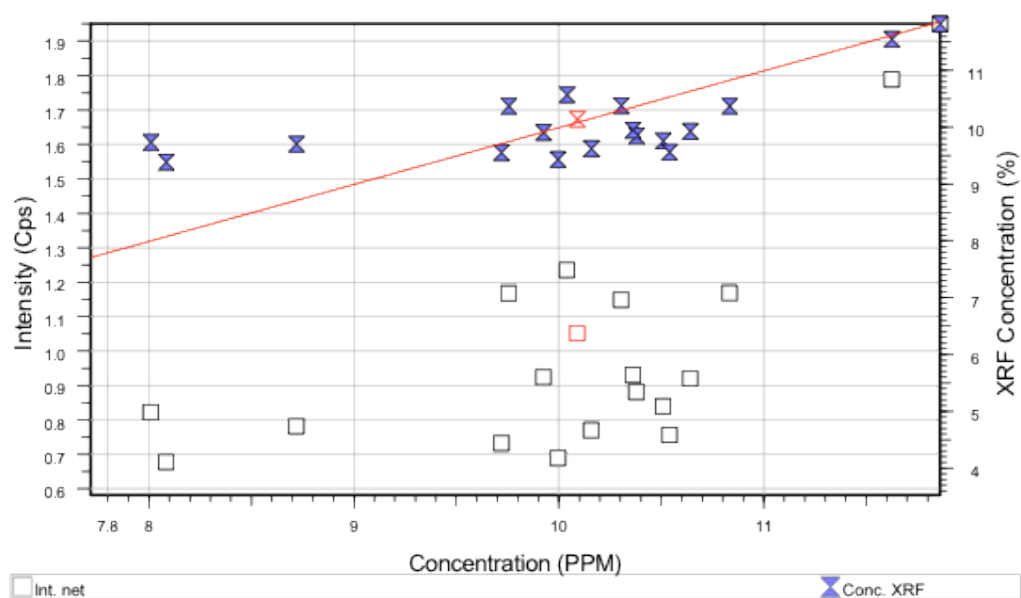
Minimization target: absolute error, 18 standards from 8.01 % to 11.86 %

Standard deviation: 0.752 %

Squared correlation coefficient: 0.448799

Slope: 1.002 %/Cps / Sensitivity: 0.9982 Cps/% (Adjustable by regression)

Corrected intensity offset: +8.045 Cps (Adjustable by regression) or -8.0600 %



Mn KA1/OSU BASALT 45

OSU BASALT 45

Abridged calibration data for line Mn KA1/OSU BASALT 45

S/N 1593, Mask: 30 mm, Mode: Air, 45 kV, 0.025 mA, Filter: None

Detector parameter 1: 600 parameter 2: 400

Peak Channels[trapeze]: 5.774 - 6.02 keV

Calibration data for compound MnO in original sample

Absorption correction: Variable alphas

Intensity model: net intensity

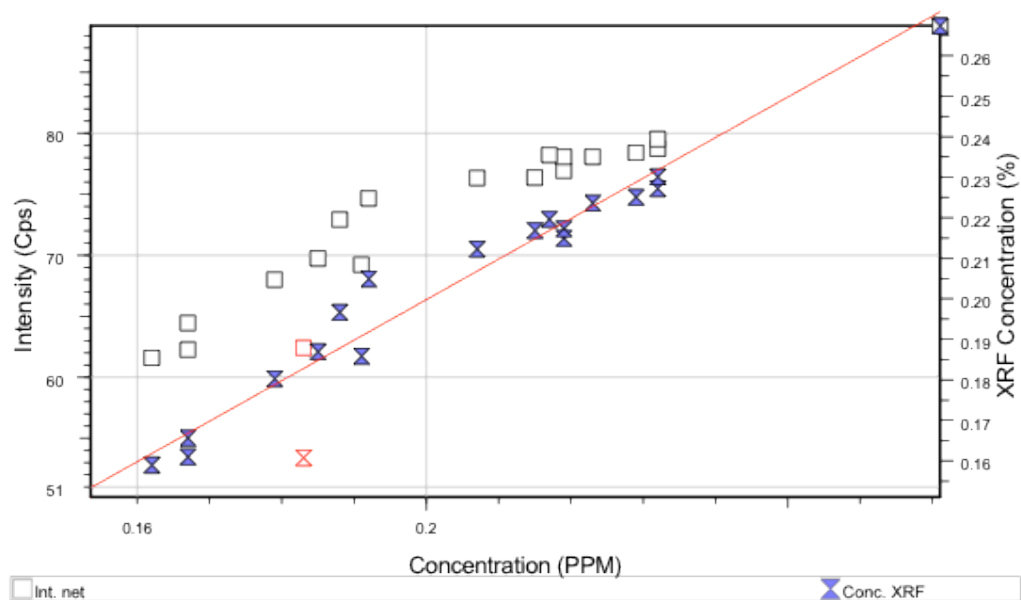
Minimization target: absolute error, 18 standards from 1620 PPM to 2710 PPM

Standard deviation: 51 PPM

Squared correlation coefficient: 0.968532

Slope: 0.00524 %/Cps / Sensitivity: 190.9 Cps/% (Adjustable by regression)

Corrected intensity offset: -8.269 Cps (Adjustable by regression) or 433.2 PPM



Nb KA1/OSU BASALT 45

OSU BASALT 45

Abridged calibration data for line Nb KA1/OSU BASALT 45

S/N 1593, Mask: 30 mm, Mode: Air, 45 kV, 0.025 mA, Filter: None

Detector parameter 1: 600 parameter 2: 400

Peak Channels[trapeze]: 16.44 - 16.78 keV

Calibration data for compound Nb in original sample

Absorption correction: Variable alphas

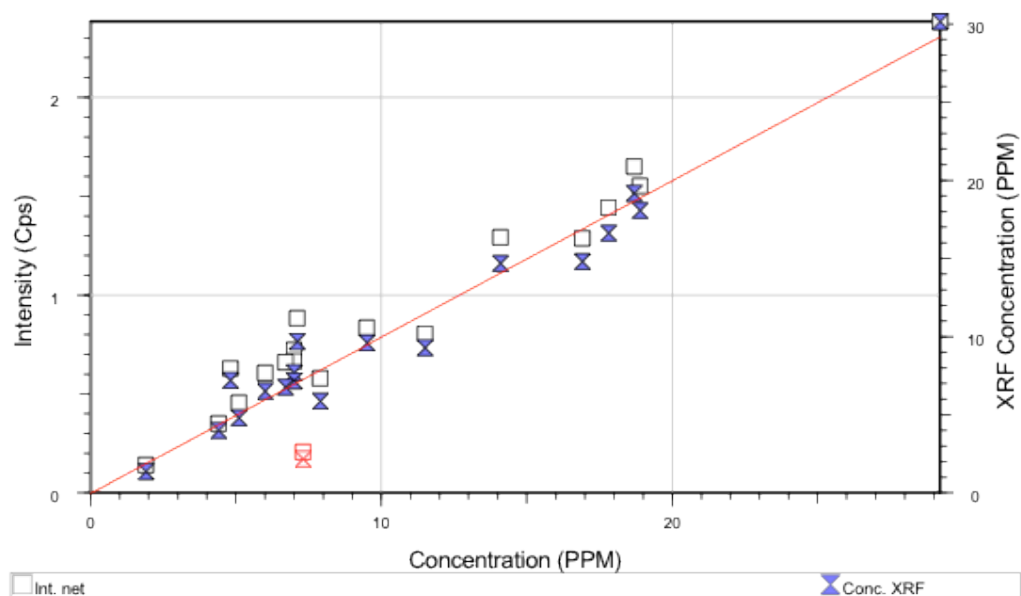
Intensity model: net intensity

Minimization target: absolute error, 18 standards from 2 PPM to 29 PPM

Standard deviation: 1 PPM

Squared correlation coefficient: 0.963850

Slope: 0.006963 %/Cps / Sensitivity: 143.6 Cps/% (Adjustable by regression)



Ni KA1/OSU BASALT 45

OSU BASALT 45

Abridged calibration data for line Ni KA1/OSU BASALT 45

S/N 1593, Mask: 30 mm, Mode: Air, 45 kV, 0.025 mA, Filter: None

Detector parameter 1: 600 parameter 2: 400

Peak Channels[trapeze]: 7.339 - 7.585 keV

Calibration data for compound Ni in original sample

Absorption correction: Variable alphas

Intensity model: net intensity

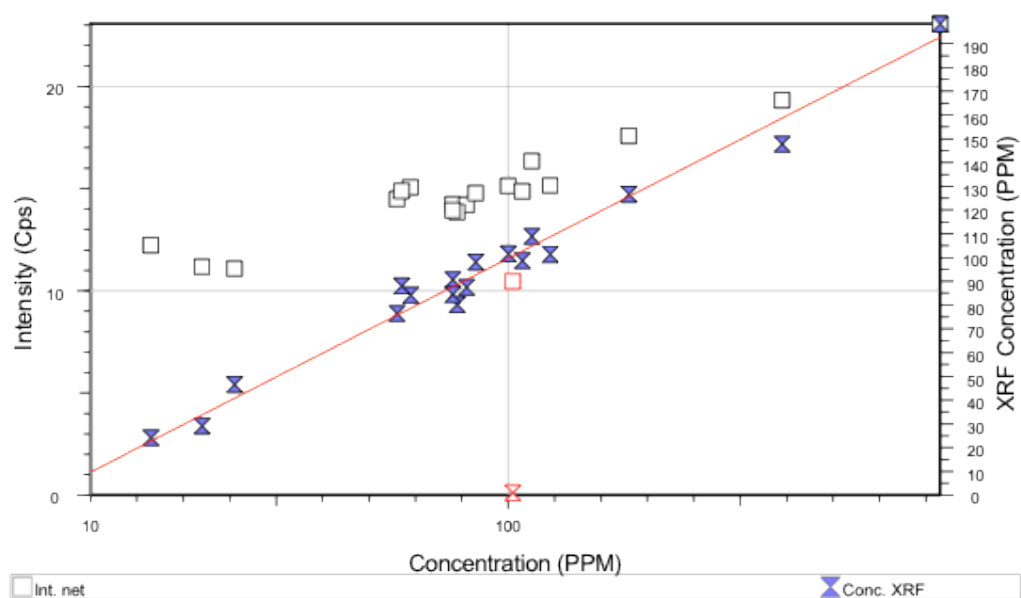
Minimization target: absolute error, 18 standards from 23 PPM to 193 PPM

Standard deviation: 6 PPM

Squared correlation coefficient: 0.978785

Slope: 0.002974 %/Cps / Sensitivity: 336.2 Cps/% (Adjustable by regression)

Corrected intensity offset: -6.14 Cps (Adjustable by regression) or 182.6 PPM



Si KA1/OSU BASALT 45

OSU BASALT 45

Abridged calibration data for line Si KA1/OSU BASALT 45

S/N 1593, Mask: 30 mm, Mode: Air, 45 kV, 0.025 mA, Filter: None

Detector parameter 1: 600 parameter 2: 400

Peak Channels[trapeze]: 1.634 - 1.845 keV

Calibration data for compound SiO₂ in original sample

Absorption correction: Variable alphas

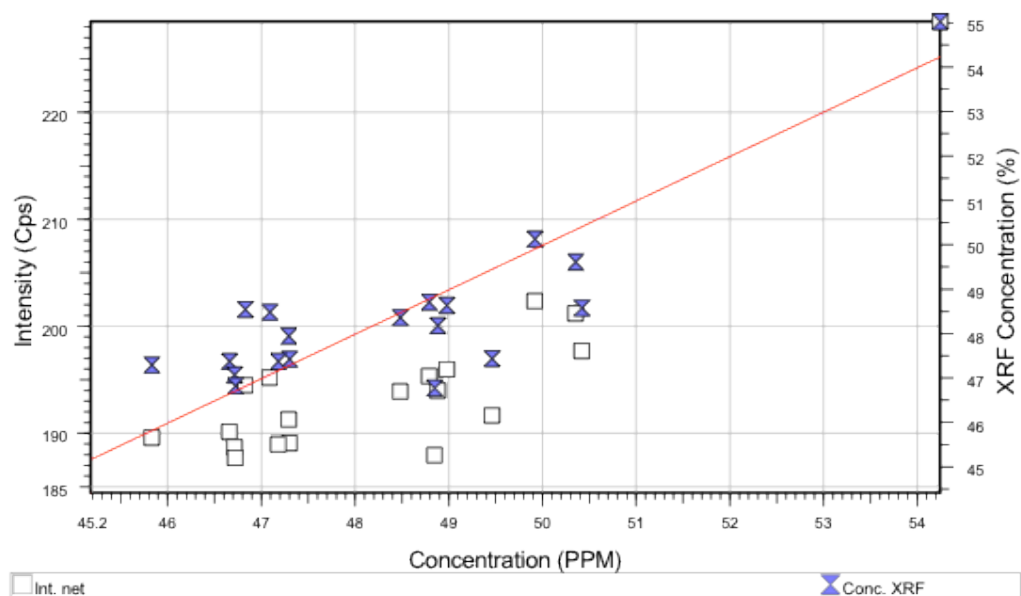
Intensity model: net intensity

Minimization target: absolute error, 19 standards from 45.83 % to 54.24 %

Standard deviation: 1.1 %

Squared correlation coefficient: 0.697372

Slope: 0.1713 %/Cps / Sensitivity: 5.837 Cps/% (Adjustable by regression)



Sr KA1/OSU BASALT 45

OSU BASALT 45

Abridged calibration data for line Sr KA1/OSU BASALT 45

S/N 1593, Mask: 30 mm, Mode: Air, 45 kV, 0.025 mA, Filter: None

Detector parameter 1: 600 parameter 2: 400

Peak Channels[trapeze]: 13.98 - 14.32 keV

Calibration data for compound Sr in original sample

Absorption correction: Variable alphas

Intensity model: net intensity

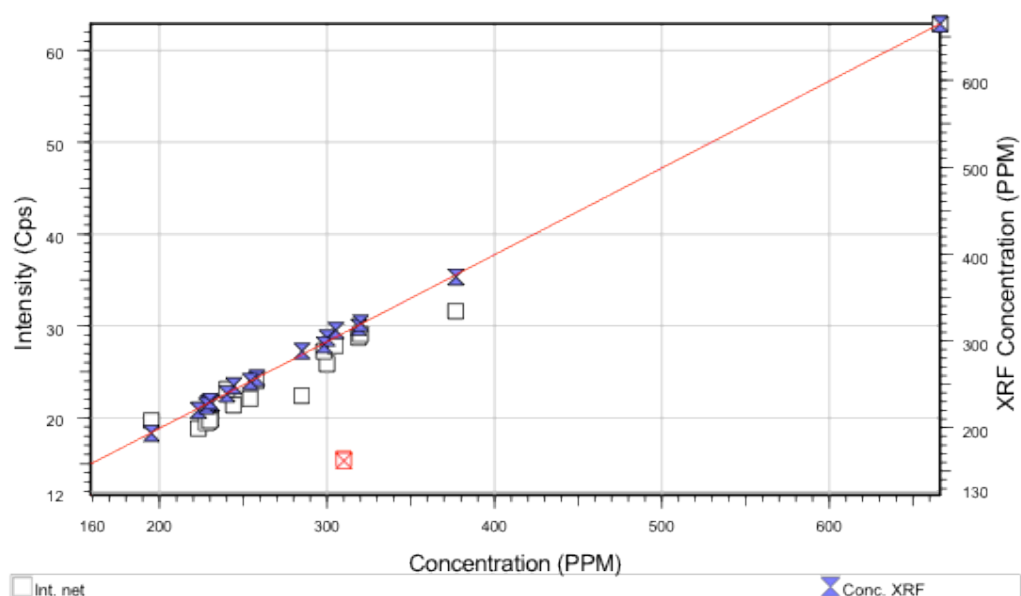
Minimization target: absolute error, 18 standards from 195 PPM to 666 PPM

Standard deviation: 3 PPM

Squared correlation coefficient: 0.999216

Slope: 0.005165 %/Cps / Sensitivity: 193.6 Cps/% (Adjustable by regression)

Corrected intensity offset: -0.2332 Cps (Adjustable by regression) or 12.0 PPM



Ti KA1/OSU BASALT 45

OSU BASALT 45

Abridged calibration data for line Ti KA1/OSU BASALT 45

S/N 1593, Mask: 30 mm, Mode: Air, 45 kV, 0.025 mA, Filter: None

Detector parameter 1: 600 parameter 2: 400

Peak Channels[trapeze]: 4.385 - 4.638 keV

Calibration data for compound TiO₂ in original sample

Absorption correction: Variable alphas

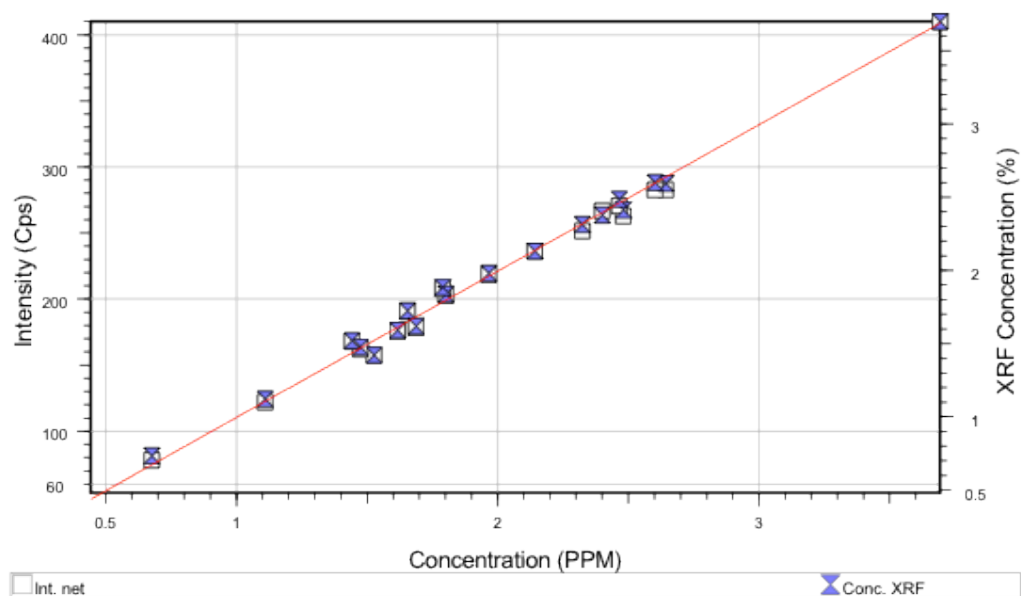
Intensity model: net intensity

Minimization target: absolute error, 19 standards from 0.67 % to 3.69 %

Standard deviation: 0.053 %

Squared correlation coefficient: 0.994040

Slope: 0.011154 %/Cps / Sensitivity: 86.69 Cps/% (Adjustable by regression)



V KA1/OSU BASALT 45

OSU BASALT 45

Abridged calibration data for line V KA1/OSU BASALT 45

S/N 1593, Mask: 30 mm, Mode: Air, 45 kV, 0.025 mA, Filter: None

Detector parameter 1: 600 parameter 2: 400

Peak Channels[trapeze]: 4.847 - 5.057 keV

Calibration data for compound V in original sample

Absorption correction: Variable alphas

Intensity model: net intensity

Minimization target: absolute error, 18 standards from 194 PPM to 330 PPM

Standard deviation: 17 PPM

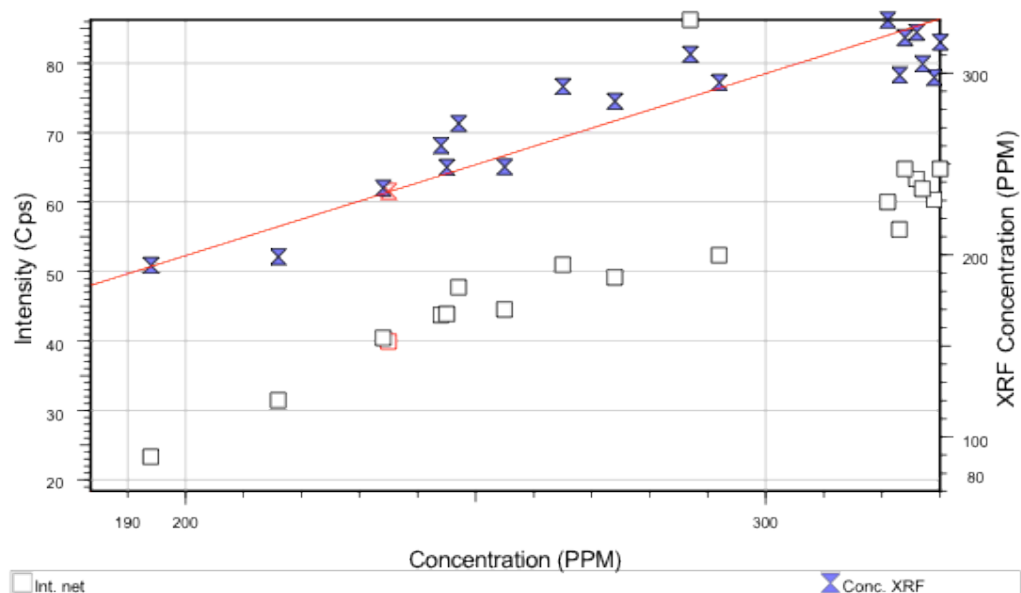
Squared correlation coefficient: 0.848751

Slope: 0.002595 %/Cps / Sensitivity: 385.3 Cps/% (Adjustable by regression)

Corrected intensity offset: +0.2347 Cps (Adjustable by regression) or -6.1 PPM

Line overlap correction by Intensity (Ti KA1/OSU BASALT 45) * (-0.1639) (Adjustable by regression)

Line overlap correction by Intensity (K KA1/OSU BASALT 45) * (-0.03177) (Adjustable by regression)



Y KA1/OSU BASALT 45

OSU BASALT 45

Abridged calibration data for line Y KA1/OSU BASALT 45

S/N 1593, Mask: 30 mm, Mode: Air, 45 kV, 0.025 mA, Filter: None

Detector parameter 1: 600 parameter 2: 400

Peak Channels[trapeze]: 14.82 - 15.07 keV

Calibration data for compound Y in original sample

Absorption correction: Variable alphas

Intensity model: net intensity

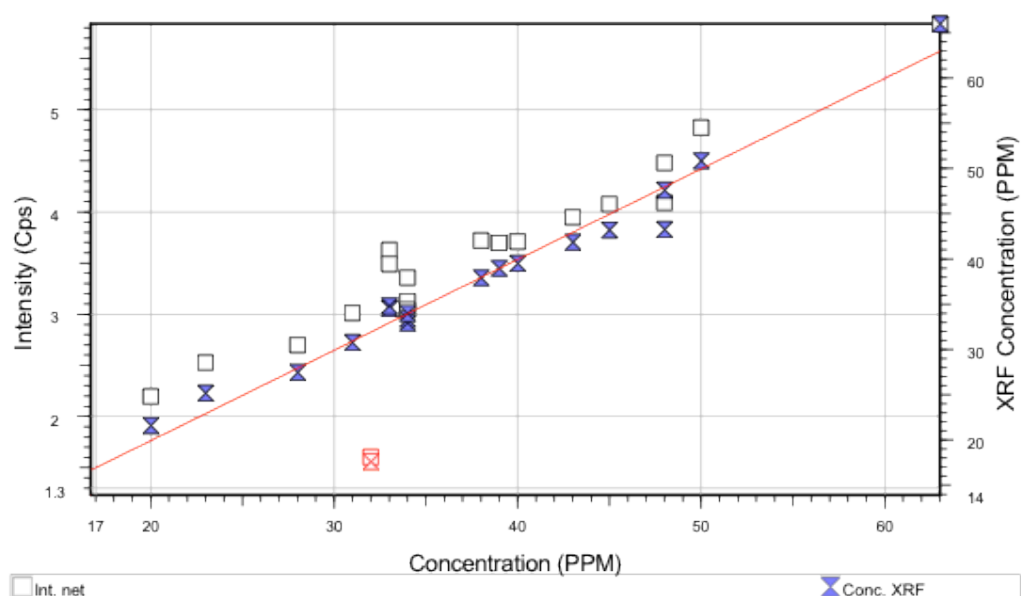
Minimization target: absolute error, 18 standards from 20 PPM to 63 PPM

Standard deviation: 2 PPM

Squared correlation coefficient: 0.971897

Slope: 0.004696 %/Cps / Sensitivity: 213 Cps/% (Adjustable by regression)

Corrected intensity offset: +0.06897 Cps (Adjustable by regression) or -3.2 PPM



Zn KA1/OSU BASALT 45

OSU BASALT 45

Abridged calibration data for line Zn KA1/OSU BASALT 45

S/N 1593, Mask: 30 mm, Mode: Air, 45 kV, 0.025 mA, Filter: None

Detector parameter 1: 600 parameter 2: 400

Peak Channels[trapeze]: 8.51 - 8.75 keV

Calibration data for compound Zn in original sample

Absorption correction: Variable alphas

Intensity model: net intensity

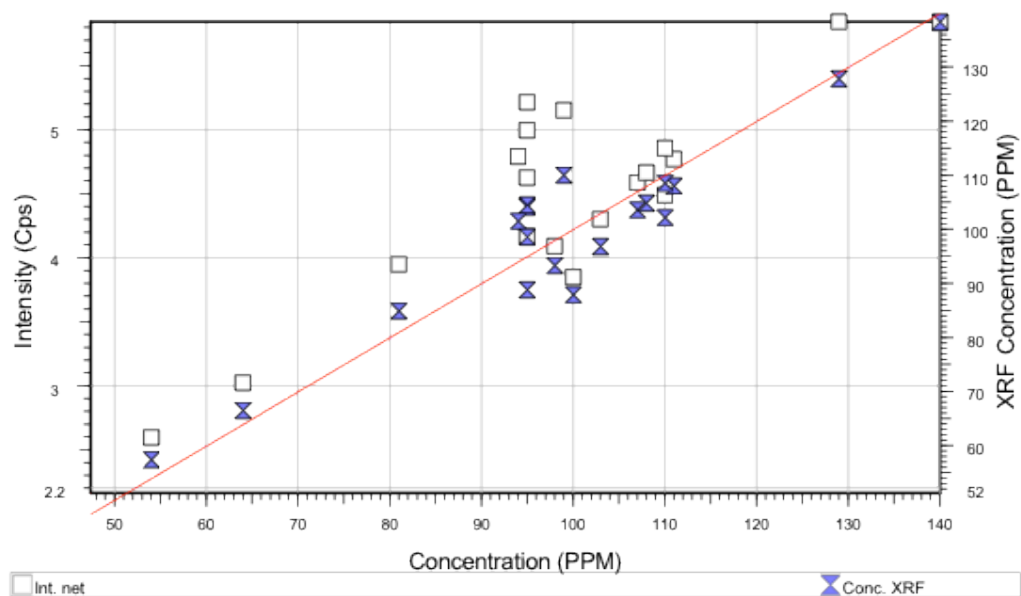
Minimization target: absolute error, 19 standards from 54 PPM to 140 PPM

Standard deviation: 6 PPM

Squared correlation coefficient: 0.890772

Slope: 0.003609 %/Cps / Sensitivity: 277.1 Cps/% (Adjustable by regression)

Corrected intensity offset: +0.3677 Cps (Adjustable by regression) or -13.3 PPM



Zr KA1/OSU BASALT 45

OSU BASALT 45

Abridged calibration data for line Zr KA1/OSU BASALT 45

S/N 1593, Mask: 30 mm, Mode: Air, 45 kV, 0.025 mA, Filter: None

Detector parameter 1: 600 parameter 2: 400

Peak Channels[trapeze]: 15.63 - 15.92 keV

Calibration data for compound Zr in original sample

Absorption correction: Variable alphas

Intensity model: net intensity

Minimization target: absolute error, 18 standards from 44 PPM to 296 PPM

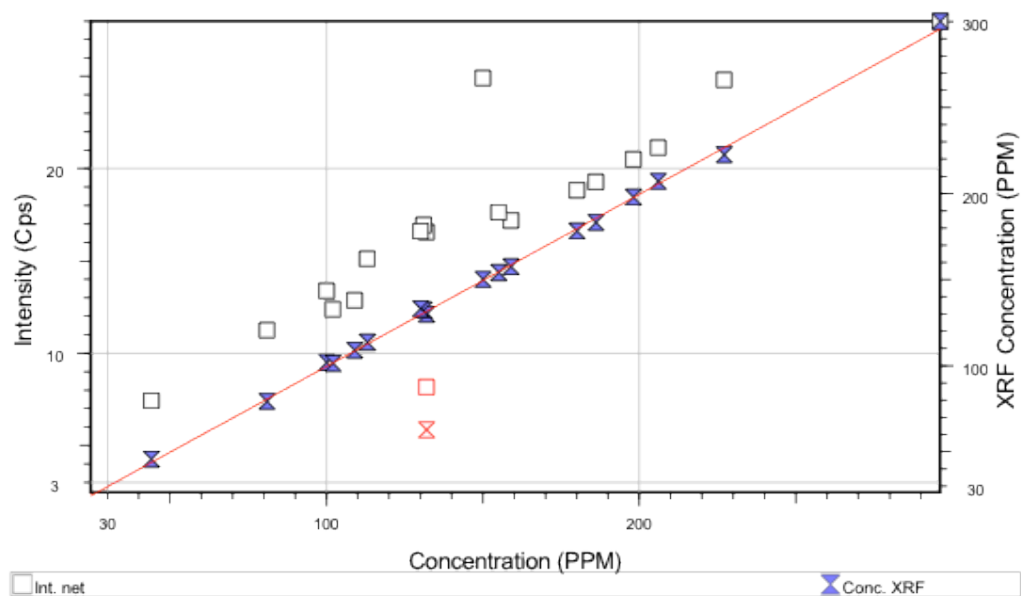
Standard deviation: 2 PPM

Squared correlation coefficient: 0.998763

Slope: 0.005894 %/Cps / Sensitivity: 169.7 Cps/% (Adjustable by regression)

Corrected intensity offset: +0.08942 Cps (Adjustable by regression) or -5.3 PPM

Line overlap correction by Intensity (Sr KA1/OSU BASALT 45) * (-0.1576) (Adjustable by regression)



APPENDIX D

Detailed Lithologic Descriptions

Late Miocene dacite to rhyolite lava flow and dome facies

Felsite (Tr1f)

The felsite facies is composed of lava flows and domes of devitrified gray glass with weak to moderate vesiculation aligned parallel to moderately-strongly developed, often highly contorted flow banding. Lithophysae, spherulitic zones, and perlitic fracturing occur locally.

Obsidian (Tr1o)

The obsidian facies is composed of black, red, brown, mahogany, and colorless obsidian flows. Textures are nonvesicular, ranging from massive uniform to strongly flow banded. Obsidian breccia clasts in an obsidian matrix occur locally.

Pumice (Tr1p)

The pumice facies occurs as coarsely vesicular pumice, commonly perlitically fractured that occurs stratigraphically above the obsidian zone. Weathered surfaces are tan and fresh surfaces are light to dark gray. Vesicles, which generally compose more than 50% of the volume, are ovoid to highly elongate, ranging from <1mm to a few cm in diameter.

Carapace Breccia (Trbx)

Brecciated pumice zones are found associated with flows and domes and occur as poorly sorted, black, gray & brown pumice clasts within an unaltered gray-brown pumice matrix. Clasts are angular, ranging from pebble to boulder size.

Biotite-phyric lava flows & domes (Tr₂)

Biotite-phyric lava flows contain 1-2% biotite, \pm quartz, \pm plagioclase, \pm sanidine phenocrysts in pumiceous, gray to brown, locally perlitically fractured groundmass. Elongate vesicles comprise 25-40% of the volume. Biotite phenocrysts are $<2\text{mm}$ and aligned parallel to flow banding.

Pyroclastic rhyolite (Tr_3)

The pyroclastic unit occurs as well indurated ash-flow tuff with clasts of obsidian, pumice, and felsite in a white- to pink-colored rhyolite ash matrix. Broad cross-bedding of cobble-size clasts occurs locally.

Rhyolite lavas (Tr_4)

Rhyolite lavas occur as black to gray; pink, often oxidized red rhyolite lava flows with common contorted flowbanding, typically with $<10\%$ plagioclase phenocrysts.

Rhyodacite lavas (Tr_5)

Black to gray; pink, often oxidized red rhyodacite lava flows are localized in the western end of the silicic complex and typically have $>10\%$ plagioclase and 2-6% hornblende phenocrysts.

Dacite lavas (Td)

Dacite lava flows that erupted from the west flank of Glass Butte are medium to dark gray with $\sim 5\%$ plagioclase phenocrysts and 5-10% elongate vesicles.

Pliocene to Pleistocene basalt to basaltic andesite lava flows and tuffs

Diktytaxitic olivine basalt (Tdb_1)

Pliocene age basalt lava flows are geochemically characterized by 0.2-0.4 wt.% K_2O , and 1.7-2.0 wt.% TiO_2 . Unit Tdb_1 directly overlies silicic rocks of the Glass Buttes complex in 3-8 meter thick faulted exposures directly east of Antelope Ridge and west of Round

Top Butte. To the north, a ~30 meter thick exposure lies at the base of the section east of Grassy Butte. No source vent has been identified for lava flows of unit Tdb₁. On the basis of available ages, Tdb₁ has a bracketed age between 6.49±0.03 and 4.18±0.07 Ma.

Basaltic andesite (Tba)

Pliocene basaltic andesite lava flows are geochemically characterized by 634-666 ppm Sr. A ~20m thick section exposed at the NW end of Parmele ridge is light to medium gray, aphyric, and has rare 1-5 cm rhyolite inclusions. Ten km away to the SE, an exposure along a fault scarp is dark gray, and has 20-30% 1-2mm elongate vesicles.

Basalt of Parmele Ridge (Tbpr)

Pliocene basalt unit Tpbr is geochemically characterized by 437-482 ppm Sr. This aphyric, light to medium gray basalt caps the west rim of Parmele ridge and is exposed in faulted outcrops south of Glass Butte. An ⁴⁰Ar/³⁹Ar age of 4.51±0.17 is reported for Tbpr (Fig. 5).

Diktytaxitic olivine basalt (Tdb₂)

The Pliocene age basalt unit Tdb₂ is geochemically characterized by 0.4-0.7 wt.% K₂O, and 1.5-1.8 wt.% TiO₂. Lava flows of unit Tdb₂ were erupted from at least two small, structurally aligned vents located ~3 kilometers northeast of Antelope Ridge and were channeled northwest along preexisting fault-controlled drainages in the silicic rocks of the Glass Buttes complex. ⁴⁰Ar/³⁹Ar ages of 4.70±0.27 and 4.31±0.29 Ma were determined for samples at two Tdb₂ vents (Fig. 5).

Basaltic-andesite of Grassy Butte (Tbgb)

The Pliocene age basaltic-andeiste of Grassy Butte is geochemically characterized by 1.1-1.3 wt% K₂O, and 2.3-2.7 wt.% TiO₂. Grassy Butte is a low, broad basaltic andesite

scoria cone and associated lava flows located 10 kilometers north of Little Glass Butte.

On the east side of the cone, deposits exposed in several cinder pits consist of mostly unconsolidated, oxidized, fine to coarse, scoriaceous cinders, bombs and agglutinate.

Lavas emanating from Grassy Butte consist of very dark gray to black, fine-grained basaltic-andesite with ~2% plagioclase phenocrysts generally <1 mm. An $^{40}\text{Ar}/^{39}\text{Ar}$ age of 4.18 ± 0.07 Ma was reported by Iademarco (2009).

Basalt of Hat Butte (Tbhb)

The Pliocene age basalt of Hatt Butte is geochemically characterized by 0.8-0.9 wt.% K_2O , and 2.6-2.7 wt.% TiO_2 . Hat Butte is a prominent mafic vent and related lava flows located 8 kilometers southeast of Grassy Butte. Lava flows from Hat Butte are medium to dark gray, with 5% plagioclase (1-3 mm) and rare olivine phenocrysts in a fine-grained groundmass.

Pyroxene Basalt (Tpb)

The Pliocene age basalt unit Tpb is geochemically characterized by 290-298 ppm Sr, and 3.2-3.5 Ni/Zr with a phenocrysts assemblage of ~20% pyroxene up to 1mm long, and 20% plagioclase 1-3mm long, and rare <1mm size olivine phenocrysts with abundant plagioclase microlites in the groundmass. Exposed in an isolated faulted outcrop just south of Glass Butte and capping a prominent fault scarp southeast of Round Top Butte.

Diktytaxitic olivine basalt (Tdb₃)

The Pliocene age basalt unit Tdb₃ is geochemically characterized by 0.1-0.2 wt.% K_2O , and 0.6-1.0 wt.% TiO_2 . Lava flows of unit Tdb₃ form much of the plateau north of Glass Butte and are well exposed in the prominent fault scarp forming Rattlesnake Ridge. To the south, flows of unit Tdb₃ also form the eastern rim of Parmele Ridge. No source vent

has been identified for flows of unit Tdb₃. An $^{40}\text{Ar}/^{39}\text{Ar}$ age of 2.81 ± 0.05 Ma was determined from a sample located at a Qpmb vent (Fig. 5).

Plagioclase trachytic basalt (Ttb)

The Pliocene-Pleistocene age basalt unit Ttb is a dark gray to black, fine-grained basalt with abundant flow aligned plagioclase laths and well-defined platy jointing exposed only along a ~30m high fault scarp east of Rattlesnake Ridge.

Diktytaxitic olivine basalt (Tdb₄)

The Pliocene-Pleistocene age basalt unit Tdb₄ is geochemically characterized by 74-119 ppm Zr, and 0.17-0.19 wt.% MnO. Lava flows of Tdb₄ form much of the low-lying topography west of Parmele Ridge. At Parmele Ridge, Tdb₄ is banked against and partially buries the uplifted Tba and Tbpr fault scarp. It is similarly lapped onto the prominent Ttb scarp to the north.

Mafic lapilli tuff (Tlt)

Unit Tlt is a Pliocene-Pleistocene age, 3-5 meter thick unwelded lapilli tuff composed of tan and brown pumice and lithics in a dark gray ashy matrix. Highly eroded, unit Tlt is typically only preserved where underlying a cap rock of younger basalt.

Plagioclase intergranular basalt (Tpib)

The Pliocene-Pleistocene age unit Tpib is a plagioclase-rich (~30%) basalt with intergranular olivine and a fine-grained groundmass. Lava flows of Tpib are found banking against the south side of the Parmele Ridge fault scarp and in an uplifted horst block to the south. No source vent is identified for Tpib.

Plagioclase-Olivine glomerophyric basalt (Tgb)

Pliocene-Pleistocene lava flows of basalt unit Tgb are found in the eastern map area, where flows erupted from several small vents between Round Top Butte and Cascade Ridge. To the west, 10-12 meter thick Tgb lava flows erupted from a nearby vent make up the up-thrown rim rock of Stauffer Rim. This medium to dark gray basalt is characterized by round clusters of olivine and plagioclase up to 1 cm in diameter in a fine-grained groundmass.

Plagioclase megaphyric basalt (Qpmb)

Low volume Pleistocene age lava flows of Qpmb erupted from two vents on the south and southeast flanks of Glass Butte. Individual lava flows are 5-10 meters thick and are characterized by 1-3 cm long plagioclase phenocrysts in a fine-grained groundmass with abundant plagioclase microlites. An $^{40}\text{Ar}/^{39}\text{Ar}$ age of 2.04 ± 0.38 Ma was determined from a sample located at a Qpmb vent (Fig. 5).

Diktytaxitic olivine basalt (Qdb)

Pleistocene age basalt lava flows of unit Qdb are geochemically characterized by 0.4-0.5 wt.% K_2O , and 2.3-2.7 wt.% TiO_2 . Lava flows of unit Qdb were erupted from fault-aligned vents both within and on the flanks of the main Glass Buttes silicic complex, and were channeled to the northwest along a preexisting fault-controlled structural fabric. A small kipuka of Glass Buttes silicic rocks projects through flows of unit Qdb erupted from a small vent located between Cascade Ridge and Antelope Ridge. An $^{40}\text{Ar}/^{39}\text{Ar}$ age of 1.39 ± 0.18 is reported for Qdb (Fig. 5).

APPENDIX E

Summary of $^{40}\text{Ar}/^{39}\text{Ar}$ incremental heating (this study)

Incremental Heating		36Ar(a)	37Ar(ca)	38Ar(cl)	39Ar(k)	40Ar(r)	Age $\pm 2\sigma$ (Ma)	40Ar(r) (%)	39Ar(k) (%)	K/Ca	$\pm 2\sigma$
12C1685	400 °C	0.000665	0.006752	0.000089	0.002923	0.008199	7.96 ± 5.65	4.01	4.38	0.186	± 0.007
12C1686	500 °C ✓	0.000435	0.027662	0.000159	0.007355	0.006766	2.61 ± 2.15	5.00	11.01	0.114	± 0.004
12C1687	600 °C ✓	0.000641	0.172892	0.000375	0.017293	0.017922	2.95 ± 0.80	8.65	25.89	0.043	± 0.001
12C1689	700 °C ✓	0.000323	0.198755	0.000232	0.012725	0.012344	2.76 ± 1.23	11.45	19.05	0.028	± 0.001
12C1690	800 °C ✓	0.000208	0.205126	0.000147	0.010654	0.010231	2.73 ± 1.17	14.25	15.95	0.022	± 0.001
12C1691	950 °C ✓	0.000193	0.159100	0.000157	0.008090	0.007975	2.80 ± 1.20	12.25	12.11	0.022	± 0.001
12C1693	1100 °C ✓	0.000232	0.101649	0.000135	0.004244	0.003585	2.40 ± 3.92	4.97	6.35	0.018	± 0.001
12C1694	1250 °C ✓	0.000340	0.119643	0.000103	0.002388	0.002050	2.44 ± 2.63	2.00	3.58	0.009	± 0.000
12C1695	1400 °C ✓	0.000328	0.068795	0.000027	0.001118	0.000933	2.37 ± 16.32	0.95	1.67	0.007	± 0.000

Information on Analysis		Results	40(r)/39(k) $\pm 2\sigma$	Age $\pm 2\sigma$ (Ma)	MSWD	39Ar(k) (% _n)	K/Ca	$\pm 2\sigma$
GB012		Weighted Plateau	0.9877 ± 0.1745 $\pm 17.67\%$	2.81 ± 0.50 $\pm 17.67\%$	0.04	95.62 8	0.013	± 0.007
groundmass								
HLP				External Error	2.36	Statistical T Ratio Error Magnification		
jh				Analytical Error	1.0000			
Project = HLP		Total Fusion Age	1.0481 ± 0.2274 $\pm 21.69\%$	2.98 ± 0.65 $\pm 21.69\%$		9	0.027	± 0.000
Irradiation = OSU1B12								
J = 0.0015765 \pm 0.0000060								
FCT-3 = 28.030 \pm 0.003 Ma								
				External Error				
				Analytical Error				

Incremental Heating		36Ar(a)	37Ar(ca)	38Ar(cl)	39Ar(k)	40Ar(r)	Age $\pm 2\sigma$ (Ma)	40Ar(r) (%)	39Ar(k) (%)	K/Ca	$\pm 2\sigma$
12C1586	400 °C	0.001857	0.003922	0.000075	0.003275	0.012947	11.33 ± 6.57	2.31	2.29	0.359	± 0.017
12C1587	500 °C ✓	0.002891	0.007899	0.000148	0.008779	0.005353	1.75 ± 3.17	0.62	6.15	0.478	± 0.015
12C1588	600 °C ✓	0.003408	0.025111	0.000211	0.017832	0.012022	1.94 ± 1.86	1.18	12.49	0.305	± 0.009
12C1590	700 °C ✓	0.002131	0.041679	0.000124	0.018125	0.014209	2.25 ± 1.00	2.21	12.70	0.187	± 0.005
12C1591	800 °C ✓	0.001550	0.072085	0.000117	0.020387	0.014405	2.03 ± 0.74	3.05	14.28	0.122	± 0.003
12C1592	900 °C ✓	0.001170	0.082056	0.000117	0.017889	0.012428	2.00 ± 0.58	3.47	12.53	0.094	± 0.003
12C1594	1000 °C ✓	0.001084	0.091917	0.000194	0.016784	0.011684	2.00 ± 1.30	3.52	11.76	0.079	± 0.002
12C1595	1100 °C	0.001003	0.089364	0.000207	0.013047	0.019612	4.32 ± 1.17	6.21	9.14	0.063	± 0.002
12C1596	1250 °C	0.002135	0.223552	0.000513	0.018187	0.032686	5.16 ± 1.22	4.93	12.74	0.035	± 0.001
12C1598	1400 °C	0.001036	0.114770	0.000255	0.008432	0.011472	3.91 ± 2.07	3.61	5.91	0.032	± 0.001

Information on Analysis		Results	40(r)/39(k) $\pm 2\sigma$	Age $\pm 2\sigma$ (Ma)	MSWD	39Ar(k) (% ,n)	K/Ca	$\pm 2\sigma$
GB026-10		Weighted Plateau	0.7091 ± 0.1337 $\pm 18.86\%$	2.04 ± 0.38 $\pm 18.86\%$	0.05	69.92 6	0.108	± 0.051
groundmass								
HLP								
jh								
Project = HLP		Total Fusion Age	1.0286 ± 0.1640 $\pm 15.94\%$	2.96 ± 0.47 $\pm 15.95\%$	1.0000	10	0.082	± 0.001
Irradiation = OSU1B12								
J = 0.0015939 \pm 0.0000057								
FCT-3 = 28.030 \pm 0.003 Ma								

Statistical T
Ratio
Error
Magnification

Incremental Heating		36Ar(a)	37Ar(ca)	38Ar(cl)	39Ar(k)	40Ar(r)	Age $\pm 2\sigma$ (Ma)	40Ar(r) (%)	39Ar(k) (%)	K/Ca $\pm 2\sigma$
12C1544	400 °C	0.000240	0.002267	0.000090	0.003975	0.001120	0.83 ± 3.28	1.56	2.06	0.754 ± 0.026
12C1545	500 °C ✓	0.000350	0.010055	0.000262	0.012415	0.018895	4.46 ± 1.06	15.44	6.44	0.531 ± 0.015
12C1547	600 °C ✓	0.000564	0.070100	0.000567	0.035283	0.054637	4.54 ± 0.27	24.68	18.30	0.216 ± 0.006
12C1548	675 °C ✓	0.000327	0.082532	0.000364	0.029320	0.044591	4.46 ± 0.38	31.57	15.21	0.153 ± 0.004
12C1549	750 °C ✓	0.000238	0.107830	0.000243	0.032588	0.049653	4.47 ± 0.39	41.36	16.90	0.130 ± 0.003
12C1551	800 °C ✓	0.000137	0.076794	0.000128	0.022688	0.034850	4.50 ± 0.54	46.16	11.77	0.127 ± 0.003
12C1552	850 °C ✓	0.000094	0.063089	0.000082	0.017404	0.027399	4.62 ± 1.00	49.62	9.03	0.119 ± 0.003
12C1553	925 °C ✓	0.000101	0.071066	0.000063	0.016846	0.026220	4.56 ± 1.11	46.87	8.74	0.102 ± 0.003
12C1555	1025 °C ✓	0.000099	0.066155	0.000070	0.011993	0.018036	4.41 ± 1.35	38.19	6.22	0.078 ± 0.002
12C1556	1150 °C	0.000119	0.073536	0.000079	0.006558	0.005895	2.64 ± 2.06	14.39	3.40	0.038 ± 0.001
12C1557	1300 °C	0.000043	0.051903	0.000041	0.002607	0.011997	13.46 ± 5.99	48.42	1.35	0.022 ± 0.001
12C1559	1400 °C	0.000045	0.023061	0.000006	0.001104	0.000016	0.04 ± 8.94	0.12	0.57	0.021 ± 0.001

Information on Analysis	Results	40(r)/39(k) $\pm 2\sigma$	Age $\pm 2\sigma$ (Ma)	MSWD	39Ar(k) (% ,n)	K/Ca $\pm 2\sigma$
GBP7-11 groundmass	Weighted Plateau	1.5365 ± 0.0584 $\pm 3.80\%$	4.51 ± 0.17 $\pm 3.85\%$	0.04	92.61 8	0.115 ± 0.036
HLP			External Error ± 0.19	2.36	Statistical T Ratio Error Magnification	
jh			Analytical Error ± 0.17	1.0000		
Project = HLP	Total Fusion Age	1.5215 ± 0.0850 $\pm 5.59\%$	4.46 ± 0.25 $\pm 5.62\%$			12
Irradiation = OSU1B12			External Error ± 0.26			0.119 ± 0.001
J = 0.0016276 \pm 0.0000055			Analytical Error ± 0.25			
FCT-3 = 28.030 \pm 0.003 Ma						

Incremental Heating		36Ar(a)	37Ar(ca)	38Ar(cl)	39Ar(k)	40Ar(r)	Age $\pm 2\sigma$ (Ma)	40Ar(r) (%)	39Ar(k) (%)	K/Ca	$\pm 2\sigma$
12C347	400 °C	0.045042	0.023805	0.000157	0.003329	0.085129	68.36 ± 45.29	0.64	3.06	0.060	± 0.009
12C348	500 °C	0.025485	0.026456	0.000093	0.004640	0.014264	8.36 ± 19.66	0.19	4.27	0.075	± 0.008
12C349	600 °C ✓	0.009492	0.093756	0.000080	0.009543	0.014739	4.20 ± 4.29	0.52	8.78	0.044	± 0.005
12C351	700 °C ✓	0.004142	0.182960	0.000071	0.018524	0.029353	4.31 ± 1.06	2.34	17.04	0.044	± 0.004
12C352	800 °C ✓	0.002334	0.255877	0.000084	0.027003	0.042834	4.32 ± 0.44	5.85	24.84	0.045	± 0.004
12C353	900 °C ✓	0.000912	0.187274	0.000101	0.019574	0.030629	4.26 ± 0.49	10.20	18.01	0.045	± 0.004
12C355	1025 °C ✓	0.000774	0.155136	0.000086	0.013928	0.022479	4.39 ± 0.79	8.94	12.81	0.039	± 0.004
12C356	1150 °C ✓	0.000533	0.099966	0.000060	0.006601	0.010382	4.28 ± 1.51	6.19	6.07	0.028	± 0.003
12C357	1275 °C ✓	0.000395	0.069584	0.000059	0.003495	0.006086	4.74 ± 4.69	4.96	3.22	0.022	± 0.002
12C359	1400 °C	0.000262	0.041623	0.000032	0.002051	0.011100	14.69 ± 6.41	12.55	1.89	0.021	± 0.003

Information on Analysis	Results	40(r)/39(k)	$\pm 2\sigma$	Age	$\pm 2\sigma$ (Ma)	MSWD	39Ar(k) (%,n)	K/Ca	$\pm 2\sigma$
GB10B037 HLP 2A24-11 gm HLP db Project = HLP Irradiation = OSU2A11 J = 0.0015103 ± 0.0000089 FCT-3 = 28.030 ± 0.003 Ma	Weighted Plateau	1.5824	± 0.1047 ± 6.62%	4.31	± 0.29 ± 6.71%	0.02	90.78 7	0.033	± 0.008
			External Error		± 0.30	2.45	Statistical T Ratio Error Magnification		
			Analytical Error		± 0.28	1.0000			
	Total Fusion Age	2.4565	± 0.6393 ± 26.03%	6.68	± 1.74 ± 26.00%			10	0.041
			External Error		± 1.74				
			Analytical Error		± 1.74				

Statistical T
Ratio
Error
Magnification

Appendix F: Sample Location Map Keyed to Geochemical Groups

